Modelling of bushes and hydro mounts in vehicles using a multi body simulation environment

Scheiblegger, Christian

Award date:
2019

Modelling of bushes and hydro mounts in vehicles using a multi body simulation environment

Scheiblegger, Christian

Award date:
2019

MODELLING OF BUSHES AND HYDRO MOUNTS IN VEHICLES USING A MULTI BODY SIMULATION ENVIRONMENT

Christian Scheiblegger

A thesis submitted for the degree of Doctor of Philosophy

University of Bath
Department of Mechanical Engineering

2018

ABSTRACT

Engine mounts and suspension bushes are crucial for ride comfort and handling, durability loads and vehicle dynamics. To ensure good ride comfort and vehicle handling the various mounts must be tuned carefully for an optimal setup. This tuning work is very time consuming and expensive because prototypes and expert test drivers are needed. Computer based tuning is very beneficial for manufacturers but there is a need for improved elastomer and hydro mount numerical models.

In the established development process, multi body simulations (MBS) based on rigid bodies are used in combination with simple spring-damper models for the rubber mounts. Such linear models enable good forecasts in the time domain within a limited frequency and displacement range, only.

To improve the accuracy of full-vehicle simulations, a practical non-linear model for mounts and bushes has been identified, that takes into account the amplitude dependent behaviour of elastomers. The model has been improved and implemented into a full vehicle simulation environment and numerical issues and principal drawbacks have been solved.

In the past a number of model concepts have been suggested for hydraulically damped mounts, but most of them neglect the amplitude dependence of the underlying rubber parts. This simplification leads to less accuracy. Some hydro mount models need experimental data for parameterization that is not available. Other models are rough estimations for certain types of hydro mounts or they lack a stable and easy-to use parameter identification process. The newly developed elastomer model has therefore been incorporated in a numerical model for hydro mounts, leading to higher accuracy and flexibility for different sorts of hydro mounts and bushes. The suggested model uses physically based model parameters that allow a detailed study of underlying hydro mount phenomena.

Beside the main models, a user-friendly, fast and stable process for parameter identification is needed. Programs for a virtual mount test rig, the import and further processing of measurement data, parameter identification and export of model parameter files for an MBS environment within a graphical user interface (GUI) have been developed to ensure usability and practicality for different areas of use.

The presented models and methods are designed for use in an early phase of development to predict the overall behaviour of vehicles. The mount’s behaviour is simulated within an MBS environment based on parametric data from a few standard experiments. The focus is to predict the transient behaviour based on simple tests from data obtained during sinusoidal excitation.

The models have been implemented into a commonly used MBS environment and validated within full-vehicle models for ride comfort analyses and durability load calculation. For model evaluation, frequencies up to 50 Hz with excitation amplitudes up to +/- 3 mm were of main interest. The accuracy of full-vehicle simulations can be significantly improved, using the new models for all bushes and hydro mounts.

This thesis outlines existing literature relating to the modelling of elastomeric mounts, the model develop process and validation. This is supported by a number of journal publications written by the author that provide additional data and discussion.

ACKNOWLEDGEMENTS

Heartfelt thanks to my family and Anita Galic, who have supported me in every possible way throughout my entire academic education.

Many thanks for their excellent supervision to Dr Andrew Hillis and Dr Jos Darling. Excellence meaning a commitment to completion, thank you for the guidance and motivation through all the challenging phases. Thanks also to Dr Roger Ngwompo and Prof Dr Necip Sahinkaya for their valuable feedback and suggestions on intermediate reports. Sincere thanks to Prof Dr Andrew Plummer and Prof Dr Kambiz Ebrahimi as internal and external examinaers for their very valuable feedback. I've enjoyed outstanding support and collegiality at the University of Bath; my thank goes to all post-graduates, lecturers and staff I know.

The presented research was mainly carried out at Munich University of Applied Sciences, as part of a research collaboration with Audi, Magna Steyr Fahrzeugtechnik (MSF), the Virtual Vehicle Compentence Center (ViF) and Helmut Schmidt University. Projects with Porsche, MSF, Fiat-Chrysler Automobiles (FCA), IPG Automotive, MdynamiX AG and VI-grade followed. I would like to thank Hannes Karrer for suggesting the idea and establishing the project at Audi and his great contributions through inspirational and motivating discussions. Further thanks go to Harald Jendryka, Jan Straßburg and Sebastian Krebs at Audi and Werner Reinalter at MSF. Thanks to Hans-Jürgen Büchler for discussions about model implementation at Porsche.

Most of the experiments shown herein were carried out at Conti Tech Vibration Control; many thanks to Michael Binar for advice on the nature of rubber and test rigs. Many thanks for the rewarding discussions and professional software development to Christoph Ortmann and Renzo Scaletta from VI-grade. I also want to thank Dr Martin Rosenberger, Peter Wimmer and Nicolas Geiger from ViF for their support as experts for full-vehicle simulation.

Special thanks to Dr Nantu Roy for his many positive contributions and to Dr Fabian Hausberg.

Many thanks for rewarding discussions, great collegiality and personal advice to my former colleagues at Munich University of Applied Sciences: Dr Jinhuai Lin, Dr Rico Schimpf, Jan Hlawatschek, Alessandro Contini, David Burmann and Mike Kunz. I would also like to thank the many other partners and students who have been involved.

My sincere thank to Prof Dr Peter Pfeffer for his trust and the support as external supervisor. You have taught me many things in life, besides research.

Last but not least, many thanks to you, the interested reader.

TABLE OF CONTENTS

PUBLICATIONS

The work conducted for this thesis has led to the following journal and conference articles, which are presented as stand-alone chapters within this thesis:

Paper A Scheiblegger, C., Roy, N., Silva Parez, O., Hillis, A. et al., "***Non-Linear Modeling of Bushings and Cab Mounts for Calculation of Durability Loads,***" SAE Technical Paper 2014-01-0880. 2014, doi: 10.4271/2014-01-0880.

- **Elastomer Mount Model**
- The author conducted most of the research independently. Design of experiments, data processing, model development, parameter identification and presentation of the results were his responsibility. (He generated approximately 80% of the content).

Paper B1 Scheiblegger, C., Roy, N., Hillis, A. J., and Pfeffer, P., "***Modeling Hydro Mounts in Vehicles for Durability Load Analyses, Ride Comfort and Vehicle Dynamics Simulation,***" AVEC 2016, Munich.

- **Hydro Mount Model**
- The author conducted most of the research independently. Model development and description, parameter identification and presentation of the results were his responsibility. His contribution for this publication is approximately 90%.

Paper B2 Scheiblegger, C., Roy, N., Hillis, A. J., and Pfeffer, P., "**Hydro mounts: An in-depth look at modeling hydro mounts in vehicles for durability load analyses, ride comfort and vehicle dynamics simulation**," Vehicle Dynamics International, Annual Showcase 2017.

- **Hydro Mount Model**
- Due to a high level of interest in paper B1 following the conference presentation and its publication, the authors were invited to republish the content for a wider audience in a journal. 90% contribution of the lead author.

Paper C Hausberg, F., Scheiblegger, C., Pfeffer, P., Plöchl, M. et al., "**Experimental and analytical study of secondary path variations in active engine mounts**," Journal of Sound and Vibration. 2015, 340:22–38, doi: 10.1016/j.jsv.2014.11.024.

- **Model Linearization and Study on Active Hydro Mounts**

- As second author, he was responsible for model development and parameter identification for the rubber part and other components of the hydro mount. Contribution is approx. 30%.

Paper D Roy, N., Scheiblegger, C., Darling, J., and Pfeffer, P., "***Durability Loads Prediction of Body-on-Frame Vehicles using Full Vehicle Simulation,"*** Int. Journal of Passenger Car, SEA Technical Paper 2017-01-9675. RETRACTION

- **Full-vehicle study to validate the models in MBS environment**
- As second author, he was responsible for model development for bushing elements, support for parameter identification and presentation of the outcomes regarding the bushing elements. Contribution is approx. 50%. This peer-reviewed paper was published several months before it had to be withdrawn on behalf of Fiat-Chrysler Automobiles due to confidentiality/legal issues, after the leading author had left the company.

Besides these main articles, the conducted research has been published in other conference proceedings, which are not included in this thesis:

Scheiblegger, C., Pfeffer, P. E., Karrer, H., and Geiger, N., "***Modelling of Elastomer and Hydro Mounts for Ride Comfort and Handling Simulation***," In 13th International VDI Congress Tires-Chassis-Road, Hanover, Germany: VDI-Berichte 2137, 2011 (German)

- **Evaluation of early model version and full-vehicle simulation for ride comfort**

  (Contribution approx. 80%)

Scheiblegger, C., Lin, J., and Karrer, H., "***New nonlinear bushing model for ride comfort and handling simulation: Focussing on linearization and the implementation into MBS environment***." Paper read at FISITA 2012 World Automotive Congress, November 27-30 2012, at Beijing, China, 2012.

- **Elastomer Model and Linearization**

  (Contribution approx. 90%)

1 INTRODUCTION AND BACKGROUND

Simulation is needed to predict the behaviour of not-yet-existing vehicles, using dynamic simulation software tools, to obtain a good starting point for the fine-tuning of suspension components later in the development process. Variations of the vehicle, such as wheels, engines, drivetrain and comfort equipment create challenges for suspension tuning. Different driving and weather conditions as well as tolerance ranges for all components add complexity, so that the entire product range of vehicles cannot be tested and tuned with real parts on the road. Critical combinations of equipment, tolerances and temperatures have to be investigated with the help of multi-body simulation (MBS) in order to limit real on-road testing to a few variations.

Besides the wheels and tyres, suspension coil springs and shock absorbers, the many mounts and bushes used on the suspension sub-frame and powertrain highly affect ride comfort, vehicle handling and durability. There are many different types of mounts and bushes in the car, most of them are conventional rubber-metal bushes. The term *rubber* describes a natural-rubber (NR) based mixture of the material, whereas the term *elastomer* includes all sorts of synthetically based rubber-like materials. The *linear viscoelastic* behaviour of unfilled natural rubber leads to frequency dependence and can be modelled accurately with combinations of springs and dampers, but after vulcanisation other *non-linear effects* occur in varying importance. Besides elastomer mounts, hydraulically damped mounts are used to further improve vibration isolation and damping characteristics.

Figure 1-1 highlights some bushing elements in a MBS vehicle model and defines vehicle coordinates. Powertrain mounts and suspension bushes are indicated.

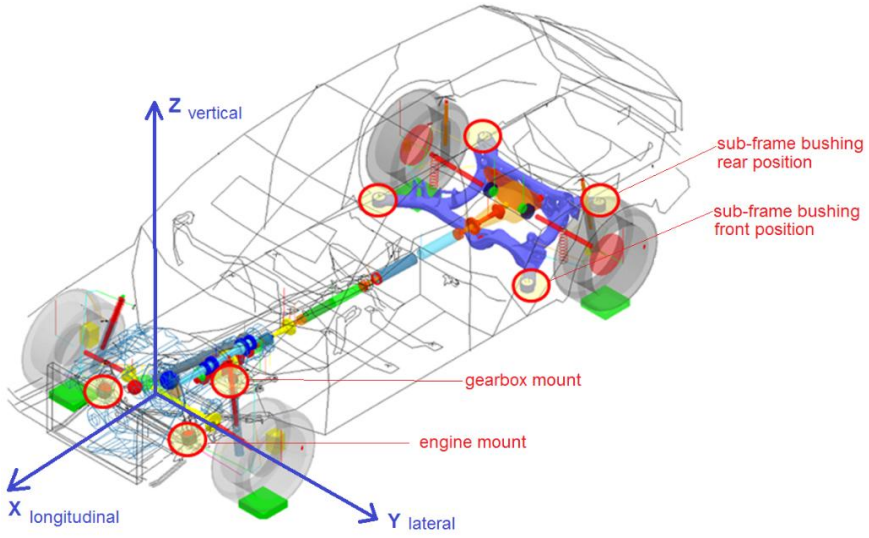

Figure 1-1: Passenger car in virtual MBS environment with several bushing elements and definitions for vehicle coordinate system (modified from Rigler (2009))

The powertrain rests on engine and gearbox mounts and suspension parts are connected to the car body by bushes. Bushing elements are traditionally represented as simple spring-damper systems within the MBS software environment. Figure 1-2 shows cross-sections of different types of mounts.

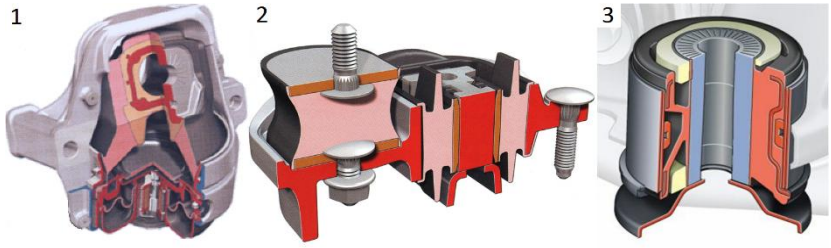

Figure 1-2: Types of mounts: passive hydraulic engine mount (HEM) with decoupling membrane (1), conventional rubber gearbox mount (2) hydro suspension bushing for rear sub-frame (3).

All mounts contain rubber or rubber-like elastomer and can be divided into conventional elastomer mounts and hydraulically damped mounts. Elastomer mounts are most commonly used and engine mounts are often hydraulically damped (1). The gearbox mount (2) is of modular structure, in which the vertical load is carried from a simple interchangeable rubber element, whereas separate rubber cushions are incorporated into the metal housing for longitudinal and transverse directions. In contrast, suspension bushes (3) usually have rotational symmetry, so that three-dimensional coupling effects might be relevant. Similar bushes are also used for rail vehicles and other applications.

In the simulation environment, such parts are referred to as *bushing elements*. Real bushes exhibit complex non-linear behaviour that depends on the mass on the mount, the excitation amplitude and frequency spectrum associated with the engine and road disturbances.

1.1 Standard Characterisation

Cardillo (1964) and the standards *DIN 53535* and *VDI 3880* discuss the measurement of rubber parts. To characterise mounts, the quasi-static stiffness curve is measured at very slow excitation velocities and the static stiffness k_{stat} is calculated around the main operating point with an appropriate design preload.

Generally, the stiffness characteristics of elastomer parts under quasi-static excitation are non-linear with a progressive curve. The exact characteristics depend on the part's geometry and its material composition. Figure 1-3 (left) shows a static characteristic stiffness curve at slow excitation (10 mm/min) for an elastomer mount over a wide displacement range (+/- 6mm). Around the operating point without preload (0N), stiffness remains constant but stiffness increases at higher deflections when the bush goes into 'progression'. Therefore, the behaviour depends on preloading conditions.

Following excitation, relaxation behaviour can be observed for elastomeric parts. The material's internal stress gradually decreases over time. Under periodic excitation this relaxation leads to hysteresis. A small hysteresis is already visible in the static stiffness curve.

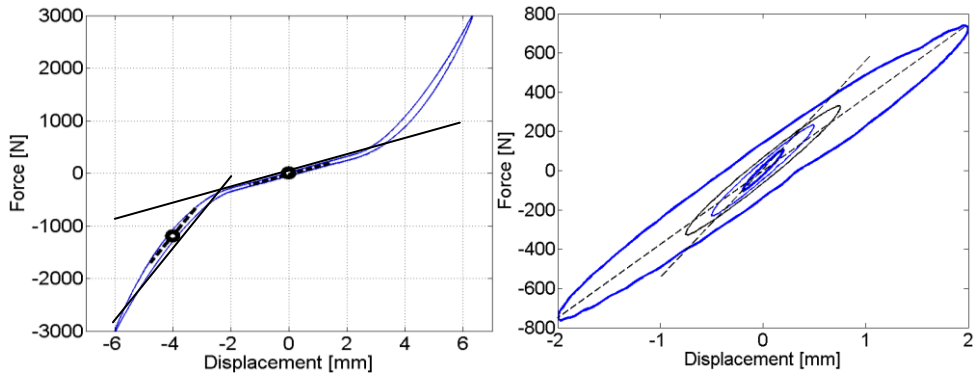

Figure 1-3: Measured non-linear static displacement-force characteristics at 10mm/min and calculation of average static stiffness k_{stat} at various operating points (left). Behaviour at dynamic sinusoidal excitation at 10Hz with amplitude dependent hysteresis characteristics (right): Note that the average stiffness at small excitation amplitudes is higher than at high amplitudes.

To characterize the mount's dynamic behaviour the force-displacement loops are measured at sinusoidal excitation with increasing frequency, for different amplitudes. The resulting average dynamic stiffness k_{dyn} at sinusoidal excitation is much higher than the static stiffness and depends on the frequency and amplitude.

Figure 1-3 (right) shows force-displacement loops at 10 Hz for various amplitudes around the operating point 0 N. The broken lines indicate a stiffness of 390 N/mm @ 2 mm but 580 N/mm at 0.1 mm. This behaviour is independent of the static stiffness, which shows almost constant stiffness around this operating point at 0 N.

The dynamic stiffness can be derived as an average from force-displacement loops. Alternatively, the dynamic stiffness can be represented as a complex vector as shown in Figure 1-4. The complex value of stiffness is described by K_d where the dynamic stiffness k_{dyn} is the absolute value of the complex stiffness K_d.

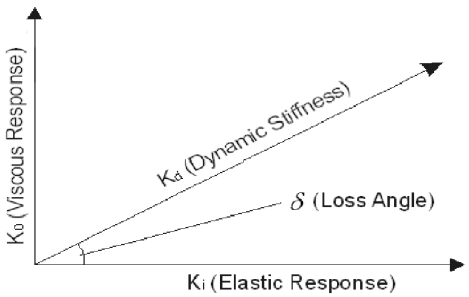

Figure 1-4: Complex representation of dynamic stiffness (Turner 2005)

$$k_{dyn} = |K_d| = \left|\frac{\hat{F}(\Omega)}{\hat{U}(\Omega)}\right| \qquad (1\text{-}1)$$

$$K_d = k_{dyn}\cos\delta + \left(k_{dyn}\sin\delta\right)\cdot i \tag{1-2}$$

The loss angle δ is widely used to characterise the damping behaviour of mounts and bushings. The loss angle δ is the complex argument (or phase) of the complex dynamic stiffness K_d. U is the displacement input and $\hat{U}$ and $\hat{F}$ represent the amplitude of the input displacement and output force for a defined frequency Ω, respectively.

$$\delta = \arg\left(\frac{\hat{F}(\Omega)}{\hat{U}(\Omega)}\right) \tag{1-3}$$

Both the dynamic stiffness and loss angle change with frequency and - more significantly - with the excitation amplitude: A typical measured dynamic stiffness and loss angle as a function of frequency for a rubber mount are presented in Figure 1-5. Dynamic stiffness and loss angle generally increase with increasing frequency. The dynamic stiffness is much higher than the static stiffness and decreases with amplitude. The loss angle typically increases with amplitude but reaches a maximum, depending on the tested amplitude range; in the example, 1 mm gives the maximum loss angle.

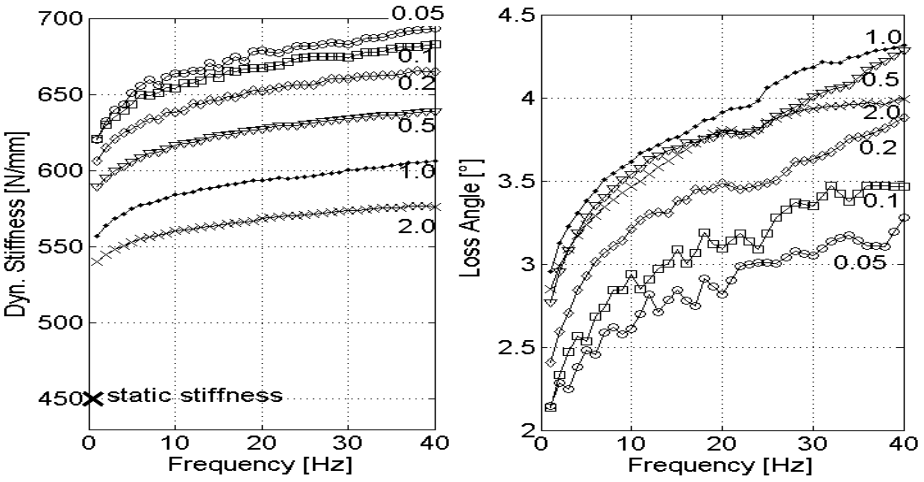

Figure 1-5: Typical dynamic characteristics of elastomer bush: measured dynamic stiffness (left) and loss angle (right) over frequency. Amplitude dependence behaviour

The static stiffness does not change around this amplitude range; so, the different stiffness and damping characteristics are only due to the Payne effect *(Payne 1964)* that is typical for elastomeric parts.

1.2 Standard Bushing Model in MBS

In multibody simulations (MBS) – or multibody dynamics (MBD) simulation most parts of the vehicle are regarded as rigid masses, few elements are modelled elastically. The bodies are connected by kinematic constraints (joints) that restrict their motion, or simple force elements for components like bushes, consisting of springs and damper elements.

The *Kelvin-Voigt model* is the standard element for modelling elastomer parts in MBS-Software tools such as Adams™, Simpack™ or Virtual Lab™. It fits the stiffness characteristics adequately enough and the input parameters can be easily derived from experimental data. For this simple model, the rate dependent dashpot element leads to a strong linear increase of the loss angle over frequency, whereas the measured loss angle increases just slightly. Therefore, the model's damping characteristics are only correct around one specific frequency point of reference. So, the model parameters are tuned for the correct loss angle around a chosen reference frequency (usually 10 or 15 Hz).

Figure 1-6 presents measured stiffness and loss angle data for an elastomer bush and shows simulation results for different model parameters, using this standard Kelvin-Voigt linear spring-damper model. The model was tuned to meet the measured loss angle at 5Hz, 10Hz, 15 Hz or 40Hz. Figure 1-6 illustrates that the fit for stiffness versus frequency is reasonable (left) but the damping characteristics are only a rough estimation (right).

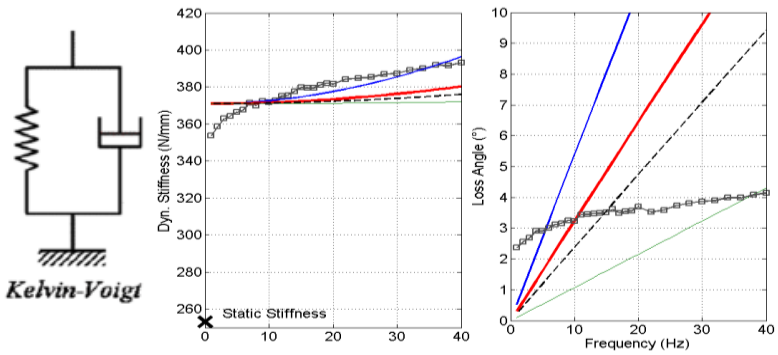

Figure 1-6: Evaluation of standard model for bushing elements: Measurement (markers) for stiffness (left) and loss angle (right) over frequency for one amplitude 0.2mm. Simulation results (lines) with different parameters to meet the loss angle at 5 Hz, 10 Hz, 15 Hz or 40 Hz. Simulation is identical for all excitation amplitudes.

The loss angle and therefore the damping characteristics only fit the experiments for one frequency point, depending on model parameters. At higher frequencies the predicted damping becomes much too high whereas the stiffness hardly changes. Using this standard model, frequency dependence is inaccurate. Furthermore, the amplitude dependent characteristics of the elastomer are entirely neglected with such a linear model approach.

A simple spring damper model is a very rough simplification. Because many bushes are in the load path from road excitation via the suspension and chassis to the driver seat, their representation highly affects overall vehicle simulation accuracy. For modelling bushes the amplitude dependence due to the Payne effect should be taken into account for more accurate overall results.

Researchers have developed many modelling approaches to take into account the amplitude dependence and some are used in Finite Element Analyses, but hardly any are available in

commercial MBS software tools. Here, computing times are limited, the model parameters need to be derived quickly and discontinuities of certain approaches may lead to numerical stability issues or unexpected behaviour after the numerical implementation. Several approaches do work well for principal investigations in academia or for FEA programs—where computing time and effort for model parameterization is not as restricted—but are not suitable for MBS implementation and full-vehicle studies in the early phase of vehicle development.

The challenge is to offer very flexible models for different types of mounts and bushes, and various fields of applications. For the models to be of practical use, a clear description of the parameter identification process or user tools to derive model internal parameters from measurements are crucial. The following scheme shows the process from characterisation of the component to model parameter estimation and simulation with the full vehicle model.

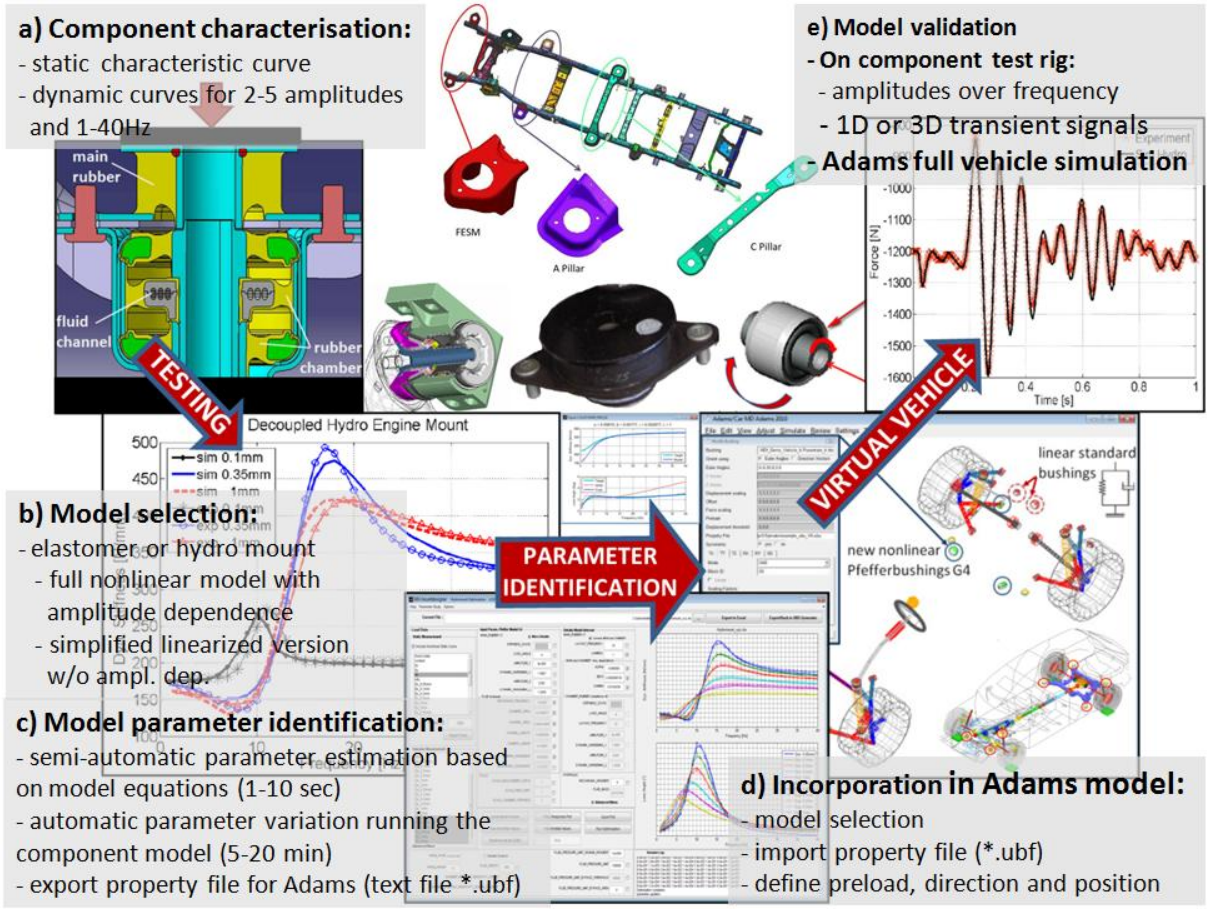

Figure 1-7: Scheme for the entire development process: a) component testing → b) model selection → c) parameter estimation → d) incorporation in full vehicle model → e) model validation on component test rig and/or full vehicle simulation

1.3 Objectives

There is a great need and demand for more accurate and practical mount models for full-vehicle simulation. This thesis discusses the development of new models for mounts and bushes and their use within the commonly used MBS environment MSC.Adams/Car.

The aim of this research is to develop new mount models, which take into account amplitude dependent behaviour due to the Payne effect. The models should give a good fit for many different combinations of parts and areas of use, where the frequency and amplitude range of interest may be different. Two types of models are discussed, one for simple elastomer bushes and a more complex model for hydraulically damped mounts and bushes.

In order to assess the potential for improvement in the context of full-vehicle simulation, the models should be implemented into an MBS environment with full functionality and usability. The model parameters are derived for all relevant mounts and bushes in three axes such that they can be used in a full-vehicle simulation. Model implementation into MBS requires essential numerical improvements or simplifications that are to be described.

This research focuses on how to model the dynamic behaviour of elastomeric and hydraulically damped mounts and bushes of vehicles, under the assumption that their behaviour is known from standard experiments under quasi-static and sinusoidal excitation. Design geometry and material blends are not studied in detail but the model has to correctly predict the mounts' behaviour under transient excitation within a MBS simulation environment. Model parameter estimation is briefly discussed, and user tools have been developed, to calculate model parameters from experimental data and export parameter files to MBS software.

1.4 Methodology, Software Development and Outline

The literature review in **Chapter 2** reveales the potential for an improvement in the overall simulation process. In this programme of work a series of experiments were carried out to assess various material effects of elastomer bushes with regards to bush elements in MBS simulation; the characteristics have been measured in all directions for nine types of mounts in a passenger car. Experiments at the component level have been carried out at industry partner Contitech Vibration Control. Hereby, the author was responsible for design of experiments, further processing of raw data and to define formats. To ensure accurate results the experiments have been carried out at various test rigs and the test rig setup and hardware was gradually improved.

The data was used to develop new models and to derive model parameters for a large variety of mounts and bushes. The following on-road experiments were entirely provided by industry partners Audi and Magna Steyr Fahrzeugtechnik, the author was responsible for further-processing of data.

The actual software development has been carried out by the author using *Matlab/Simulink*™. Next, the newly developed models have been parameterized and then exported in *C-code* as *General State Equations* to carry out analyses within *MSC.Adams/Car* and to validate the model performance. During the early first steps of model development and subsequent use within *MBS,* certain numerical issues were revealed and were solved in the next step of code development in *Matlab/Simulink.*

In **Chapter 3** the models are briefly described and significant improvements and methodical findings for numerical implementation are discussed. A practical method for linearization has been developed, so that the user can chose between the full non-linear model or a linear frequency dependent model version. *Scheiblegger et al. (2012)* briefly describes the new elastomer mount model and discusses the parameter identification process for the frequency dependent linear part of the model. Beside the fundamental model, essential numerical improvements for model implementation into MBS are described.

Chapter 4 and *Scheiblegger et al. (2011 -in German)* evaluate the performance of the early model approach within a full-vehicle simulation. A 4-poster analysis has been carried out to show the potential of improvement due to the new non-linear elastomer models. This study focuses on the ride comfort of a passenger car, so that excitation amplitudes are rather small and loading conditions hardly change during the tests. At this stage models were not of practical use for the daily development process because the parameters can't be changed after code generation and parameter identification was carried out manually by the author.

Paper A in **Chapter 5** describes the latest elastomer model in detail following numerical improvements. Besides the main model, a virtual test rig is needed and user 'masks' for the MBS environment were developed. The format and logics to read in parameters via property files were also established. For practicality, user tools have been programmed for import/export of measurement and property files and quick automatic parameter estimation for the elastomer. These new tools were used for this study to find parameters for three different elastomer cab mounts in three directions. Beside the model description, **Paper A** introduces these user tools and validates the model for higher deflections for durability load analyses of a body on frame vehicle; the entire process to load measurements, export files to

MBS, change directions and choice of a different parameter set for the specific study has been validated.

Paper B1 in **Chapter 6** discusses hydro mount behaviour in detail and suggests a new model for all types of passively damped hydro mounts and hydro bushes. For practicality and usability of such complex models, the parameter optimisation routine is crucial and the developed tools are validated with regards to usability and accuracy. This research concluded that, for model accuracy, it is essential that the amplitude dependence of elastomer parts is taken into account. Paper B1 was republished by invitation to make the content available for a wider public (**B2**).

Paper C (Chapter 7) describes the extension of the linearised hydro mount model for active engine mounts (AEM). For active hydro engine mounts, the relevant amplitudes are much smaller whereas the operating frequency range is much higher; here the amplitude dependence is neglected and practical linearization of the hydro model is needed. The model is used to study secondary path variations of AEMs. For this principal investigation, the parameter identification was only carried out for one specific mount and no user tools or actual implementation in MBS is available for AEMs.

In this thesis, model validation is mainly achieved by test rig analyses with sinusoidal excitation and excitation profiles that were derived from on-road tests. For model validation in an MBS environment, the models are used to calculate durability loads of a pick up truck. In **Paper D (Chapter 8),** the model implementation itself, the method to derive model parameters from standard experiments and user masks in MSC.Adams are described. Numerical stability and the practical usability of the approach in MBS environments are presented.

2 STATE OF THE ART

This chapter discusses the wider context of the investigated research area and gives an introduction into the topic. The literature review clarifies the state of the art for full-vehicle simulation using MBS software environment and explains the entire simulation process. Next, the behaviour of elastomeric mounts and bushes is discussed and known mathematical models and methods to describe their frequency and amplitude dependent properties are discussed. Different types of hydromounts are explained and a popular model approach is introduced. The challanges and the potential for improvement of available mount models are assessed.

2.1 Full-Vehicle Simulation

2.1.1 Road Excitation and Ride Comfort

Vibrations at the driver seat are caused by engine disturbances through the powertrain mounting system and by road excitations via the tyres' suspension system with its bushes and mountings. *Mitschke and Klingner (1998)* introduced a model for the evaluation of vibration comfort that categorises road excitations into:

- Stochastic road inputs containing a wide amplitude range and primarily causing vibrations up to 20 Hz.
- Periodic excitation e.g. due to road surfaces like concrete paving slabs that are usually five meters long. Here the excitation frequency is proportional to vehicle speed.
- Transient excitation through single obstacles like potholes or railroad crossings that cause freely damped vibrations.

The typical parameters to objectively evaluate ride comfort are the maximum acceleration at the driver seat and at the steering wheel on uneven roads or when driving over single obstacles. The acceleration signal is then further processed and weighted with respect to amplitude and frequency content in regards to perception sensitivity of the human body (ISO 2031, VDI 2057).

To assess which vibrations affect the passengers, *Gan et al. (2015)* present a new model for a seated human body on a car seat. Fischer and *Meywerk (2013)* have introduced a method to derive subjective evaluation criteria from objective measurement data, using neural networks. However research concerning the correlation from objective measurement to subjective evaluation remains a challenge (see also *Lennert (2009)* and *Stammen (2009)*).

Mischke (1987) has analytically studied the impact of changing road profiles on ride comfort, using two-dimensional multiple degree-of freedom (DOF) models. *Gao et al. (2008)* use a

quarter-car model to study the car response when the sprung mass, unsprung mass, suspension damping, suspension stiffness, and tyre stiffness are considered as random variables. *Georgiou (2007)* present a multi-object optimisation method for such analyses. However, the highly simplified nature of quarter-car models neglects the non-linear behaviour of suspension dampers, tyres and hydro mounts.

2.1.2 Simulation Process

Many researchers have considered the issues associated with the simulation of vehicle system dynamics including *Cao et al. (2011)* who discusses general design aspects for suspension components and vehicle dynamics in a wider context. *Rauh (2003)* describes the virtual development process for ride and handling characteristics while *Botev (2008)* presents the state of the art for the overall development process for ride comfort and handling in detail.

The validation process of MBS vehicle model is explained in *Falkner and Reinalter (2005, 2006)* and *Hammer et al. (2003).* In general, Multi Body Simulation models provide good relative correlation comparisons e.g. regarding different types of mountings or various road excitations. Vertically, the maximum displacement and attenuation are simulated accurately. But for optimising the coupling of the power unit and suspension, it is crucial to further improve model performance. *Ohlendorf et al. (2000)* explained a method to improve ride comfort by systematically coupling the various mounts used for the power unit and the suspension. In this approach, the power unit is wilfully used as a tuned mass damper (TMD). They state that longitudinal movement at the driver seat can be as significant for road comfort as vertical vibrations. Particularly for longitudinal vibrations, the vehicle simulation currently has high potential for improvement.

The *tyre models* in MBS highly affect accuracy but also computing time and the effort required for accurate parameter identification is significant. *Lugner et al. (2005)* compare some tyre models and *Pacejka (2002)* gives further insight into the topic. *Gibser (2005)* has introduced the FTire model that is widely used for such analyses while *Riepl et al. (2005)* described the virtual development process with the FTire model and the steps required for ride comfort simulation. During simulation, the car virtually follows a given path on the track. Besides the car's components, the virtual driver model must also be accurate to ensure vehicle speed and position are equal to the measurement data from on-road testing. *Plöchl and Edelmann (2007)* present a comprehensive literature review concerning human driver models.

Beside ride comfort, durability analyses are another area of use. *Yang and Xu (2012)* describe the state of the art for road load analysis. *Roy and Villaire (2013)* have described the full-

vehicle simulation process using FTire and a PID driver model for a body on frame vehicle, in an attempt to replace on-road testing by simulation. Model validation proved that the excitation at the wheel carrier was correct. However, in order to further analyse the load-path over the suspension/frame into the body, the overall level of detail needs to be increased—so body mounts and engine mounts become particularly relevant.

Ambrosio and Verissimo (2009) use MBS simulation to analyze how the bushing characteristics have an impact on ride comfort for a compact size car while *El Hafidi et al. (2010)* study the best positioning of the engine mounts to reduce vibration in city busses. Both use spring-damper simplifications for the bushing elements. *Lewitzke and Lee (2001)* give an overview about different sorts of elastomer components in cars, testing methods, material compounds and basic modelling methods.

Yang et al. (2004) focus on the engine mount load prediction, where the entire powertrain's vibration is analysed. The simulation results—using linear mount models—are accurate enough for quantitative comparison, but also show high potential for improvement. Beside the engine mounts, suspension bushes affect many relevant vehicle characteristics. *Yang (2011)* has studied the impact of bushing properties on suspension ball-joint travel and concludes that non-linear stiffness characteristics have a high impact. Therefore, all bushing elements should be modelled as accurately as possible, with reasonable effort for parameter identification and testing.

2.2 Modelling Elastomer Behaviour

2.2.1 Linear Frequency Dependent Models

Maier (2006) gave a brief overview of currently used models for elastomer parts within MBS software packages for vehicle comfort simulations. In his thesis, the following basic linear model approaches for the linear viscoelastic, frequency dependent behaviour are mentioned: Kelvin-Voigt model; Poynting-Thomson model; Dual-Kelvin-Voigt model; Dual-Poynting-Thomson model. (*Maier 2006: pp.38-39*). The following figure shows several such linear models and qualitatively gives simulation behaviour versus frequency, where the reference layout frequency for parameterization is marked.

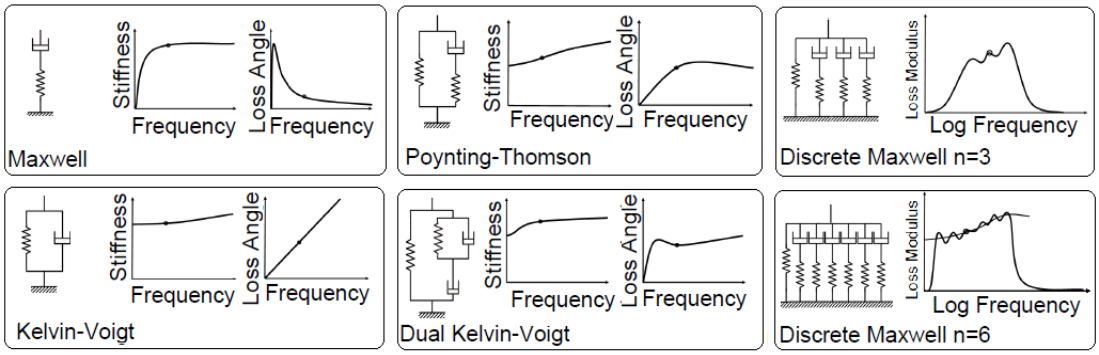

Figure 2-1: Qualitative representation of linear basic models simulation results

In the Kelvin-Voigt model, a spring (*k)* is parallel to a dashpot element with damping coefficient *c*. The overall force of this model is:

$$F = k \cdot x(t) + c \cdot \dot{x}(t) \qquad (2\text{-}1)$$

In the frequency domain, with the excitation frequency Ω (rad/s), the resulting dynamic stiffness k_{dyn} and loss angle δ are as follows:

$$k_{dyn} = \sqrt{k^2 + \Omega^2 \cdot c^2} \qquad (2\text{-}2)$$

$$\tan(\delta) = \frac{\Omega \cdot c}{k} \qquad (2\text{-}3)$$

The spring may represent the static stiffness characteristics with a progressive curve, so that *k=k(x).* In the Figure 1-6 (page 15) the results of a Kelvin-Voigt model were shown for different layout frequencies where simulation meets experimental data. Lower frequencies lead to negligible damping and for high frequencies the calculated damping is much too high.

A single *Maxwell-element* can properly simulate the relaxation behaviour over time, but after excitation the damper would stay in its position. This behaviour is plastic deformation and would not fit for elastomer parts, but this element is widely used in combination with other elements.

Giesekus (1995) gives an overview of additional multi-element models for linear viscoelastic materials. *Stommel (1999)* points out that in principle any combination of springs and dampers can be extended into a continuous Maxwell chain with an unlimited number of elements.

The Dual Kelvin Voigt model offers a good compromise for stiffness and damping over a wide frequency range after start-up effects at low frequency. It will be discussed later when parameter identification at a range of frequencies is considered.

2.2.1 Amplitude Dependent Models

A combination of spring and damper elements can be used to simulate a bush's properties as a function of frequency however additional non-linear effects lead to additional amplitude dependent properties. In this section non-linear elements and models to cover this amplitude dependence are discussed.

If a spring element is in series with a Coulomb-friction component, this is often referred to as a Prandtl-element. Figure 2-2(a) schematically gives the model behaviour with discontinuous force development. Several Prandtl-elements in parallel form a discrete Masing element as shown in (b).

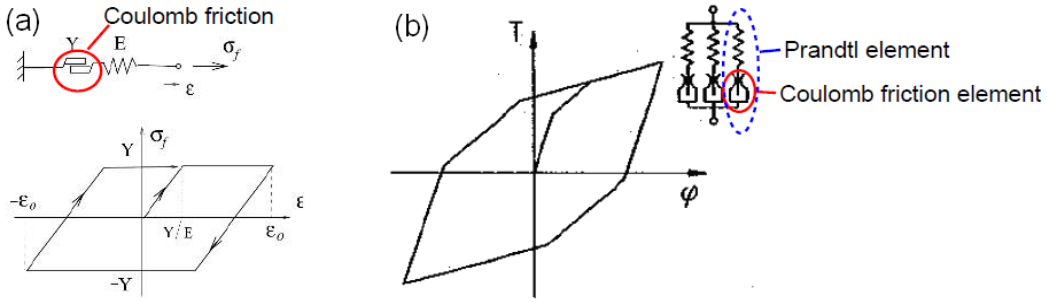

Figure 2-2: Shape of hysteresis for basic Prandtl element (a) and hysteresis for three-element discrete Masing model (b). (modified from Karlsson 2003, p.12 and Ziegenhagen 1994, p.4-2)

Japs (1979) combined the non-linear Masing approach with a discrete Maxwell-chain for frequency dependence as shown in the following figure. *Kümmlee (1986)* puts the Coulomb friction elements in series with Maxwell elements.

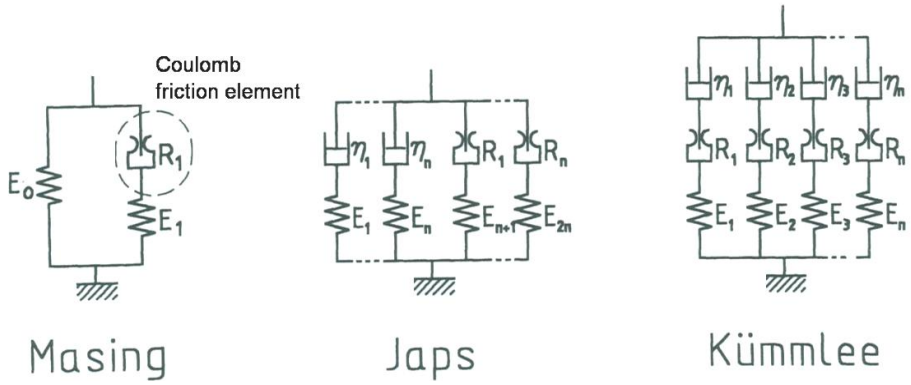

Figure 2-3: Non-linear models with Coulomb friction elements (Lambertz 1994, p.69)

These three models are capable of modelling the amplitude dependence and are implemented in FEA-software but are unsuitable for MBS standard analysis software because of the discontinuous force development of Coulomb element. MBS software such as ADAMS solves differential equations using direct time integration. *Arnold et al (2011)* study numerical methods for MBS simulation and discuss the variety of mathematical methods to solve

constrained multi-body equations. Explicit and implicit multistep methods for the time integration of stiff and non-stiff problems are discussed and evaluated for their performance. Arnold's paper gives insight into numerical details and discusses issues due to stiff formulations for calculation of the friction force.

Williams and Whear (2005) eliminated the disadvantages of discontinuous Coulomb friction forces, using several *non-linear Maxwell-Elements* in parallel. Klingenberg (2001) used a broken rational hyperbolic function to model the friction force. The friction force converges to a maximum value and thereby relaxation is also taken into account.

To describe static hysteresis *Berg (1997, 1998)* uses a hysteresis function without relaxation over time that could be seen as a smoothed Coulomb friction element. The papers provide Matlab code and describe parameter estimation well. In parallel with viscous damping and a spring for the static stiffness, the amplitude dependence is well simulated. Bergs friction force for increasing displacement x is:

$$F_{frict} = F_{fs} + \frac{x - x_s}{x_2(1-a) + (x - x_s)}(F_{f\max} - F_{fs}) \tag{2-4}$$

For decreasing displacement x:

$$F_{frict} = F_{fs} + \frac{x - x_s}{x_2(1+a) - (x - x_s)}(F_{f\max} + F_{fs}) \tag{2-5}$$

The two parameters defined by the user are the maximum friction force F_{fmax} and the displacement x_2 where half the maximum friction force is developed. The parameters F_{fs} and x_s are set as the force and displacement starting points for each loop where $a = F_{fs}/F_{fmax}$ *and* ranges from -1 to 1.

Berg's original model lacks accuracy for higher frequencies due to its simple spring-damper approach for frequency dependence, but the friction force formulation has been used in many following publications. *Sjöberg (2002)* and following studies from *Karlsson and Persson (2003)* use fractional derivatives to model frequency dependence and have adopted Berg's friction force. More recently similar approaches have been further developed by *Dronka and Rauh (2007)* and *Sedlaczek et al. (2011).*

Bahnert (2008) developed a model for suspension dampers. He used the friction term from Dronka and Rauh (2007) with a Dual-Kelvin-Voigt model for frequency dependence. Einsle and Steinert (2008) use separated progressive spring elements for compression and tension in combination with backlash to model the dynamic stiffening of strut mounts.

Beside passenger cars, the simulation of rail vehicles faces the same challenges and the mount models can also be used for commercial vehicles, airplane suspension and many other applications. Yarmohamadi and Berbyuk (2010) present an elastomer mount model for use in commercial vehicle. Their friction force calculation goes back to the approach of Berg and a parameter estimation method is described to derive model parameters. *Eickhoff et al (1995)* and *Bruni et al. (2011)* present different model approaches for all sorts of suspension components for rail vehicles and *Waltz (2005)* discusses the most commonly known model approaches for elastomer models in more detail.

Modelling Approaches for Three-Dimensional Stress

So far, the majority of modelling approaches based on rheological basic elements (spring, damper, coulomb friction) were discussed. Additionally, there are mathematical or material modelling approaches.

Banks et al. (1999) gives a detailed validation for a model for uni-axial stress under quasi-static and dynamic testing and Banks (2008) presents an overview of modelling approaches for constitutive elastomer models.

Material models for hyperelasticity can predict the non-linear strain-stress behaviour (static stiffness) and approximations for the stress level under three-dimensional excitation to couple directions. Some approaches are discussed in Stommel (1999) and MSC.Marc (2000).

Böhm (2001) presents constitutive model for the Payne effect that is valid for different sorts of fillers. Other three-dimensional material models and their implementation for FEA software are studied in Ludwig (2001), Lion and Kardelky (2004), Lion 2006; Haupt 2001, Sedlan 2000, Rendek 2009 and Rendek (2011).

Barber (1999) presents an empirical dynamic modelling (EDM) approach for mounts, bushing and shock absorbers. Here, a black-box model is used and parameters are identified with neuronal-networks. Steinweger and Weltin (1998) discuss another empirical 3D approach for use in an MBS environment.

Material models or empirical models are not used for this study because of restrictions in computing time and because the models have to be parameterized based on few standard experiments – without studying design and material blends.

Logarithmic Force Increase

Peeken and Lambertz (1994) developed the so-called rho-model for elastomer behaviour. Here a logarithmic function is used for the non-linear force that ensures a continuous force increase and fits measured hysteresis very well. The dynamic hardening with amplitude is modelled very accurately and the resulting loss angles with amplitude also give the right trend. In combination with a time-dependent relaxation equation, the model takes static and viscoelastic effects into account. *Stommel (1999)* has further developed and extended this model approach for three-dimensional stress. *Ludwig (2001)* has slightly modified the Lambertz friction force and has implemented a three-dimensional material model into the FE-software ABAQUS. *Weidemann (2002)* has used the roh-model for rubber parts in railway trains for an MBS environment. *Gold et al. (1996)* use Lambertz friction force to describe elastomer clutches and implement it in a simulation tool for drive trains.

In the Lambertz model, the frequency and amplitude dependent behaviour are coupled and an additional time dependent relaxation force is used. To calculate the relaxation time history requires further processing, leading to increased computing time and complexity; numerical implementation is difficult. If the relaxation with time is used, frequency dependent and amplitude dependent behaviour are both affected. For simplification for a practical elastomer model in an MBS environment, *Pfeffer and Hofer (2002)* used the logarithmic force increase for amplitude dependence without relaxation and modelled the linear viscoelastic behaviour separately with a Dual-Kelvin-Voigt module. The frequency dependence is now accurately described and the model is very flexible for different parts. This modelling approach has been used as a starting point for further analyses in this research and will be discussed in detail in Chapter 3 and Chapter 5 (Paper A) .

2.3 Hydro Mounts

2.3.1 Hydro Mount Behaviour

An engine mount must meet several conflicting criteria. The mount has to carry the static gravitational load of the engine and it supports the engine torque. It should isolate engine vibrations and prevent engine bounce from shock excitation. To isolate vibrations caused by engine disturbances, low stiffness and low damping are needed because the force transmitted to the body is proportional to the stiffness and damping of the mount. Thus, low stiffness is

needed for high frequencies. On the other hand, a hard mount—high stiffness and high damping—is needed at low frequencies to reduce engine displacement caused by shock excitations.

Hydraulically damped mounts use the tuned mass damping effect (TMD) and additional fluid damping to generate high dynamic stiffness and high damping around the tuned resonance frequency. Hydro mounts change their dynamic stiffness and damping properties very significantly with both frequency and amplitude. At high excitation the movement of the cab or powertrain are limited and simultaneously damped. The fluid mass inside the channel, the rubber stiffness and chamber compliance are tuned to give high damping at certain resonance frequency.

Yu et al. (2001a) published a literature review on automotive engine mounts that gives an overview of different types. Figure 2-4 shows a range of hydro engine mounts:

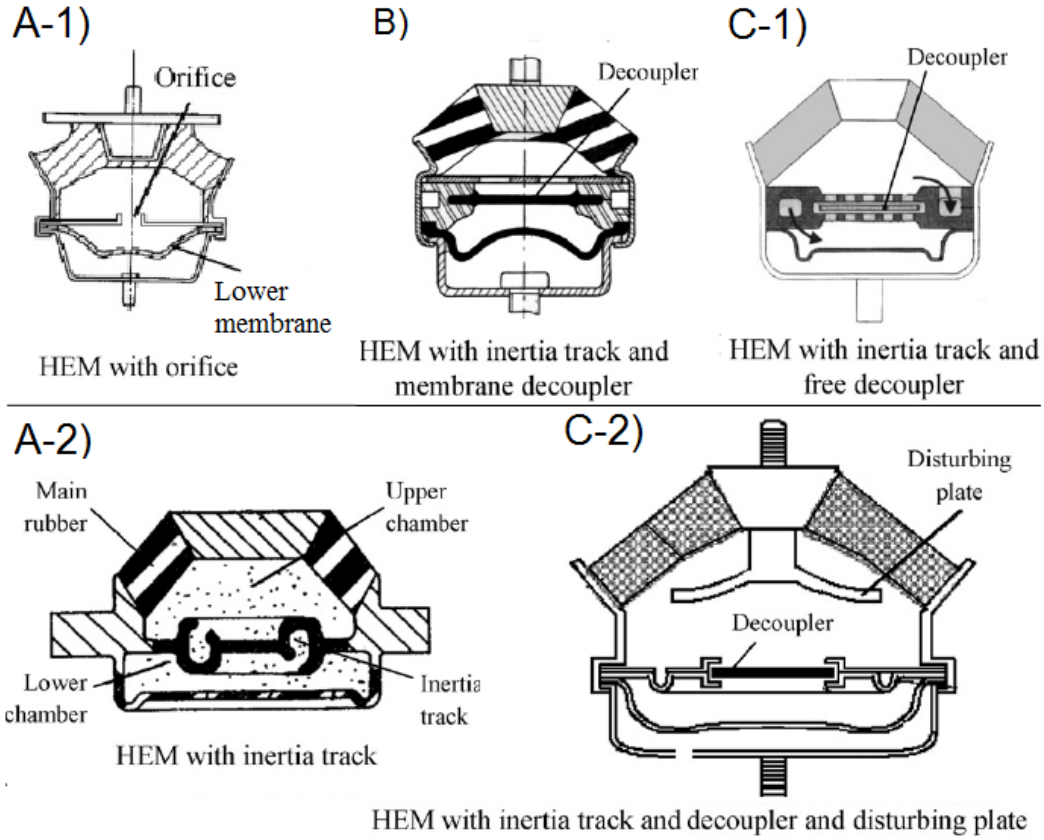

Figure 2-4: Types of passive hydraulic engine mounts (modified from Fan and Lu 2007, p.108).

The simplest form of hydro mounts with only an orifice (A-1) is unusual and most passive mounts have an inertia track (A-2). They offer superior damping compared to elastomer mounts. However, simple passive HEMs cannot meet all the requirements at high frequencies.

Engine disturbances that should be isolated from the car body are of high frequency but low amplitudes. To isolate the engine vibrations the stiffness should be lower, because energy

submitted into the car body is directly proportional to the mounts' stiffness. For this purpose the hydraulic system can be fully or partially decoupled at small amplitudes. Passive HEMs with a soft decoupling membrane (B Figure 2-4) slightly reduce their overall stiffness for small amplitudes at high frequency.

Figure 2-5 schematically gives stiffness characteristics for different types of hydro mounts and hydro suspension bush.

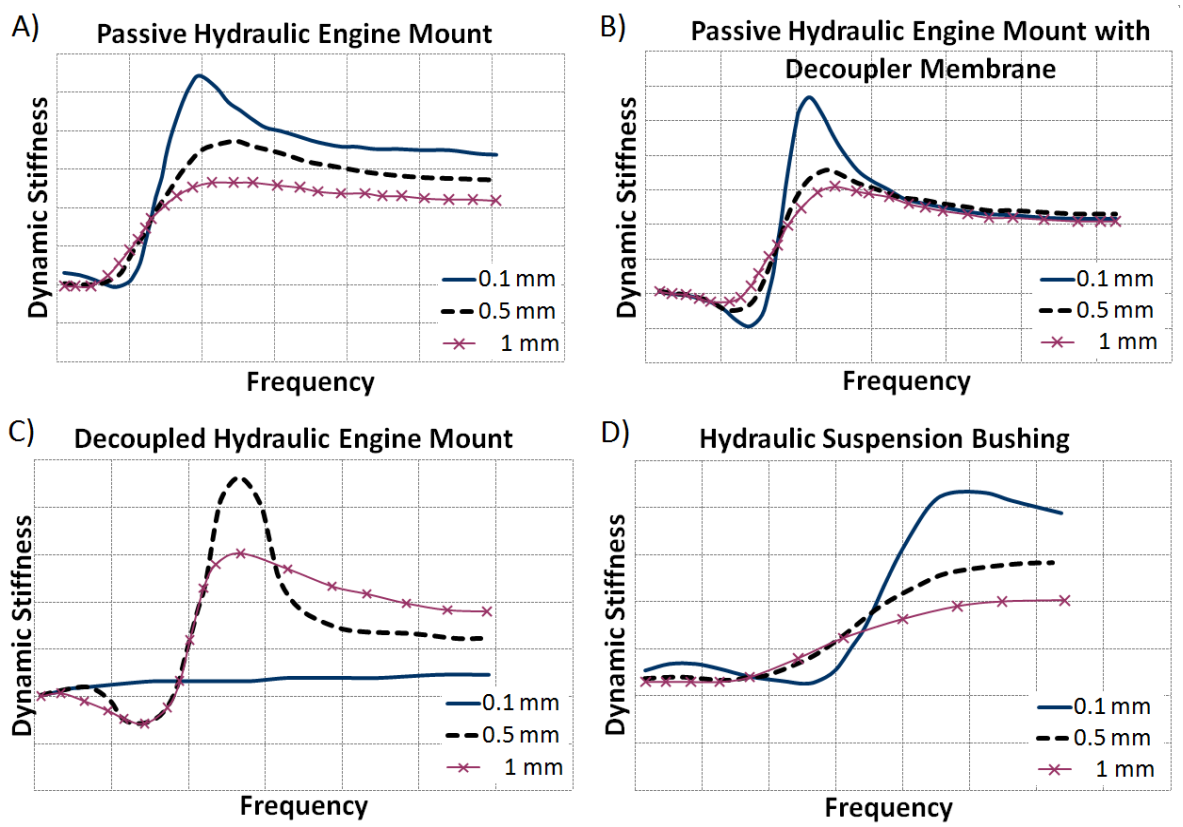

Figure 2-5: Frequency response for (a) hydraulic engine mount (HEM) with inertia track, (b) soft decoupling membrane; (c) fully decoupled HEM, (d) hydraulic suspension bushing

Compared with simple passive HEM (A), mounts with a soft decoupling membrane show significantly lower stiffness at small amplitudes (type B).

Type C (Figure 2-5) is a fully decoupled HEM where amplitudes <0.2mm show the same behaviour as its underlying main rubber part; the hydraulic part is not active at small amplitudes so that stiffness increases linearly with frequency. Passive engine mounts with a decoupler show good performance when subjected to simple sinusoidal inputs but several papers report that the results might be less promising for superimposed inputs or single obstacles. Because of the non-linearity due to the decoupler, their transient behaviour cannot be easily predicted from standard tests in the frequency domain (Yu et al (2001), Singh et al. (2002), Lee et al. (2004))

Hydraulically damped suspension bushes (D, Figure 2-5) usually have significantly smaller fluid channels and sometimes exhibit bypass valves that restrict the internal pressure (Sauer and Guy (2003)). Stiffness changes more smoothly with frequency and damping is available over a wider frequency range. Furthermore, the behaviour may highly dependent on the preloading conditions, e.g. changed stiffness during braking manoeuvres.

In *active hydraulic engine mounts* (AEM) the characteristics are constantly controlled to counteract vibrations and improve ride comfort across a range of operating conditions. Figure 2-6 shows a cross-section of an AEM with a moving magnetic coil.

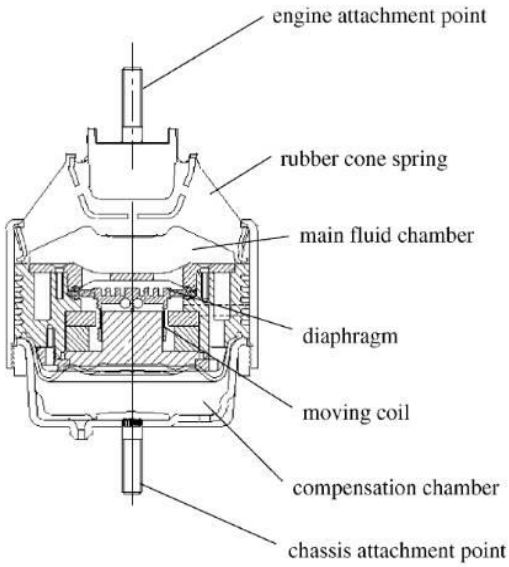

Figure 2-6: Active hydro mount with diaphragm and moving coil (Hillis et al. 2005, p.38)

Currently, AEM are mainly used in highly priced cars with cylinder on demand technology (COD). In COD engines, part of the engine is deactivated to improve fuel efficiency at low engine load. E.g. a six cylinder engine partially runs only on three cylinders during the shut-off phase. In the other cylinders, the valves are closed so that only air is compressed without injection or ignition. Engine disturbances can be significant during the two- or three-cylinder mode and during the switch phase where cylinders are de- or reactivated.

2.3.1 Modelling Hydro Mounts

Research into hydro engine mount models for MBS has been conducted recently by *Kramarczuk (2012)* for load analyses at VW. Other hydro mount models are suggested by *Lee and Kim (2005), Lee and Singh (2008), Whear and Williams (2005), Barker (2004)* and *Fan and Lu (2007).*

Foumani et al. (2003a) (2003b) use a combination of numerical methods and experimental analyses with a simple mechanical model to study the optimal characteristics of hydro engine

mounts. *Christopherson and Jazar (2006a)* discuss the dynamic effect of two different decoupler designs for passive decoupled hydro mounts and carry out an FEA analysis of the rubber characteristics to derive model parameters *(2006b).*

The most commonly used approach in MBS environments goes back to *Weber (1998)*. Figure 2-7 shows this standard hydro mount model that is implemented in the MBS software tool *MSC.Adams/Car*.

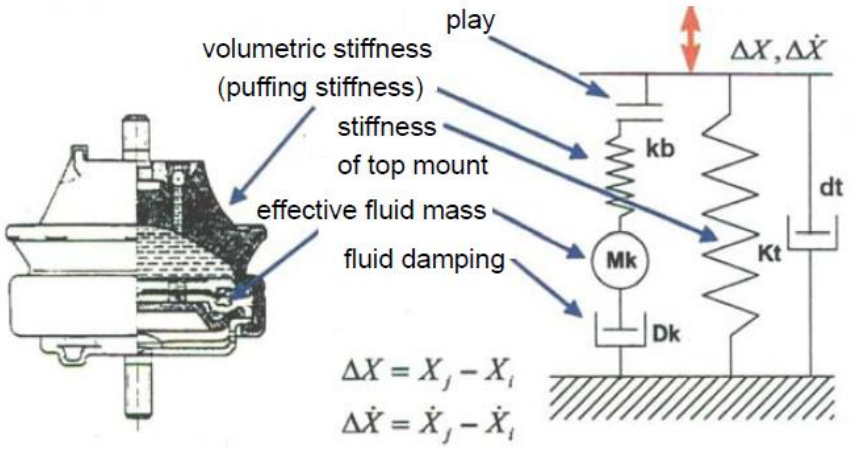

Figure 2-7 ADAMS standard hydro mount model used at AUDI (Originally from Weber 1998, p.9)

The damping and stiffness provided by the top mount are modelled with a simple Kelvin-Voigt module with spring rate *Kt* and damping coefficient *dt*. Therefore, the top mount behaves only in a linear viscoelastic manner; amplitude dependence is neglected.

The hydraulic system is modelled separately in parallel to the top mount stiffness. Here, the puffing stiffness kb is applied as a linear spring without any damping. In series is a mass *Mk* that represents the dynamic tuned mass damping effect due to the fluid pulsation in the channel. The damper *Dk* represents the viscous fluid damping in the fluid channel. 'Play' or backlash is used to simulate the decoupling effect at very small amplitudes.

The model predicts a standard passive hydro engine mount's behaviour well but the results are less satisfactory for decoupled engine mounts. The clearance/play element may lead to stability issues and gives only a rough estimation of the real behaviour for partly decoupled mounts. Furthermore, the model is not accurate for hydraulically damped suspension bushes.

For hydro mount models an automatic parameter optimisation routine is crucial to tune unknown model parameters to give a good fit to experimental data. Unfortunately, model performance cannot realistically be predicted from studying research papers; instead, the details of numerical implementation and parameter fitting software are crucial. Some models are limited for certain types of hydro mounts. Others need input parameters that are usually not available or lack a practical approach for easy, fast and stable parameter identification

processes. None of the above mentioned models seem to be accurate for all the different types of mounts. Results are often accurate enough for simple passive HEM but less promising for decoupled HEM and inaccurate for hydro suspension bushes.

2.4 Conclusions of Literature Review

While many papers suggest that non-linear models are required to take into account amplitude dependence, there is no practical approach available within commercially offered software tools. Several non-linear model approaches have been tested within MBS environments as user-sub-functions—with limited practicality—but only a few have been implemented into commercial MBS environments with full functionality.

SIMPACK offers an amplitude dependent elastomer model 'Dynamic Bushing' *(Simpack 2010; Zeman 2009)*. Within Adams/Car Ride (MSC 2015) a simplified Dual Kelvin-Voigt model is available for improved frequency dependence, referred to as 'Frequency Bushing'. Meanwhile, a' General Bushing' model is available in Adams/Car Ride which uses the Bouc-Wen model for hysteresis (Kang et al. 2010) for amplitude dependence; this software had not been available during this research. The accuracy seems promising but users reported that the parameter identification process is not fast enough and unsatisfactory for certain mounts.

Coulomb friction elements, clearance/play and other approaches reveal numerical stability issues after implementation into an MBS environment due to discontinuities. The continuously increasing friction force from *Berg (1997)* and the overall model suggested by *Pfeffer and Hofer (2002)* appear to be practical for MBS applications. However, some users report unexpected behaviour under superimposed sinusoidal excitation or transient excitation. The research lacks detail concerning the cause of unexpected phenomena associated with non-linear modelling approaches. Therefore, a new practical model for elastomer mounts has been developed and implemented into an MBS environment.

For any model to be of practical use, the user must be able to easily and rapidly derive model internal parameters from user inputs, based on experience or standard measurement data. An automatic parameter estimation routine is needed that derives model parameters from experimental data within a few seconds. Parameter estimation should be based on given equations from the frequency domain and therefore very fast.

Hydro engine mounts also mainly consist of rubber parts, which significantly affect the overall behaviour. Thus, any model for hydro mounts should take into account amplitude dependence of the rubber itself for accurate results. Many similar lumped mass model

approaches are suggested, but the Adams hydro mount model and most papers neglect the underlying elastomer parts' amplitude dependence due to the Payne effect. Others include discontinuous elements that are unsuitable for MBS. Research focuses on specific types of engine mounts but no model seems sufficiently accurate for the full range of hydro mounts.

Hydro mount models are more complex than elastomer models. The model is designed to accurately predict the behaviour when the real design parameters like the fluid channel length and area are given. However, that's often not of interest for the user and several internal parameters like fluid damping coefficients or volumetric stiffness are not known. To be of practical use, these model parameters have to be automatically tuned to meet the measurement data. For this parameter optimisation, the simulation is run multiple times while the model internal parameters are tuned. Here, a real simulation needs to be carried out, taking into account non-linear static stiffness tables, solver settings etc. This makes it far more time consuming than elastomer models' parameter estimation.

The details of this process are crucial for a hydro mount to be of practical use; this process should be straight forward and easy and computing times below 20min are desired. The practical value of any hydro mount model highly depends on flexibility for many different sorts of mounts and the accuracy of this parameter optimisation routine. It is this challenge that this thesis aims to address.

3 SIMULATION MODELS

This chapter gives a brief overview of the elastomer model for mounts and bushes that takes into account amplitude dependence. Paper A (chapter 5, page 65) describes the model approach in more detail and assesses the use of the newly developed non-linear elastomer model for mounts and bushes to calculate durability loads in the context of full-vehicle simulation. In this Paper A the parameter identification process is briefly discussed, using the provided GUI.

3.1.1 Elastomer Model Structure

Static preload dependent, frequency dependent and amplitude dependent characteristics are relevant for modelling elastomers.

Progressive static characteristics can be taken into account via table data for static stiffness; this procedure is standard for all models for bushing elements so that changed preload leads to a different stiffness at the current operating point. For the linear frequency dependent parts, a dual-Kelvin-Voigt approach is accurate enough for normal frequency ranges - as shown later in this chapter and in chapters 4.2 and 5.1.

To take into account amplitude dependence, a logarithmic non-linear force increase was chosen for this study because it leads to very accurate simulation results for dynamic hardening over a wide amplitude range, even though only two input values are defined. Figure 3-1 shows the modular model structure with a linear part for frequency dependence (F_{lin}) in parallel with a non-linear part for amplitude dependence due to the friction force (F_{NL}). As in most papers, static, linear and amplitude dependent parts are modelled separately and the calculated forces are superimposed. Compared with alternative chain model approaches the model structure is simpler. As a benefit of this model, only a few model input parameters are needed, which can be easily derived from standard experimental data.

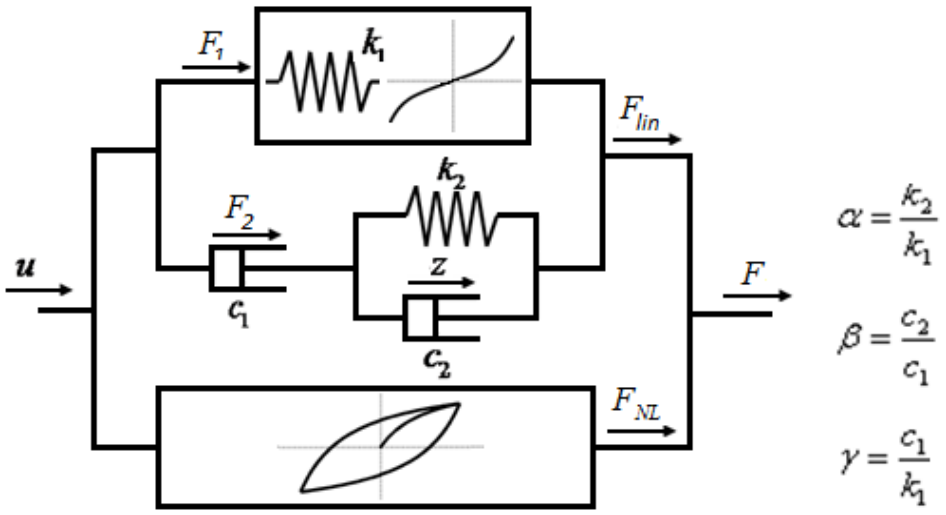

Figure 3-1: Model structure with linear, frequency dependent part in parallel to non-linear part for amplitude dependence.

k_1 represents the main spring, which may directly refer to the measured static stiffness k_{stat}. Non-linear static stiffness characteristics can be implemented here, so that k_1 is continuously calculated around the operating point from a table data approximation.

k_2, c_1 and c_2 are linear spring and dashpot elements that lead to frequency dependent behaviour. α, β and γ define the ratios of the spring and damper elements as given in *Figure 3-1*. In the model implementation, instead of using the spring and dashpot parameters k_2 c_1 c_2, all model internal parameters are referred to the main spring $k_1=k_{stat0}$ that can also be non-linear. Therefore, the same parameter combinations can be used and only static stiffness has to be changed for different mounts.

To understand the principal model behaviour and to be able to manually derive internal parameters, it is important to be aware of the modular concept as given in the following schematic representation. Displacement *s(t)* alone is the input required to calculate the static force F_{stat}. Frequency and amplitude dependent parts use a velocity signal *v(t)* as input and are scaled via the constant static stiffness k_{stat0} at the operating point from model initialization. s_0 is the displacement at this given design preload

The overall resulting force is calculated by superposition of the static force F_{stat}, frequency dependent linear force F_{LIN} and the additional non-linear friction force F_{NL} for amplitude dependence.

$$F = F_{stat} + F_{LIN} + F_{NL} \tag{3-1}$$

$$F(t) = F_{stat}(s(t), s_0) + F_{LIN}(\dot{s}(t), k_{stat_0}) + F_{NL}(\int \dot{s}ds, k_{stat_0}) \tag{3-2}$$

where *s(t)* is the actual displacement, including offset s_0 due to preload F_0. Preload is caused by a gravitational load or caused by pre-compression of the part. In the full vehicle model, the resulting displacement s_0 will be automatically derived from the given mass *m* on top of the mount.

3.1.2 Linear Frequency Dependent Element

If only the linear frequency dependent part of the model is used (F_{NL}=0) the resulting force $F=F_{lin}$ can be calculated using the following equation:

$$F = k_1\left(u + \frac{c_1}{k_1}\cdot\left(\dot{u} - \dot{z}\right)\right) = k_1\left(u + \gamma\left(\dot{u} - \dot{z}\right)\right) \tag{3-3}$$

where *u* is the overall displacement and $\dot{u}$ is the velocity. *z* is the displacement at the second spring k_2 and $\dot{z}$ is the derivative of *z*. In the frequency range, the linear force can be calculated as follows:

$$\hat{F}_{LIN} = k_{stat}\cdot\lambda\cdot\hat{U}\left(1 + i\Omega\gamma\left(1 - \left(\left(1+\beta\right) + \frac{\alpha}{i\Omega\gamma}\right)^{-1}\right)\right) \tag{3-4}$$

During the iteration process, initial starting parameters are chosen for α, β and γ, depending on the frequency range considered and the mount behaviour. In the practical model implementation, the parameters α, β and γ remain constant for many mounts and bushes and don't need to be changed. Instead, the frequency dependent part is scaled via an additional parameter λ. When the program iteration changes amplitude dependent properties, the impact of frequency dependent model elements is decreased using λ until the overall loss angle due to non-linear and linear contributions is reached.

The linear part of the model on its own can be used for frequency domain analyses or as a simplified model version *(Scheiblegger et al. 2012).* Even without the amplitude dependent friction part, the simulation gives a good fit for a small amplitude range, as shown in *Figure 3-2* for an elastomer cab mount. In this case, the stiffness k_1 (eqn 11) has to be greater than the measured static stiffness k_{stat} in order to reach the desired dynamic stiffness and compensate for the missing non-linear model part, e.g. k_1=355 N/mm versus a static stiffness of 250 N/mm in the example.

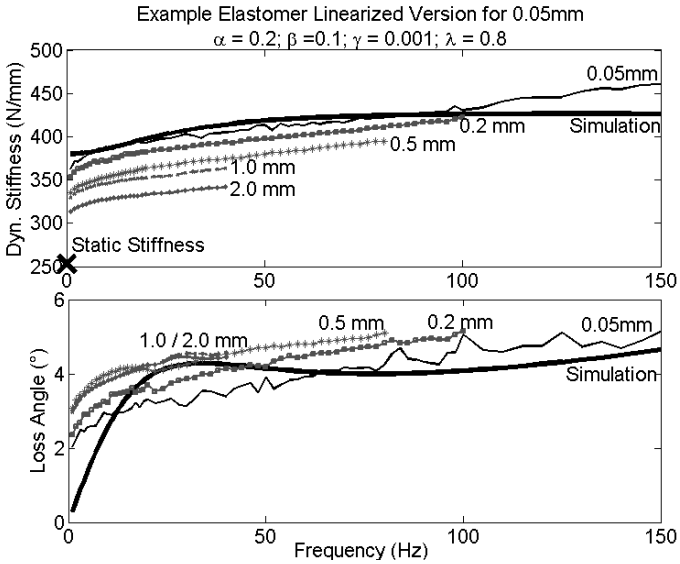

Figure 3-2: Evaluation of linear, frequency dependent model part: good fit for whole frequency range but simulation results are the same for any amplitude.

Compared with the standard spring-damper model (see *Figure 1-6 p. 15*), this linear model element already leads to improved accuracy, particularly for the damping characteristics. However, as with any linear model approach, the significant amplitude dependent properties are not taken into account but the model parameters have to be chosen in a way to offer a good trade-off for the whole amplitude range.

3.1.3 Non-linear Elements for Amplitude Dependence

To give a good fit for all amplitudes, an additional non-linear model part is needed. A logarithmic force increase was originally suggested by *Lambertz (1994)* and proved to be beneficial because it accurately maps the wanted dynamic hardening behaviour at sinusoidal excitation very well and also gives the correct trend for loss angle. Originally, the friction force had been defined as:

$$F_{NL}(u) = RDL \cdot \ln(1 + \rho \cdot u) \qquad (3\text{-}5)$$

The coefficient name ***R****DL* is taken from older model approaches, where ***R*** is a friction coefficient (‘*Reibung*’ in German) and *DL* indicates this coeffictent is valid for **d**ynamic **l**oad.

$RDL \cdot \rho$ defines the starting stiffness at very small excitation. ρ defines the decrease of stiffness with amplitude and *RDL* is then adjusted to define the desired stiffness. *Equation (*3-5) is only defined within one branch of the hysteresis loop; in between two turning points of motion.

The resulting non-linear friction force F_{NL} during sinusoidal excitation is shown in Figure 3-3. The starting stiffness (*A*) at zero offset and after a full cycle at -2mm are the same. After the

first turning point of motion (*B*) the slope of the non-linear force meets the starting point at *C*. The stiffness for the first half cycle *A*-*B*-*C* (+/-1 mm) is significantly higher than the overall stiffness for the whole cycle (+/-2 mm). Using this approach, the friction force is not symmetrical around zero.

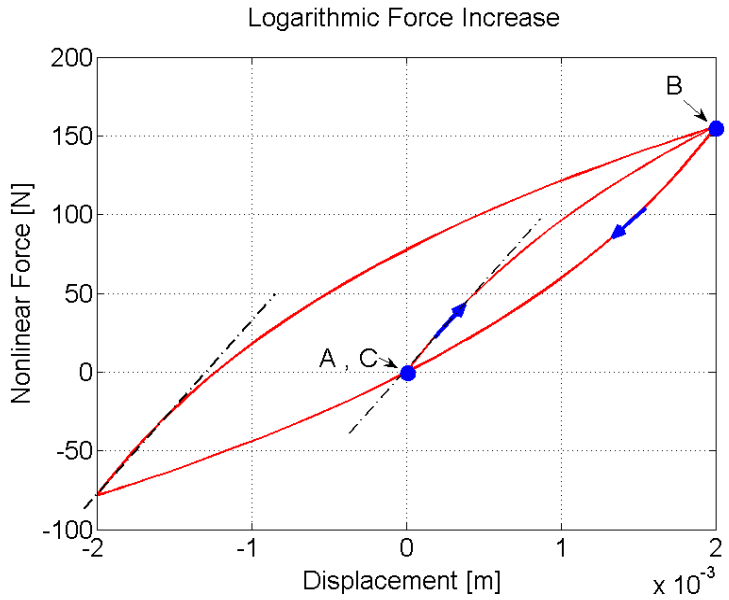

Figure 3-3: Logarithmic increase of non-linear friction force at sinusoidal excitation: Starting stiffness after turning points of motions are equal.

The logarithmic increase of the friction force leads to the desired behaviour during sinusoidal excitation, with increased damping and decreased stiffness being caused by an increase in amplitude.

3.1.4 Model Behaviour when Subject to a Sinusoidal Input

The following *Figure 4-5* presents measurement data with frequency (left) and with amplitude (right) for a typical elastomer mount and compares simulation results. The static stiffness remains constant around the measured amplitude range; amplitude dependence is only due to the Payne effect. The few user inputs to derive the model internal parameters are highlighted.

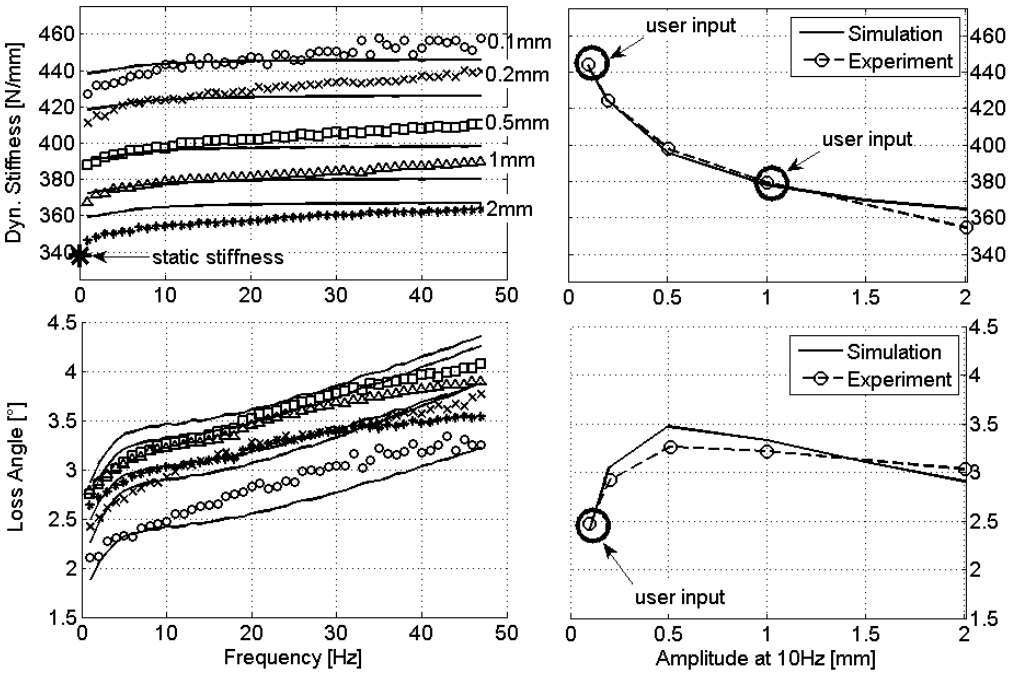

Figure 3-4: Measurement data and simulation results at sinusoidal excitation over frequency (left) and amplitude at 10 Hz (right). User inputs for model parameter estimation are marked.

Figure 3-4 shows the advantage of the non-linear model. It aligns well with the measurement data for a wide amplitude range from only few input parameters. The stiffness characteristics with amplitude are very accurately mapped in between the user inputs and the loss angle calculation is accurate enough to foresee the slope of damping with amplitude from only one required user input.

The linear model part for frequency dependence is able to map the increased damping with frequency and gives very accurate results for stiffness around the reference frequency 10 Hz. The non-linear force gives additional dynamic hardening and leads to a decreasing stiffness with amplitude; it automatically leads to the correct trend for loss angle with amplitude. Each direction needs the following input data, listed in *Table 3-1*.

Table 3-1 Main user inputs for parameter identification of new non-linear bushing model.

Parameter:	**Abbrev.**	**Symbol**	**Value:**
Static stiffness	*kstat*	k_{stat}	338 e³ N/m
Dynamic hardening 1	*DH1*	DH_1	444/338 =1.314
@ Smaller amplitude 1	*SA1*	$\hat{s}_1$	0.1e^{-3} m
Dynamic hardening 2	*DH2*	DH_2	380/338=1.124
@ Higher amplitude 2	*SA2*	$\hat{s}_2$	1.0e^{-3} m
Loss angle	*delta*	δ_1	2.47°@0.1 mm
Reference frequency	*FREQ*	f_0	10 Hz

A program internally calculates the model internal parameters from user inputs (or measurement data) within a few seconds, from the equations given in the frequency domain. The following scheme qualitatively describes this process. The details of initialisation values, boundaries for tolerances and internal sequence of calculation is crucial for accuracy but will not be further discussed herein. The entire calculations are based on the known equations, so that the iteration process takes only a few seconds (for elastomer mounts).

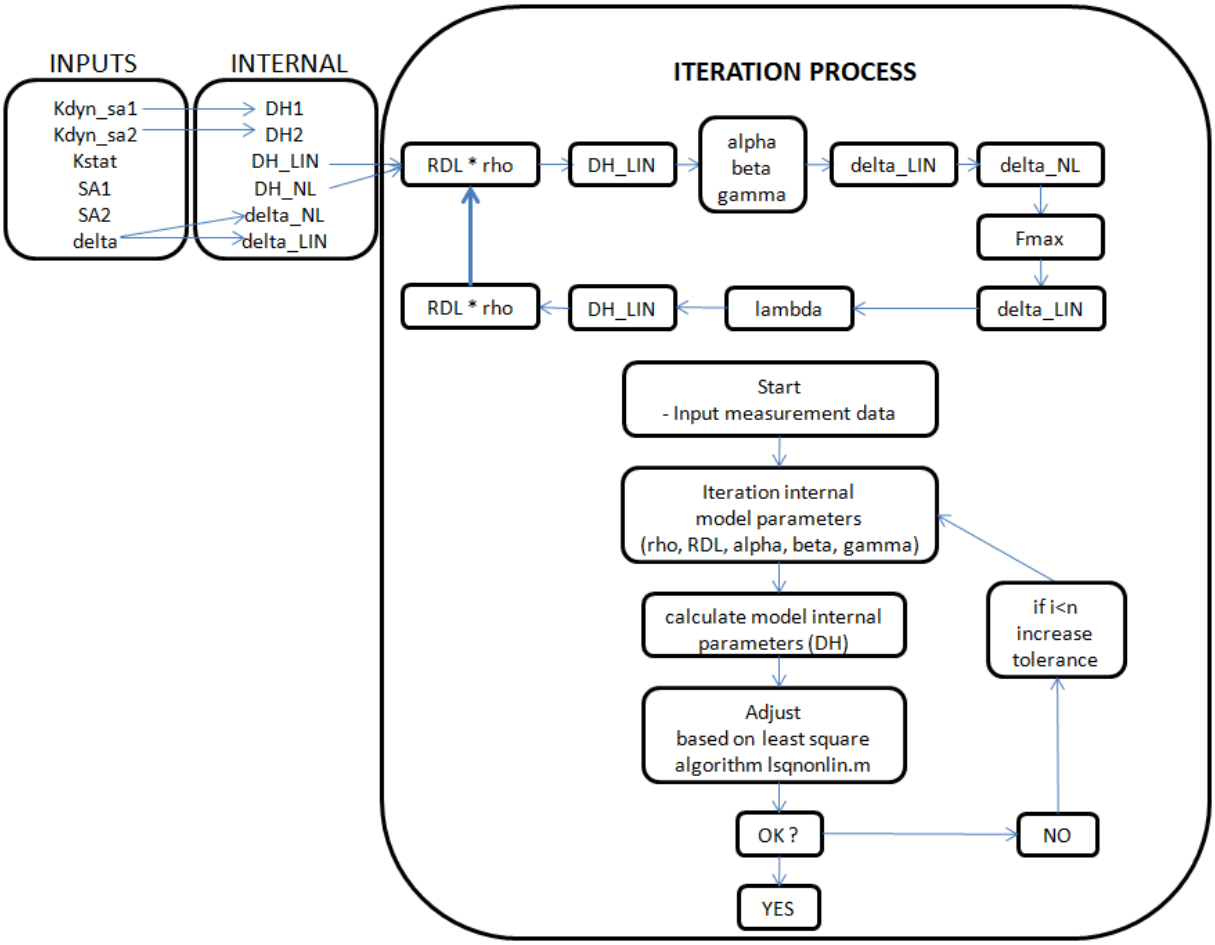

Figure 3-5: Process sequence sheme for parameter estimation and parameter iteration elastomer model

In the final model implementation the linear and non-linear parts are scaled via the static stiffness k_{stat}. Therefore the units for *RDL* changes from to Newtons to metres and the unit for λ from dimensionless to m/N. This note is relevant for reviewing parameter files. The following *Table 3-2* provides model internal parameters that are derived during this parameter estimation. Paper A briefly decribes parameter identification with the developed user tools.

Table 3-2 Model internal parameters for example bush.

Parameter:	Symbol	Value:	Unit
static stiffness	k_{stat}	338	N/m
alpha	α	0.1014	-
beta	β	0.0963	-
gamma	γ	0.0035	s
lamda	λ	0.3783	m/N
RDL	*RDL*	9.263E-05	m
rho	ρ	4352.2	1/m

3.1.5 Essential Improvements for Implementation

Model accuracy under sinusoidal excitation is not enough to validate non-linear model approaches. For instance, (*Mitsch et al. 2010)* highlight the effect of tolerances for bushes in serial production and concluded that more detailed models for the components do not automatically lead to more trustworthy simulation forecasts for the full-vehicle.

Experimental frequency response measurements during sinusoidal excitation indicate that non-linear modelling techniques are needed to better fit the behaviour of non-linear parts like elastomers or hydro bushes. However, some users state that such models give merely an improvement in full-vehicle simulation or are even less accurate than a simple spring-damper approach under superimposed or transient excitations. Publications that further clarify the modelling issues are rare but the ride comfort studies discussed in Chapter 4 revealed certain issues with this early model approach:

- Numerical instabilities and increased computing time when solvers with variable integration time steps are used
- Indifferent start-up behaviour with high oscillations until the whole system reaches a steady state
- Unexpected force drift phenomenon

If the model as described so far is used, a force or displacement drift may occur due to the nature of the model. Therefore this preliminary early model is developed further in the thesis. Pfeffer and Hofer (2002) and Pfeffer (2010), refer to this stage of development (Pfeffer model Generation 2 (G2) with property file format *.pfe).

Drift Phenomenon

The following Figure 3-6 presents experimental data and a simulation of the example bushing. The simulated force gradually moves out of the zero position and at the end of simulation an

offset to measurement can be observed; the error increases with the time period. Likewise, the amount of drift is affected by the type and length of the input signal, internal model parameterisation, solver settings and integration times and the numerical details of virtual test rig.

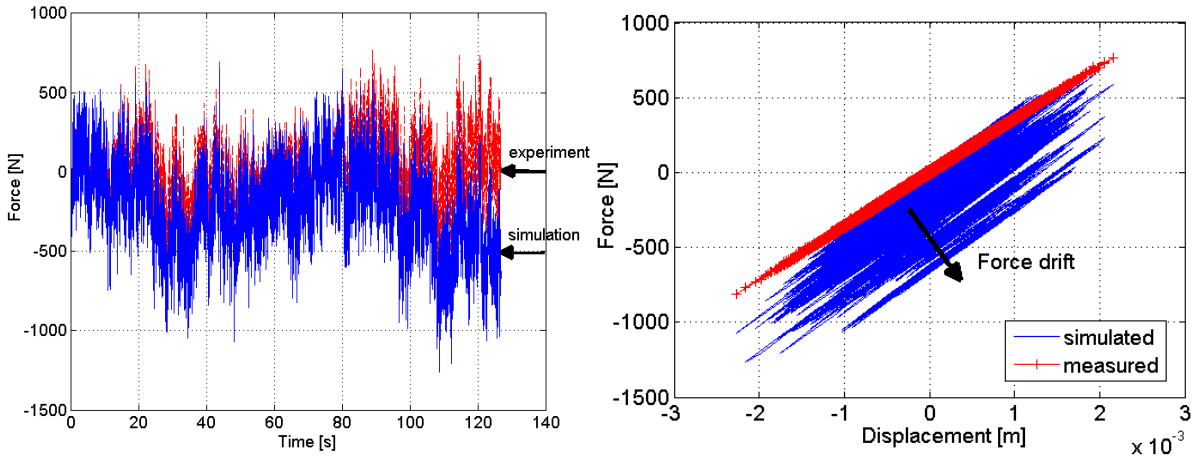

Figure 3-6: Force drift at random input signal for non-linear model without relaxation or limitation of the non-linear friction force

To evaluate the bushes, random input signals have been created, where the min/max and average amplitudes over frequency are similar to on-road-test manoeuvres. The signal's power spectral density—its energy per frequency interval—is inversely proportional to the frequency of the signal, so that higher amplitudes occur at smaller frequency. This excitation signal triggered the drift behaviour well and was used for model development and to check the parameter settings against this phenomenon. Several approaches from literature have been tested and similar behaviour was observed. In the following section, essential changes for successful implementation into the MBS environment are discussed and certain details are mentioned that are not described in the main journal articles presented in this thesis.

Start-Up Behaviour

On initial start-up of the model, the friction force depends on the force preload or the corresponding displacement offset. The hysteresis loops do not centre around zero and are not symmetric and, therefore, the force level and the stiffness of the first half cycle highly depends on the initial preload/displacement at start of the simulation as shown in Figure 3-7.

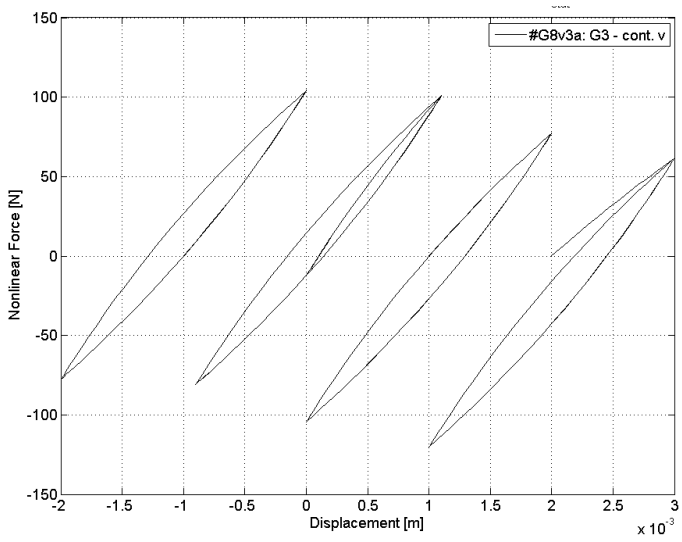

Figure 3-7: Non-linear Force of Pfeffer model without relaxation or force limit under varying preload conditions; RDL=9.1e-5 rho=410; kstat=330N/mm.

The force calculation associated with the displacement also has the drawback that, due to its non-linear nature, it can be very high on initial start-up. This high start value may lead to a force overshoot at the start of the simulation until the overall system has reached a steady state around its operating range, with deflection depending on the mass on the mount.

To avoid this phenomenon, it is beneficial to calculate the non-linear force from the integral of stiffness over time, so that it starts around zero in all circumstances:

General rules for integral calculus where *a* and *b* are parameters, *x* is the integration variable and *C* is an integration constant:

$$\int \frac{1}{ax+b}\,dx = \frac{1}{a}\cdot\log|ax+b| + C \tag{3-6}$$

$$f(x) = a\cdot\log(1+b|x|)$$
$$f'(x) = \frac{a\cdot b}{b|x|+1} \tag{3-7}$$

Applied to the non-linear Force F_{NL}:

$$F_{NL} = RDL\log(\rho\cdot|\Delta u|+1) \tag{3-8}$$

$$f'(u) = \frac{dF_{NL}}{du} = \frac{RDL\cdot\rho}{(\rho\cdot|\Delta u|+1)} \tag{3-9}$$

The equation can be rearranged in a way that the integral with displacement is multiplied with the velocity to substitute dF_{NL}/dt:

$$\frac{dF_{NL}}{dt} = \frac{dF_{NL}}{du} \cdot \frac{du}{dt} = \frac{RDL \cdot \rho}{(1 + \rho \cdot |\Delta u|)} \cdot \dot{u} \tag{3-10}$$

$$F_{NL} = \int \frac{dF_{NL}}{dt} dt = \int \left(\frac{RDL \cdot \rho}{(1 + \rho \cdot |\Delta u|)} \cdot \dot{u} \right) dt \tag{3-11}$$

In order to eliminate the impact of an existing displacement offset x_Q on the non-linear force, the integral of velocity is used instead of the actual overall displacement x for the input u itself. Hence, the only remaining input for the non-linear model part is velocity $\dot{x}(t)$.

$$x = u + x_Q \tag{3-12}$$

$$u = \int_{t=o}^{t} \dot{x} \cdot dt \tag{3-13}$$

$$\Delta u(t) = u(t) - u_{TP} = \int_{t_{TP}}^{t} \dot{x} \cdot dt \tag{3-14}$$

The above modifications improved the initial start-up behaviour and decreased the calculation time, improving the simulation performance when variable step size solvers were used; but the model still showed the drift phenomenon. Scheiblegger et. al. (2011), Büchler (2011) and chapter 4 refer to this stage of model development (Pfeffer Model Generation 3 G3, file format *.ubu). For parameter identification Matlab and Simulink programs were developed with separate programs and graphical user interfaces for elastomer mounts, hydro mounts, a virtual test rig and the import/export of parameter files.

Force Limit

Using the logarithmic friction force, the behaviour during sinusoidal excitation is mapped very well. However, in reality, experimental measurements indicate that additional relaxation can be observed where the material's internal stress is reduced over time. If this relaxation is not taken into account, unwanted model behaviour may occur at superimposed, transient or random excitation.

It is difficult to find good model parameters for relaxation over time for all possible test procedures because preloading, frequency, amplitude and the resulting non-linear friction forces cannot be foreseen. If the non-linear force decreases over time, due to relaxation, the frequency dependent and amplitude dependent properties of the model would be linked together, making parameter identification and prediction of the model behaviour far more difficult.

In order to overcome the modelling difficulties associated with relaxation over time, an additional limitation of the friction force was introduced. Here, the friction force does not disappear over time but is limited to a set value and thereby forced to centre around zero in any case. Model performance under transient or superimposed excitation improves significantly.

Because the overall model force is scaled with static stiffness, the signal y_{NL} here can be referred to as non-linear displacement–or relative friction force.

$$F_{NL} = k_{stat} \cdot y_{NL} \tag{3-15}$$

A force limiting scaling function y_{scale} is introduced, that refers to the last value of relative friction force $y_{NL\,i-1}$.

$$y_{NL} = \int \frac{RDL \cdot \rho}{\rho \cdot |u - u_{TP}| + 1} \cdot y_{scale} \cdot \dot{u} \cdot dt \tag{3-16}$$

$$y_{scale} = \begin{pmatrix} \dfrac{y_{\max} + y_{NLi-1}}{y_{\max}} & \dot{u} > 0 \\ \dfrac{y_{\max} - y_{NLi-1}}{y_{\max}} & \dot{u} < 0 \end{pmatrix} \tag{3-17}$$

$$y_{scale} = \frac{y_{\max} \pm y_{NLi-1}}{y_{\max}} \tag{3-18}$$

To differentiate cases for the sign of velocity, a hyperbolic tangent function is used with gradient parameter k_{Sign}:

$$x_{Sign} = \tanh(\dot{u} \cdot k_{Sign}) \tag{3-19}$$

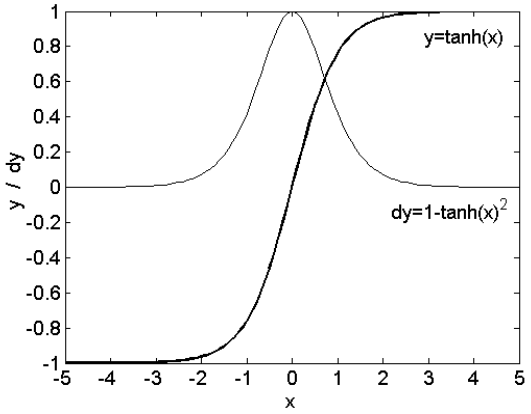

Figure 3-8: Hyperbolic tangent function and its derivative to replace discontinuous sign-function.

The function leads to positive or negative sign, but with a continuous change of slope, its derivative is also continuous. $k_{Sign} = 1e^9$ for input units in metres or k_{Sign}=0 to deactivate the scaling function. The standard unit representation in Adams is metres, but the user can chose input in mm, alternatively. The gradient k_{Sign} smooths the whole function for numerical stability and the value of k_{Sign} can be changed for different units.

x_{Sign} now substitutes the velocity within the function to calculate the non-linear force.

$$y_{scale} = \frac{y_{\max} + y_{NLi-1} \cdot x_{sign}}{y_{\max}} \tag{3-20}$$

The model internal parameter for y_{max} is called F_{max1} but it refers to a relative force, or non-linear displacement due to the model scaling via the static stiffness k_{stat}.

$$F_{\max} = y_{\max} \cdot k_{stat} \quad [\mathrm{N}] \tag{3-21}$$

$$F_{max1} = F_{max\_rel} = y_{\max} \quad [\mathrm{m}] \tag{3-22}$$

y_{max} is scaled with static stiffness and can be taken from the measured hysteresis width HW at quasi-static excitation.

$$y_{max} = HW_{rel} = F_{hys}/k_{stat} \quad [\mathrm{m}] \tag{3-23}$$

The Simulink representation of the non-linear module is shown in Figure 3-9.

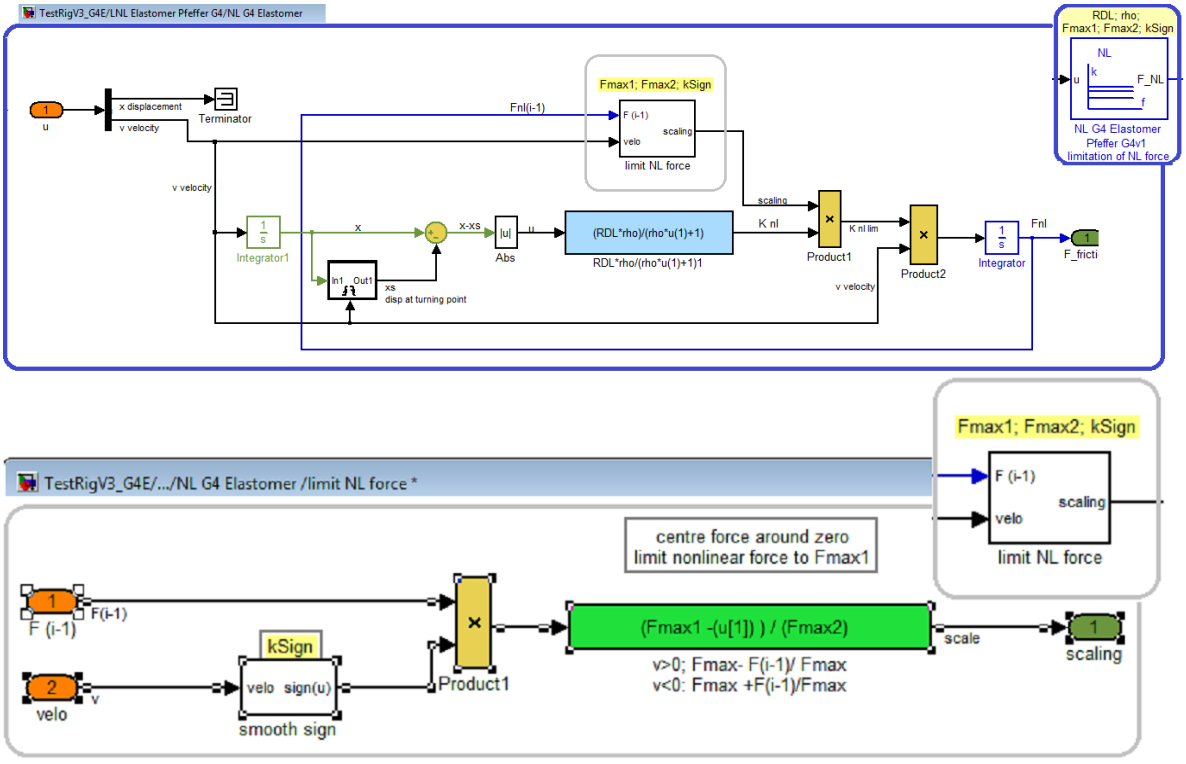

Figure 3-9: Simulink representation of non-linear module (top) and force limiting function (bottom).

Figure 3-10 shows force characteristics of the complete non-linear module where the additional force limitation overrules the purely logarithmic force increase. The stiffness of the first half cycle (A-B) is equal to the average stiffness for the entire loop (B-C). The start-up stiffness directly after the following reversal point (C–D) is defined by $RDL \cdot \rho$ and is significantly higher than the average stiffness (C-D).

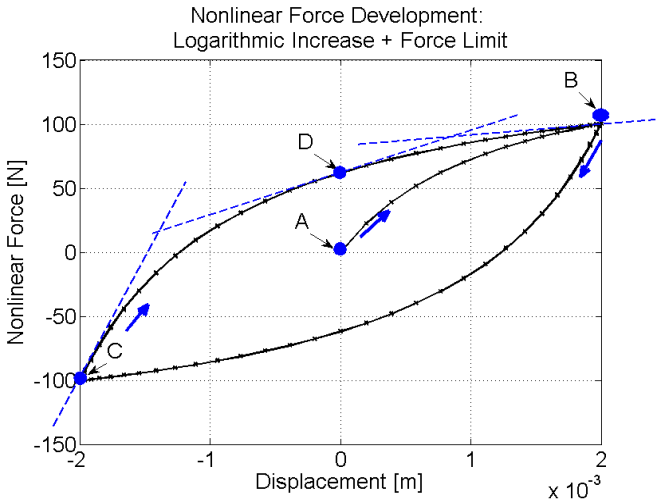

Figure 3-10: Non-linear friction force with limit F_{max}=150 N at sinusoidal excitation: force centers around zero and startup behaviour is different from purely logarithmic approach.

It is important to note that the friction force is now symmetric around zero whereas the purely logarithmic approach is not. The resulting force-displacement loops of the entire model are very similar to real measurements.

3.1.6 Model Validation - Drift Phenomenon

Figure 3-11 (left) compares measurement with simulation for the new approach with an additional force limitation 150 N. Simulation and experimental data are well matched. The right-hand graph shows the non-linear force and proves that the drift phenomenon is effectively eliminated if F_{max} is chosen in a reasonable way; e.g. from hysteresis width at static measurement (a). Curve (b) shows severe drift of the non-linear force when a purely logarithmic approach (without force limit) is used.

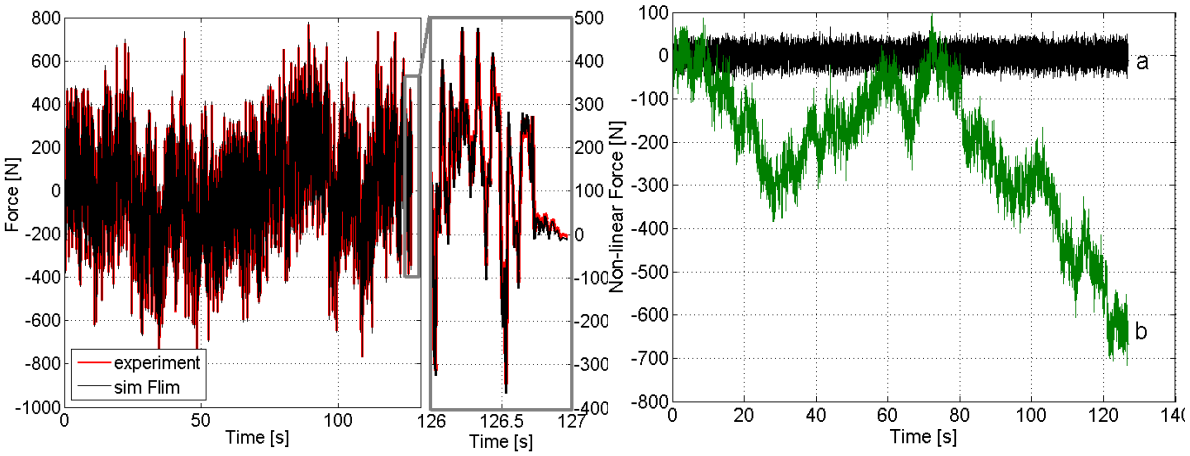

Figure 3-11: Experiment and simulation for long time signal and details thereof (left). Right graph: evaluation against drift phenomenon for model including force limit (black curve a) and without force limit (green curve b).

In Papers A, B and D several long-time transient signals are used to further validate the model for more mounts and bushes.

Figure 3-12 provides the result of parameter estimation for the model without force limitation (left) and for maximum friction force 150 N that was derived from the static hysteresis. As can be seen, the overall behaviour is largely unaffected by the force limitation and only the underlying loss angle contribution of the linear element of the model (broken line) is reduced.

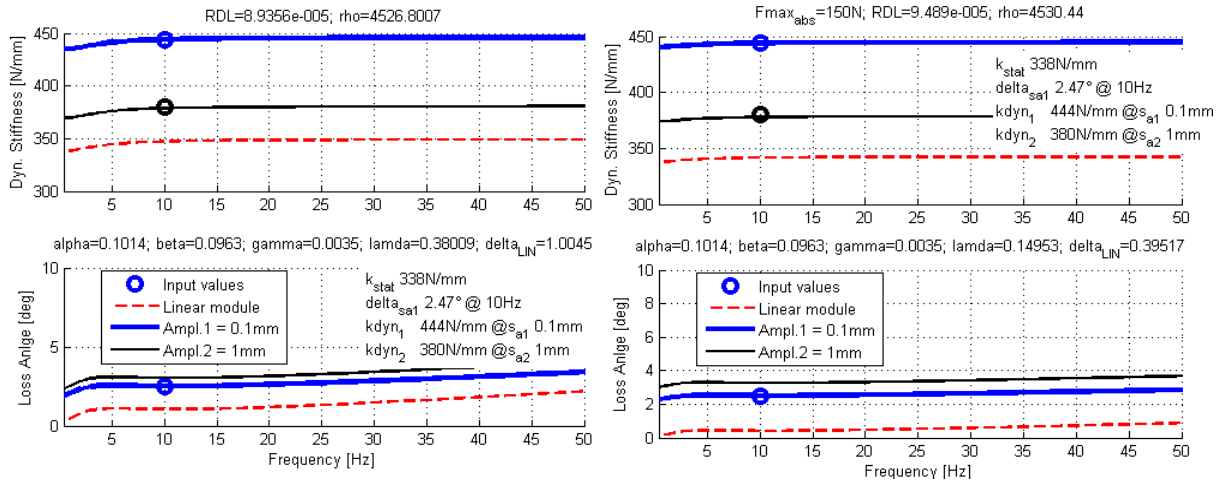

Figure 3-12: Results of model initialisation without force limit (left) and with maximum friction force 150N (right).

The following *Table 3-3* provides the model internal parameters with and without the force limit. Paper A briefly describes parameter identification with the newly developed user tools.

Table 3-3 Model internal parameters for example bush.

		Incl. force limit	**Logarithmic**	
Parameter:	**Symbol**	**Value:**	**Value:**	**Unit**
Static stiffness	k_{stat}	338	338	N/m
alpha	α	0.1014	0.1014	-
beta	β	0.0963	0.0963	-
gamma	γ	0.0035	0.0035	s
lamda	λ	0.1495	0.3803	m/N
RDL	*RDL*	9.49E-05	8.93E-05	m
rho	ρ	4530.4	4528.2	1/m
Force Limit	*Fmax*	150	-	N
string input for force limit	*strFmax*	150/kstat	-	m
Force limit rel	*Fmax1*	0.0004438	-	m
Signum function gradient	*kSign*	1e9	0	-

After the changes presented above, the overall model was able to satisfy requirements for a practical implementation. Compared with other models presented in the literature review and from the start of this investigation, the computing time, accuracy, numerical stability and behaviour during transients and long-term signals were significantly improved.

3.2 Hydro Mount Model

Many models for hydro mounts have been developed and published in the literature (*Barker (2004), Fan and Lu (2007), Lee and Kim (2005), Lee and Singh (2008), Kramarczuk (2012), Weber (1998), Whear and Williams (2005)*). However, most neglect the amplitude dependent properties associated with the underlying rubber parts. Having developed and validated the elastomer modelling approach described above, this elastomer modelling approach was then incorporated into a more complex hydro mount model, to represent its rubber parts. Additional model parts were developed to take into account the decoupling functionality of fully or partially decoupled HEM and better match the behaviour of hydro suspension bushes.

In the following, the model structure and details for the decoupler functionality are briefly described. Simulation results are validated in chapter 6, in the context of a ride comfort simulation for a passenger car. A more detailed description and parameter study is given in paper B (chapter 6, page 76). In this paper the model is used for durability load analyses of a pick-up truck – with significantly higher excitations than at the ride comfort study.

Paper C discusses a model for active hydro engine mounts. Here the amplitude dependence of its underlying rubber parts has been neglected, because the frequency range of interest is much higher (up to 400 Hz) and small amplitudes are crucial.

3.2.1 Model Structure

The presented model is of a modular structure as shown in Figure 3-13, where the hydro mount behaviour is a superposition of:

- *Elastomer behaviour* of its underlying rubber parts where c_T represents the main rubber stiffness (in the vertical direction). The chamber stiffness c_B represents the resistance against puffing of the chamber (chamber compliance, volumetric stiffness). Both springs for the main rubber c_T and chamber rubber c_B are calculated from a sub-model for the elastomer that takes into account amplitude dependence due to the Payne effects. c_T and c_B are to be regarded as complex stiffness and depend on the current preload, frequency and amplitude.

- *Tuned mass damping effect* is affected by the chamber compliance c_B, the main rubber stiffness c_T and the fluid mass m_K as the main factors of impact. The pulsation in the

fluid channel is amplified as a result of the 'hydraulic lever arm', where the areas of the main spring A_0, the chamber A_B and the fluid channel area A_K are relevant.

- Additional *fluid damping* in the channel and at the orifice at input and output. The virtual fluid mass m_K is known from the channel length l_K, the channel area A_K and the fluid density ρ_F.

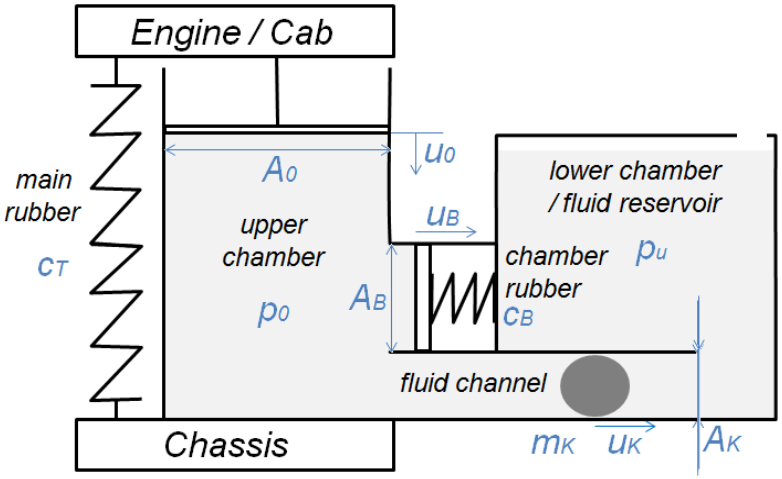

- *Figure 3-13: Simple hydro mount model for principal investigations.*[1]

The overall force on the top of the hydro mount is calculated as:

$$F = c_T \cdot u_0 + p_0 \cdot A_B \tag{3-24}$$

The pressure p_0 in the upper chamber increases due to the force F. The chamber displacement (deflection) u_B results from the pressure in the upper chamber p_o.

$$p_0 \cdot A_B = u_B \cdot c_B \tag{3-25}$$

The fluid (mass m_K and displacement u_K) flows through the channel with length l_K and cross sectional area A_K. d and β are damping coefficients for linear and non-linear fluid damping in the channel, respectively.

$$m_K \cdot \ddot{u}_K = p_0 \cdot A_K - d \cdot \dot{u}_K - d \cdot \beta \cdot \dot{u}_K^{\,2} \cdot sign(\dot{u}_K) \tag{3-26}$$

In simple passive engine mounts, the lower chamber consists of a flexible rubber diaphragm membrane and acts as a fluid reservoir with atmospheric pressure p_u=0. Even if the lower chamber is physically closed and under pressure, the assumption p_u=0 still gives a good agreement to experimental data. For further simplification, it is assumed that the main rubber area is the same as the chamber area.

1 Because earlier model versions are still in use, the German notation for springs has been kept with cT for the dynamic stiffness of main rubber (top mount/Tragfeder) and cB of chamber rubber (bulge stiffness/Blähfeder).

$$A_0 \approx A_B \tag{3-27}$$

In order to understand the physical correlations, it is important to be aware that a change of input displacement at slow excitation does not affect the pressure p_0 inside the mount. At slow excitation, fluid flows freely through the channel without damping. Therefore, an input displacement u_0 only contributes to the calculation of F_T due to the rubber spring c_T. Deflection of u_B of the chamber is calculated from the integral of velocity du_0 over time; thereby eliminating a constant displacement offset Q_0 due to static gravitational load onto the mount.

$$u_B = \int \left(\dot{u}_0 - \dot{u}_K \frac{A_K}{A_B} \right) \tag{3-28}$$

It is assumed that the fluid is incompressible. So, pressure can be calculated as

$$p_0 = \frac{u_B \cdot c_B}{A_B} = \int \left(\dot{u}_0 - \dot{u}_K \frac{A_K}{A_B} \right) \cdot \frac{c_B}{A_B} \tag{3-29}$$

The challenge for a practical flexible hydro mount model is to be able to cope with a wide range of mounts and hydro bushes. During a ride comfort study the model was used for four differently tuned hydro engine mounts and hydro suspension bushes. Chapter 5 gives a brief validation. The hydro mount model and underlying phenomena are described in more detail in chapter 7 (*Paper B*). In the following, an approach for decoupled mounts is discussed because *Paper B* does not address this functionality.

3.2.2 Decoupler

An ideal mount should be soft at high frequencies to isolate vibrations. Because high frequency vibrations are of low magnitude (amplitude), some hydro mounts use a decoupling functionality that blocks the fluid channel off from the main chamber; a soft decoupling membrane with very low resistance moves if pressure increases, until a certain volume is reached. Only then, the fluid flows freely into the inertia track.

The decoupler is modelled by introducing a non-linear factor into the chamber stiffness. At small amplitude, the chamber compliance is low due to a soft rubber diaphragm. The overall resistance against a pressure increase (stiffness) is very low, so most of the fluid remains in the upper chamber. The diaphragm can only move to a certain deflection, or fluid volume.

The following equations are used to calculate the effective displacement of u_B that moves the chamber rubber, where u_2 is the input displacement, resulting from main rubber deflection.

$$u_B = u_2 - D_{decoupling} \cdot \tanh\left(\left(\frac{K_{decoupling}}{D_{decoupling}} \cdot u_2\right)^2\right) \tag{3-30}$$

$D_{decoupling}$ defines the displacement of the decoupler play and a stiffness coefficient $K_{decoupling}$ defines the smoothness of the function. *Figure 3-14* highlights a soft decoupling membrane and gives the resulting displacement characteristics within the chamber.

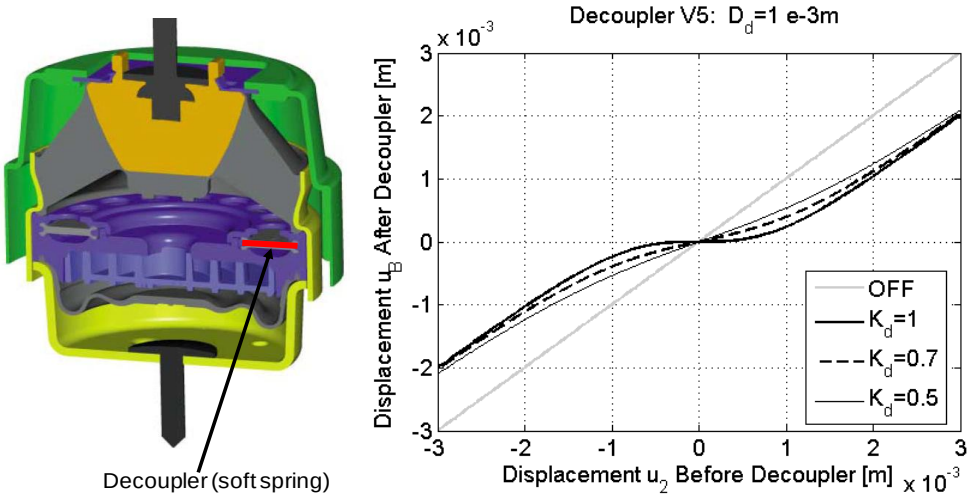

Figure 3-14: Cross-section of partially decoupled engine mount with soft decoupling diaphragm (left). Effect of decoupler for decoupled amplitude (play) $D_{decoupling}$=1 mm and varying decoupling stiffness $K_{decoupling}$

For small amplitudes, the movement is fully or partially absorbed by the decoupler or soft rubber diaphragm. For stable model implementation, the fluid velocity at the chamber du_B/dt needs to be given, to avoid derivatives inside the model. The chamber displacement u_B is then calculated from the integral of its velocity.

$$u_B = \int \dot{u}_B \cdot dt \tag{3-31}$$

$$\dot{u}_B = \left(1 - \left[1 - \tanh\left(\left(\frac{K_{decoupling}}{D_{decoupling}} \cdot \dot{u}_2\right)^2\right) \cdot K_{decoupling}\right]\right) \cdot \dot{u}_2 \tag{3-32}$$

Due to the play, the mean overall stiffness for the chamber rubber decreases. The following Figure 3-15 shows the average stiffness over amplitude for $D_{decoupling}$=1 mm. At small excitation, the overall stiffness c_B is much lower; for high amplitude 1 mm, the average stiffness is 90% of the underlying chamber rubber stiffness c_{B0}.

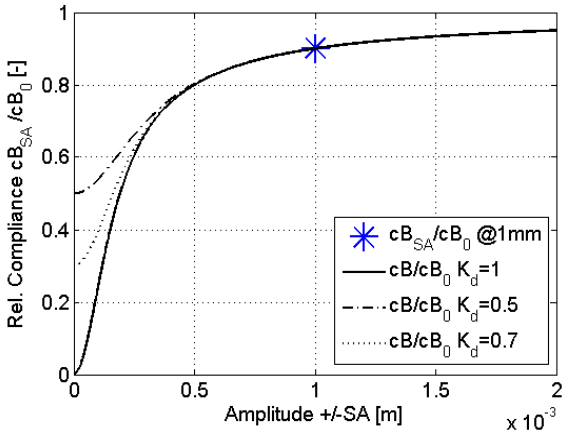

Figure 3-15: Effect of decoupling function onto the chamber compliance c_B for for $D_{decoupling}$=1 mm and varying $K_{decoupling}$

With the gradient $K_{decoupling}$, the resulting behaviour at deflections smaller than $D_{decoupling}$ can be tuned, allowing an appropriate fit for the operating range where the hydraulics are only partially decoupled.

- $D_{decoupling}$ defines at which amplitude the mount behaves as a simple passive mount.
- $K_{decoupling}$ is usually 1 but can be tuned for more accurate results in the area where the mount is only partly decoupled.

Using this formulation for decoupler functionality, the model aligns well with experimental data for partially or fully decoupled mounts over the entire amplitude range. The following Figure 3-16 shows parameter identification results for a fully decoupled hydro mount. In contrast to uncoupled hydro mounts, the resonance frequency and the point of maximum loss angle does increase when the amplitude increases.

At 0.06 mm and 0.1 mm amplitudes, the damping and stiffness are significantly lower than at higher amplitudes; and the maximum stiffness and maximum loss angle are reached at lower frequencies. For even smaller amplitudes and higher frequencies that are relevant for NVH, almost purely elastomeric behaviour can be observed -- where stiffness and loss angle increase only very slightly over frequency without a specific resonance peak.

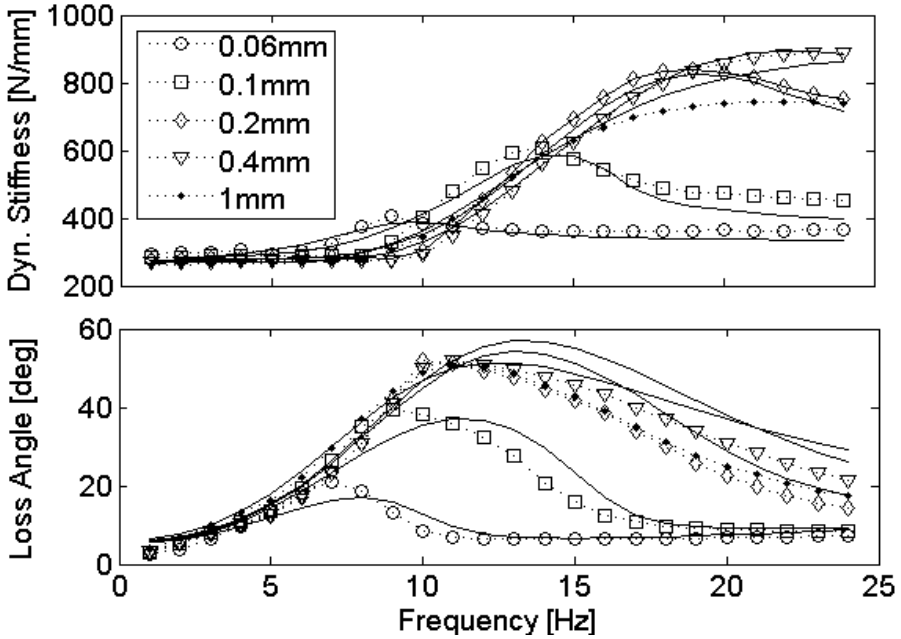

Figure 3-16: Model evaluation for fully decoupled hydro engine mount. Measurement (marker) and simulation (solid lines).

The presented hydro mount model gives very accurate results for this type of mount. In combination with amplitude dependent rubber parts and the decoupling stiffness gradient $K_{decoupling}$ the model is accurate enough for all types of passive hydro mounts.

For switchable HEM, the hydraulic damping can be entirely decoupled, e.g. at engine idle, to improve isolation for high-frequency vibrations with small amplitudes. The mount's stiffness then only depends on the underlying main rubber and is significantly lowered. For the simulation process, this traditionally means that two parameter sets have to be derived for:

a) elastomer behaviour for completely decoupled mode

b) normal hydro mount behaviour

In order to implement the above features, another property file had to be chosen, depending on the study. The model could not meet requirements if the damping is switched on or off during the simulation. To automatically generate the correct behaviour, the coefficient $K_{decoupling}$ has been implemented as the dynamic input for the simulation. For completely decoupled hydraulics, this signal is zero and otherwise it is 1. So, switchable mounts can effectively be simulated without loading a different property file to change model parameters.

In principal, the active hydro mount's (AEM) behaviour could also be studied with this model approach if $K_{decoupling}$ continuously changes its value and sign, but that was not the original intention of this work. In *Hausberg et al. (2015)* a separate model for AEM is presented, where the magnetic coil actuator dynamics have been studied and taken into account.

3.3 Summary of Presented Models

A model for elastomer bushes was presented, based on the approach suggested by *Pfeffer and Hofer (2002).* Such non-linear models may show unexpected behaviour under superimposed or long time domain signals. The drift phenomenon has been discussed and a new approach is presented that solves this issue by limiting the internal friction force. Furthermore, computing time and numerical stability for solvers with variable integration time step have been significantly improved before the implementation into an MBS environment.

The elastomer model approach is also used in the hydro mount model for the main rubber and chamber rubber and enables very accurate results. For hydro mount models, the challenge is to provide an approach that fits well for many different designs of mounts. An automatic parameter optimisation routine has been developed to tune unknown model parameters. The iteration process takes 10-20 min and leads to very accurate results for all types of passive mounts. A novel approach for the decoupler functionality has proved to generate very accurate results for partly decoupled mounts, so that the model is now able to cover all designs of passive hydro mounts and bushes.

Chapter 4 validates elastomer and hydro mounts in the context of ride-comfort of a full-vehicle simulation subject to low excitation amplitudes. Paper A discusses the elastomer mount more in detail for durability load analyses of a body-on-frame vehicle with higher loads. Paper B describes the hydro mount model and underlying phenomena more in detail. Paper C describes a model extension for active hydro mounts, where a simplified model for elastomer – without amplitude dependence – is incorporated.

Finally, paper D validates the overall model performance in full-vehicle simulation for durability load calculation and discusses other factors of importance for improved vehicle simulation.

4 MODEL EVALUATION: RIDE COMFORT STUDY

4.1 Area of Investigation

This section discusses the improvement of full-vehicle modelling for ride comfort simulation. For this principal investigation, the models have been manually parameterised first and then compiled into C-code to be implemented via General State Equation in Adams. Model parameters couldn't be changed afterwards. Model improvements, user tools for parameter identification, and the implementation into MBS environment with full functionality were subsequently developed.

Figure 4-1 highlights the position of suspension bushes. Overall, 9 different sorts of mounts are taken into account for this study: The rear frame is mounted with two differently tuned pairs of sub-frame bushes that may be conventional elastomeric bushes or hydro. Control-arm bushes are usually elastomeric type, but hydro suspension bushes (3) are alternatively used, to reduce vibrations during hard brake manoeuvres. The engine rests on two differently tuned hydro engine mounts and an elastomer gearbox mount; see also Figure 1-2 (page. 12). Top mounts are not considered here, but were modelled together within the system for the shock absorber.

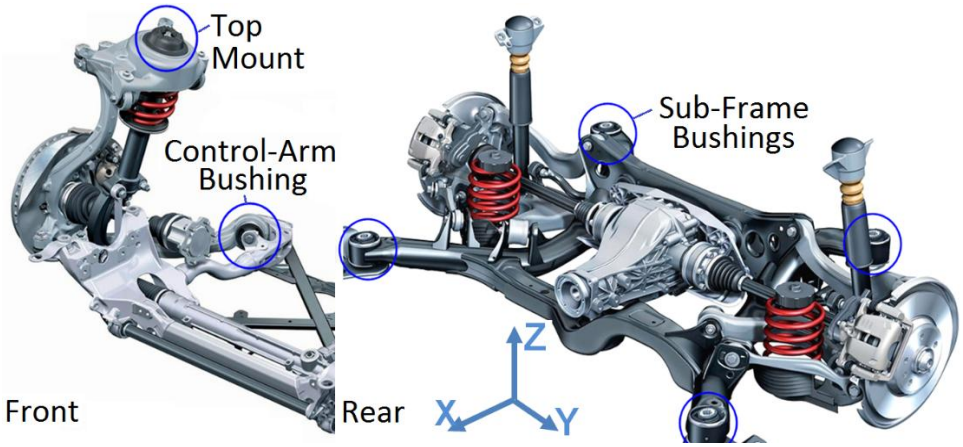

Figure 4-1: Position of the regarded mounts and bushes in passenger car. Control-arm bushing (elastomeric or hydro) and mounts for rear sub-frame in front(elastomer or hydro) and rear position (elastomer).

For each mount type, two alternative setups were separately tested on test rigs and various combinations were mounted in the vehicle to assess the influence on the comfort characteristics. Model parameters have been identified for 18 bushing elements in three translational directions, each.

Most directions are represented by the elastomer model; four differently tuned hydro engine mounts, one hydro control-arm bush and one hydro bush for the rear sub-frame represent

hydraulically damped directions. Several suspension versions have been tested, where the standard configuration (V00) uses only hydro engine mounts and rubber bushes for all other parts. An alternative setup V01 used a hydro steering-arm bushing and hydro bush for rear sub-frame (in the front position).

4.2 Elastomer Model Performance

Figure 4-3and Figure 4-3 give identification results of the elastomeric sub-frame bush in the longitudinal direction and the user inputs for static stiffness k_{stat}, dynamic hardening DH_1 at 0.1 mm and dynamic hardening DH_2 for higher amplitude 2 mm.

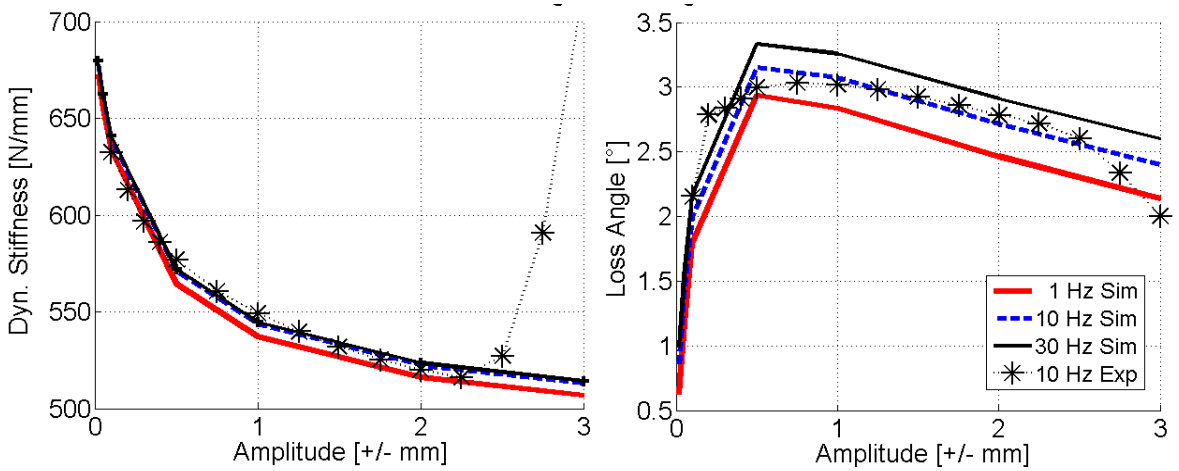

Figure 4-2: Model accuracy over amplitude for elastomeric sub-frame bush in longitudinal direction.

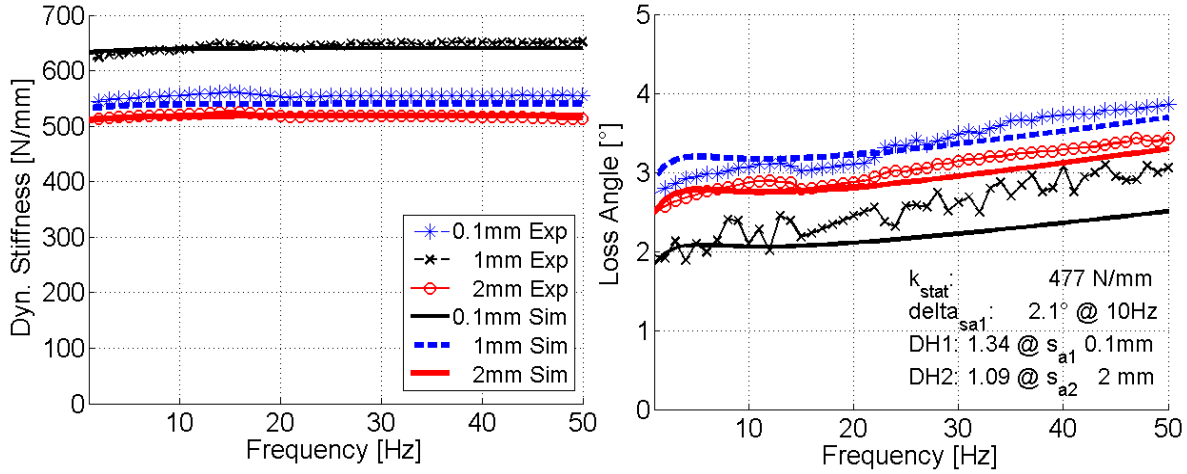

Figure 4-3: Model accuracy over frequency for elastomeric sub-frame bush in longitudinal direction.The simulation predictions for all other elastomer parts are qualitatively similar and the agreement between simulation and experiment is similarly good. The frequency and amplitude dependent behaviour of the elastomer bush is mapped very well giving benefit over the standard bushing element in MBS environment.

4.3 Hydro Mount Model Performance

Figure 4-4 shows simulation results for a simple hydro engine mount with a soft decoupler membrane. (Mount Type B Figure 2-5 on page 29).

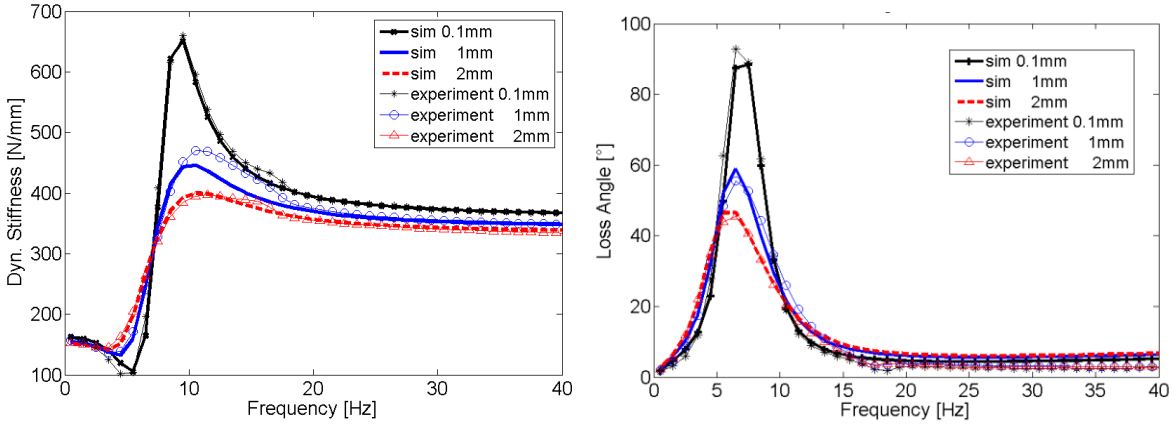

Figure 4-4: Model accuracy for hydro engine mount with soft decoupler membrane.

The dynamic stiffness and loss angle are mapped very accurately. Because the hysteresis loops in the resonance area may be very non-linear, it is not sufficient to judge the simulation accuracy on these results alone as they do not demonstrate the accurate capture of transient behaviour.

Figure 4-5 shows measured and simulated force displacement loops at 10Hz excitation for this mount. Simulation curves show the start-up behaviour whereas the mount has already reached a steady state during measurements. The shape of the hysteresis loop in the resonance area is very accurate for the presented model approach, so that the transient behaviour of the mount can also be confidently predicted.

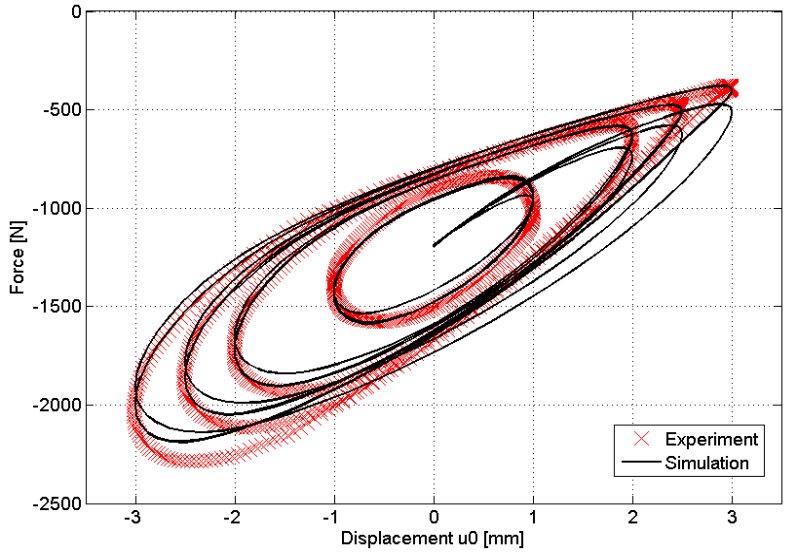

Figure 4-5: Hydro mount evaluation: at 10Hz highly non-linear hysteresis loops occur at a hydro engine mount with soft decoupler membrane.

4.4 Transient Excitation

After basic model evaluation under sinusoidal excitation, both types of mounts were tested on the component test rig with a transient input signal that qualitatively represents an on-road test manoeuvre for ride comfort. Both types of mounts align well on the component level as shown in the Figure 4-6.

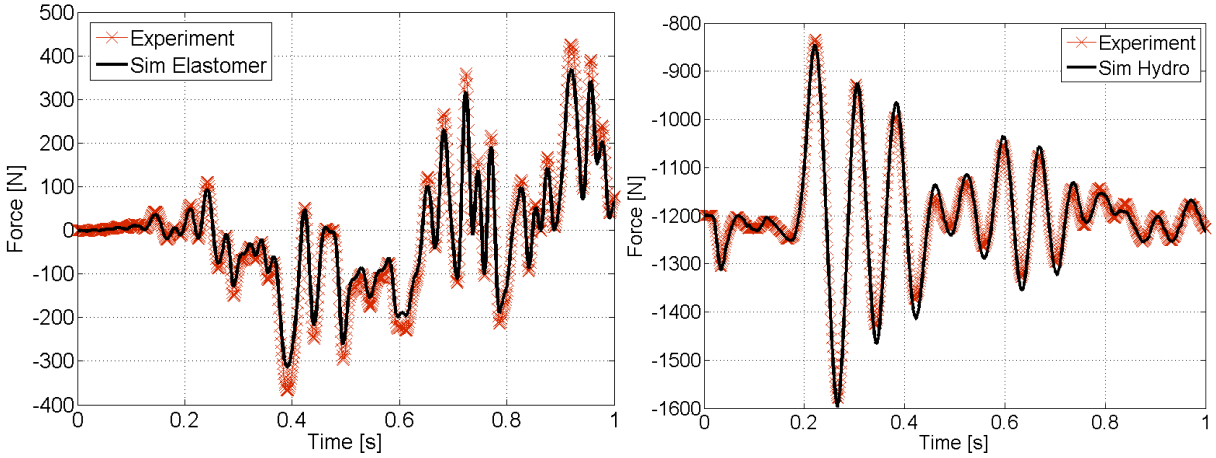

Figure 4-6: Model accuracy for elastomeric sub-frame bush and hydro mount under transient excitation.

4.5 Full Vehicle Simulation

Figure 4-7 shows the overall model performance of the full car model, for vertical acceleration at the driver seat, using a standard configuration for mounts and bushes (V00). Various on-road tests are marked with minimum and maximum range (curves 1). Firstly, the simulation has been carried out with Adams linear dual Kelvin-Voigt model (frequency bushing) where parameters had been tuned for 0.1 mm excitation amplitude (2). Non-linear static stiffness curves are taken into account via table data in all cases. The Adams hydro mount model (*Weber (1998), MSC Adams 2010*) has been used for the hydro engine mount. Compared with the linear models (2), accuracy improves for frequencies >25Hz if the new amplitude dependent models (3) are used.

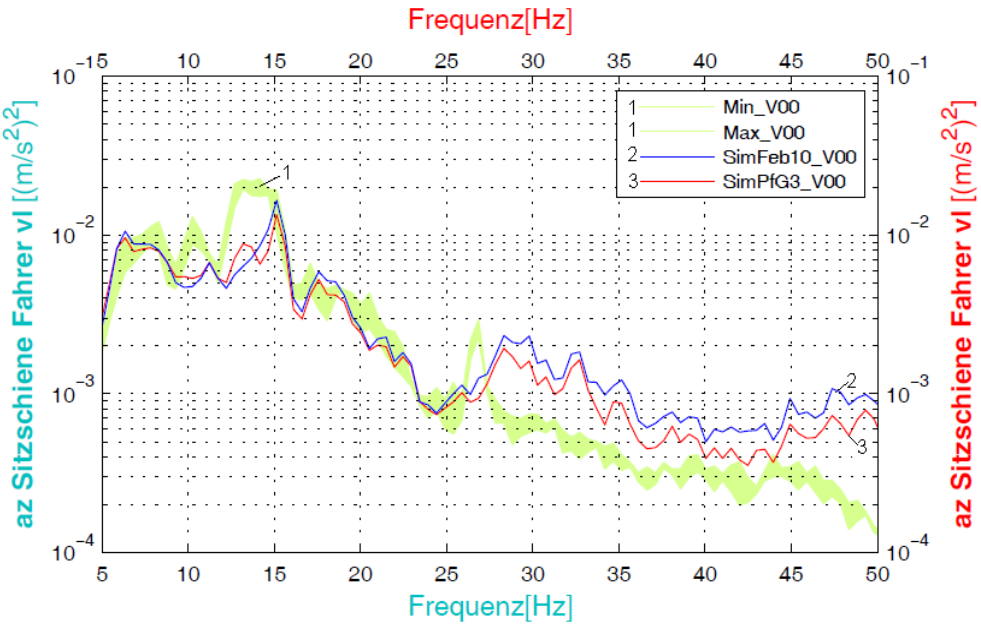

Figure 4-7: Acceleration at the driver seat in a vertical (z) direction during the test manoeuvre roll out west curve 120km/h: Experimental data with range of variation (1) and simulation results using Adams/ride frequency bushing models (2, SimFeb10_V00) and presented model w/o force limit (3, SimPfG3_V00); hydro model for engine mounts and elastomer models for all other mounts and bushes.

The results of the overall simulation with the new models are similar to those with the Frequency Bushing models because not all model features come into effect here. The displacement amplitudes and preloads during the conducted comfort manoeuvres had been rather small so that these functionalities affected simulation results less than, for instance, in studies for durability load analyses. The hydraulic engine mounts within this project are simple passive units with soft decoupling membranes. Therefore, the impact of improved modelling for decoupled mounts and hydro suspension bushes could not be assessed within this simulation.

For the car setup with hydraulic steering-arm bushes (V01), the simulation results with the new models (3) further improved for the longitudinal direction as shown in Figure 4-8. Here, the new model for hydro suspension bushes is able to slightly improve model performance of the full vehicle simulation.

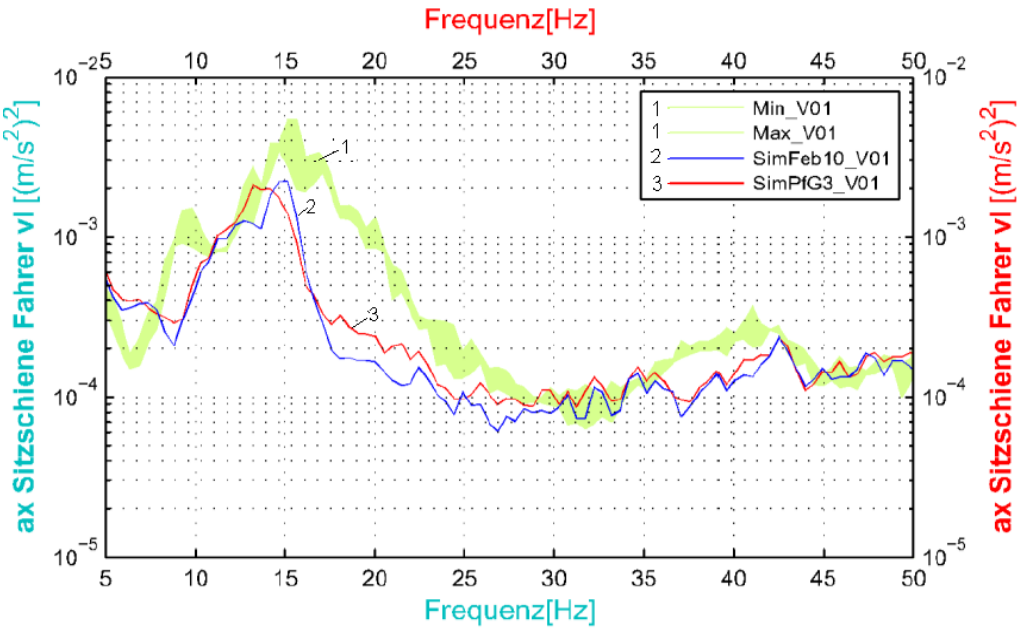

Figure 4-8: Acceleration at the driver seat in a longitudinal (x) direction during the test manoeuvre roll out west curve 120km/h: Experimental data with range of variation (1) and simulation results using Adams/ride frequency bushing models (2, SimFeb10_V00) and presented models w/o force limit (3, SimPfG3_V00); hydro model for engine mounts, separate model approach for the hydraulic steering arm bushes and elastomer models for all other mounts and bushes.

4.6 4-Poster Analysis Engine /Gearbox

The full vehicle simulation is affected by many parameters, such as flexible body structures, tyre models, accurate position and masses. The effect of the bushing models was relatively minor when compared with these influences. To isolate bushing model performance, a 4-poster analysis has been carried out, additionally.

Here, the measured excitations at the chassis were directly used as inputs for the simulation. Thus, tyre and damper models lose their influence on the simulation results. The engine rests on two differently tuned hydro engine mounts and the powertrain is additionally supported by an elastomeric gearbox mount. The vertical z-direction is hydraulically damped; longitudinal (x) and traverse direction (y) behave like conventional elastomer mounts.

Figure 4-9 shows the results for three different levels of detail for the mount model. Measurement data (1) is compared to simulation for spring-damper model (2) and linear frequency dependent bushing model (Dual Kelvin-Voigt) (3). Simulations with non-linear models that take into account amplitude dependence are given in (4).

The layout amplitude for the standard ADAMS bushing model (Kelvin-Voigt) was 1 mm (curve 2 in Figure 4-9); for the vertical z-direction of the engine mounts the ADAMS standard hydro mount model was used (2). With different parameterisation of the MBS model and usage of the ADAMS frequency dependent bushing model (based on dual Kelvin-Voigt),

performance was slightly improved for the z-direction (3). This model is a linear approach and does not take into account the amplitude dependence. The model parameters had been tuned for 0.1mm amplitude.

Finally, an amplitude dependent model for elastomer mounts and the new hydro mount model have been used (4). Thereby, the model performance was significantly improved. However, the full-car model still lacks accuracy in longitudinal direction x; the cause for this discrepancy could not be definitively clarified. These investigations were made in an early stage of development before the numerical implementation of the model had been improved to avoid drift phenomenon.

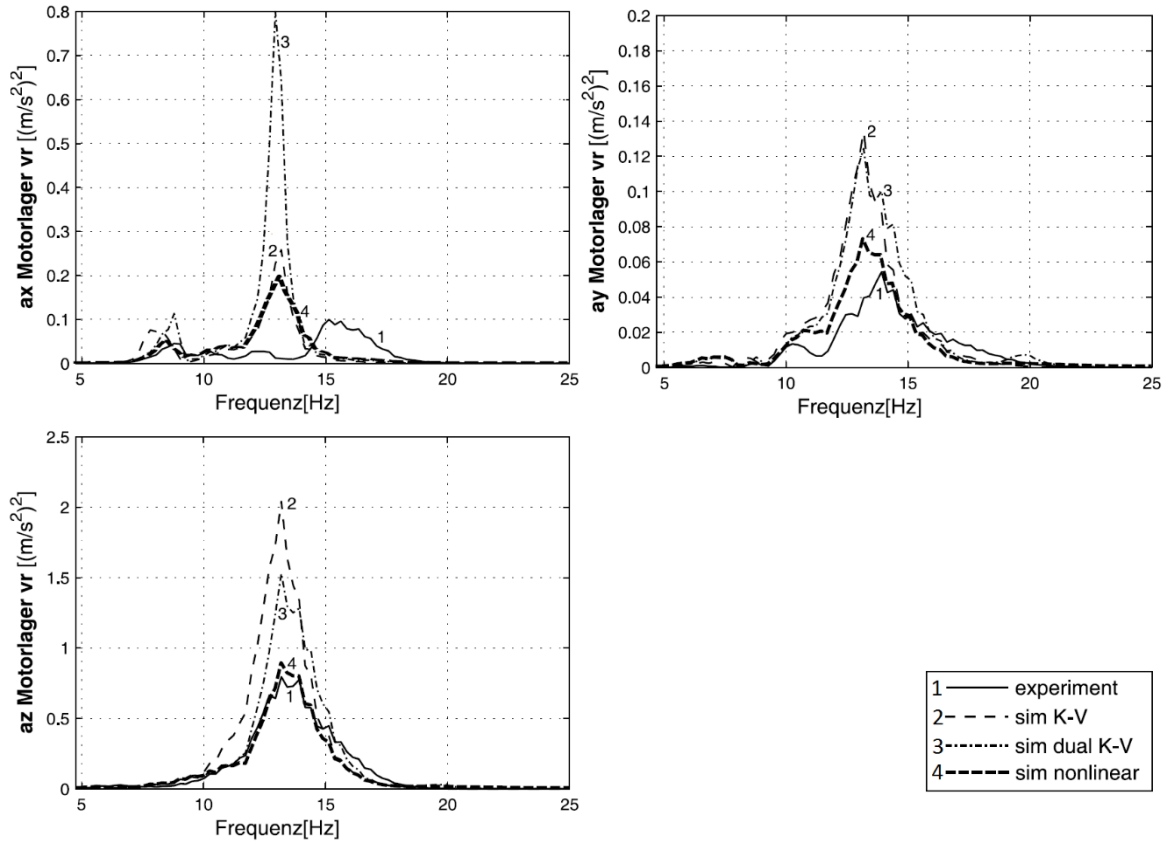

Figure 4-9: Potential to enhance overall vehicle simulation using non-linear modelling approaches: For simulation (2) the standard models in ADAMS were used: Kelvin-Voigt models for elastomer mounts (directions X and Y) and the standard hydro mount model for the Z direction. Simulation (3) was carried out with a different parameter set and elastomer models based on Dual Kelvin-Voigt (Adams frequency bushing). The use of non-linear models (4) for elastomer mounts and for hydro mounts in Z showed significant improvements. The X direction shows relevant discrepancies for all simulations, which might be caused by engine accessories or three-dimensional effects.

The full-vehicle simulations showed that different model approaches for mounts and bushes and their model parameterisation show relevant impact on model performance of the full-vehicle simulation. This analysis with 4-poster excitation clearly proved that the accuracy of models for mounts and bushes can be significantly improved using non-linear models that map amplitude dependence.

4.7 Conclusions from Ride Comfort Study

The previous chapters showed that the simulation results have significantly improved under sinusoidal excitation through improvements made in bush modelling. In this chapter, the models were firstly tested within full-vehicle simulation under MBS environment. Results under transient excitation were seen to improve, compared to simulation with simple spring-damper models; simulations are very accurate as long as the mounts and bushes are tested in isolation using the component test rigs. Overall results of the full vehicle simulation slightly improved in terms of accuracy compared to measured data, when the presented new bush models are used. In the full-vehicle model, there are many other sources of uncertainty that could not be clarified.

To reduce complexity for bushing model evaluation (compared to a full-vehicle simulation), a 4-poster analysis for the powertrain system eliminated the impact of tyre models and clearly showed potential for improvement when non-linear amplitude dependent models are used. Simulation forecasts are accurate for vertical and lateral directions but longitudinal direction is less accurate for unknown reasons.

Computing time of the overall vehicle slightly increased but is acceptable for the daily development process. The new mount model enables automatic linearisation of the bushing models without significantly increasing computing time. With the remaining Dual-Kelvin-Voigt approach for frequency dependence the simulation results significantly improved for all tested manoeuvres, compared to the simple spring-damper approach.

This study successfully assessed the principal improvements and justified further development for a practical model implementation into MBS environment. The early model version used for this chapter (without force limitation) showed certain numerical and principal drawbacks that were improved later on; for this principal investigation, model parameters could not be changed after code compiling. As a result of this study, usability and numerical stability of the model approaches and parameter identification tools have been further developed and successfully validated in long-term professional use within the development process of car manufacturers. (Büchler (2011), Pfeffer et al. (2014), MdynamiX (2017)).

5 ELASTOMER MOUNT MODEL

In this chapter the new non-linear model for elastomeric mounts and bushes is introduced and used for a study on durability loads of a body on frame light truck. Previous research on elastomer model within a ride comfort study on passenger cars (chapter 4) had dealt with lower excitation amplitudes and had only been published in German and within conference proceedings. The findings of the paper and study in this chapter now lead to the conclusion that the fully implemented models are capable to improve the simulation results significantly. Practicality and usability of the suggested model are validated within MBS software environment, for the daily development process in the early phase of vehicle development.

5.1 Paper A Non-Linear Modeling of Bushings and Cab Mounts for Calculation of Durability Loads

Scheiblegger, C., Roy, N., Silva Parez, O., Hillis, A. et al., "*Non-Linear Modeling of Bushings and Cab Mounts for Calculation of Durability Loads*," SAE Technical Paper 2014-01-0880. 2014, doi: 10.4271/2014-01-0880.

- **Focusses on Elastomer Mount Modelling**
- The author conducted most of the research. Design of experiments, data processing, model development, parameter identification and presentation of the results were his responsibility. Contribution approx. 90%.

5.2 Contribution to Research

This paper assesses the use of non-linear elastomer models for mounts and bushes to calculate durability loads in the context of full-vehicle simulation. The parameter identification process is discussed. The new non-linear bushing model is validated, regarding simulation accuracy, usability and computing time. Typical mount loads have been measured from durability events for model evaluation under realistic excitation. Within the context of this thesis, durability loads are much higher than during the ride comfort study, so that another area of use is validated.

In earlier research, similar modelling approaches have been presented from a research perspective but to be of practical use for industry, three major objectives were solved by the author:

a) Implementation into MBS with full functionality to import/export parameter files and defining directions, position and preloading of bushing elements in the full-vehicle simulation.

b) Unexpected behaviour, such as drift phenomenon had been revealed for non-linear models. The novel model approach to limit the friction force in order to improve model behaviour is mentioned for the first time.

c) User tools to derive model internal parameters from experiments and their validation for different mounts and directions.

The significance and originality of this article is that the practicality and usability of non-linear bushing models have been successfully validated under the harsh conditions of the automotive development process in an MBS environment. The novel model and tools for parameter identification were presented, tested and validated within a wider research context, in cooperation with external industry partners as users.

SAE INTERNATIONAL

Non-Linear Modeling of Bushings and Cab Mounts for Calculation of Durability Loads

2014-01-0880
Published 04/01/2014

Christian Scheiblegger
Munich University of Applied Sciences

Nantu Roy and Orlando Silva Parez
Chrysler Group LLC

Andrew Hillis
University of Bath

Peter Pfeffer
Munich University of Applied Sciences

Jos Darling
University of Bath

CITATION: Scheiblegger, C., Roy, N., Silva Parez, O., Hillis, A. et al., "Non-Linear Modeling of Bushings and Cab Mounts for Calculation of Durability Loads," SAE Technical Paper 2014-01-0880, 2014, doi:10.4271/2014-01-0880.

Abstract

Cab mounts and suspension bushings are crucial for ride and handling characteristics and must be durable under highly variable loading. Such elastomeric bushings exhibit non-linear behavior, depending on excitation frequency, amplitude and the level of preload. To calculate realistic loads for durability analysis of cars and trucks multi-body simulation (MBS) software is used, but standard bushing models for MBS neglect the amplitude dependent characteristics of elastomers and therefore lead to a trade-off in simulation accuracy. On the other hand, some non-linear model approaches lack an easy to use parameter identification process or need too much input data from experiments. Others exhibit severe drawbacks in computing time, accuracy or even numerical stability under realistic transient or superimposed sinusoidal excitation.

To improve bushing modeling of cab/box mounts for heavy duty/light duty trucks, a practical approach to model non-linear bushing dynamic characteristics has been tested and validated against standard bushing models. For model parameterization, several elastomeric cab mounts have been tested for their static and dynamic properties. The paper discusses the parameter identification process and validates the new non-linear bushing model regarding simulation accuracy, usability and computing time. Typical mount loads have been measured from durability events for model evaluation. This paper assesses the use of non-linear models for mounts and bushings to calculate durability loads in the context of full-vehicle simulation.

Introduction

For heavy duty and light duty trucks reliability and robustness are key requirements and therefore the accurate prediction of durability load is crucial during development process. Multi body simulation tools are used to simulate the impact of different stiffness and position of the mounts and bushings in the early phase of development. Prediction of road load using full-vehicle simulation is described in [1]. To improve accuracy of such analyses, the impact of cab mount models within the full vehicle simulation was assessed.

Elastomer mounts are widely used in automotive and railway applications [2]. For such parts highly non-linear behavior due to the Payne effect [3] is reported so that their properties significantly change over excitation amplitude. The mounts stiffness and damping characteristics are sensitive to the excitation amplitude and frequency as well as preload conditions. This non-linear behavior also affects hydraulically damped mounts due their underlying rubber parts.

In the standard development process, amplitude dependence due to the Payne effect is not considered within the MBS environment but simple spring-damper models are used for cab mounts, suspension bushings and jounce bumpers. Only

the non-linear static stiffness curves are implemented in standard MBS models. For this research, new non-linear bushing models were used for all cab mounts within the ADAMS/Car environment to assess the potential of improvement for full-vehicle simulation of durability loads.

Three different types of mounts are regarded, Figure 1 showing their position in the car frame. Overall, six mounts are modeled with the new non-linear model approach, with different characteristics in all three translational directions.

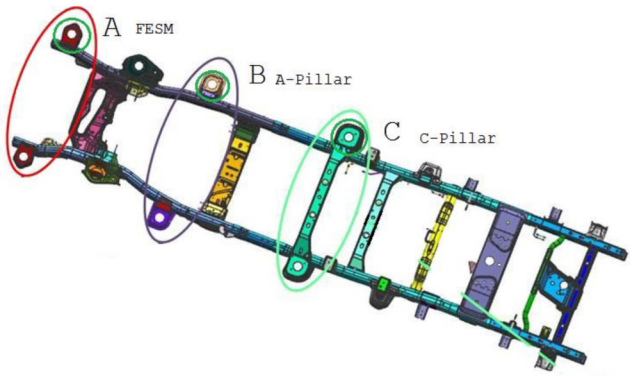

Figure 1. Virtual vehicle frame with position of regarded mounts and bushings marked.

For parameter identification the mounts have been tested under quasi-static and sinusoidal excitation. The models were then validated under realistic transient excitation derived from on-road experiments. Simulation accuracy and effort for parameter identification will be evaluated based on these experiments.

Characteristics of Elastomers

The term elastomer refers to any rubber parts including synthetic rubber compounds. Generally, elastomer parts' stiffness characteristics at quasi-static excitation are non-linear. Figure 2 shows the measured static stiffness curve for the cab mount type C and the table data for approximation within the model. The static stiffness k_{stat} depends on the loading conditions. Therefore, the following characteristics more or less depend on the preload and behavior varies at different operating points.

The material exhibits some damping which can be seen in the force-displacement hysteresis loops. Figure 3 shows force-displacement loops at 10Hz and highlights the average stiffness for amplitude 0.5mm. Such force-displacement loops are measured at sinusoidal excitation with increasing frequency for different amplitudes. The average dynamic stiffness is calculated as follows.

$$K_{dyn} = \frac{\Delta F}{\Delta s} \tag{1}$$

The area of the hysteresis loop A_{loss} represents the loss work:

$$A_{loss} = \oint F \cdot ds \tag{2}$$

The loss angle δ can be interpreted as the phase shift between force and displacement and is widely used to characterise the damping behaviour of mounts and bushings. It can be calculated from the integral of force over displacement, divided by a reference area:

$$\delta = \arcsin\left(\frac{A_{loss}}{\pi \cdot \Delta s/2 \cdot \Delta F/2}\right) \tag{3}$$

Damping and stiffness increase noticeably over frequency.

The dynamic stiffness under sinusoidal excitation is much higher than the static stiffness. Dynamic stiffness significantly decreases over excitation amplitude; known as the Payne effect.

After the end of excitation relaxation behaviour is observed for elastomeric parts. The materials internal stress gradually decreases over time.

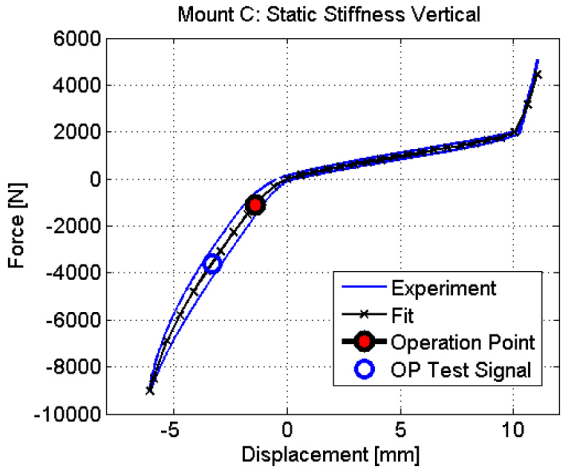

Figure 2. Measured non-linear static stiffness curve at slow excitation (10mm/min): Measurement; fit for main spring table data; standard operating point for parameter identification and preload during transient test signal

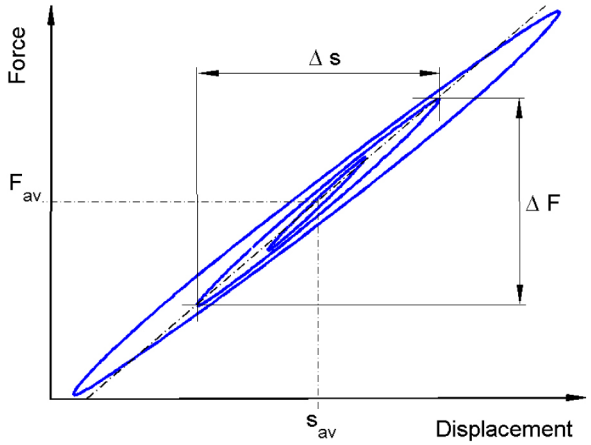

Figure 3. Measured hysteresis loops at sinusoidal excitation at 10Hz. The dynamic stiffness at small excitation amplitudes is higher than at high amplitudes, although the static stiffness remains constant.

Figure 4 presents measured dynamic stiffness and loss angle over frequency for one excitation amplitude and qualitatively shows simulation results using a standard linear spring-damper model (Kelvin-Voigt). The dynamic stiffness is accurately mapped over frequency but the damping characteristics are only a rough estimation. The loss angle increases linear over frequency, so that damping will be overestimated for higher frequencies. It is therefore important to know the layout frequency correctly. The model parameters for spring and dashpot elements can be chosen in a way to give a good fit around the specified layout frequency of main interest. Figure 4 illustrates the loss angle simulation for different model parameters to achieve a good fit around 5Hz, 10Hz, 15Hz or 20Hz. The main drawback of such standard spring-damper model is that the simulation results will be the same for any excitation amplitude whereas measurement data reveals strong amplitude dependence due to the Payne effect.

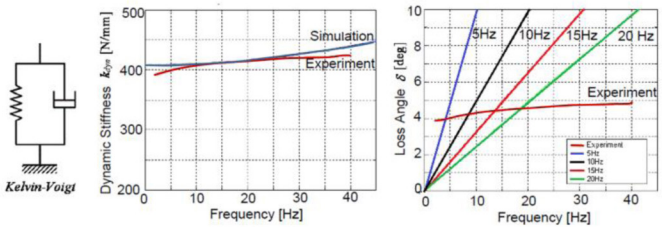

Figure 4. Evaluation of spring-damper model: Simulation results are shown for different layout frequency. Results are identical for any excitation amplitude.

Experimental data for a typical elastomer mount and simulation results with the proposed new non-linear model are presented in Figure 5. Note that the different stiffness and damping characteristics are only due to the Payne effect; the static stiffness does not change in this amplitude range. The stiffness and damping change significantly over excitation amplitude. Dynamic stiffness is much higher than static stiffness at very slow excitation and decreases over amplitude. The loss angle typically increases over amplitude but reaches a maximum, depending on the tested amplitude range. The mount stiffness and damping characteristics are more affected by the changing excitation amplitude and less affected by frequency within the range up to 50Hz.

Figure 5 illustrates that the non-linear elastomer model is very accurate at sinusoidal excitation. A wide amplitude range is covered accurately although only a few input parameters were given for parameter identification. For durability load analyses high peak travels are expected for the mounts, including the non-linear progressive range of static stiffness curves. It can be concluded that non-linear models are needed particularly for simulation of durability loads and ride comfort, because here the frequency range of interest is small but the excitation amplitude significantly changes after every single obstacle.

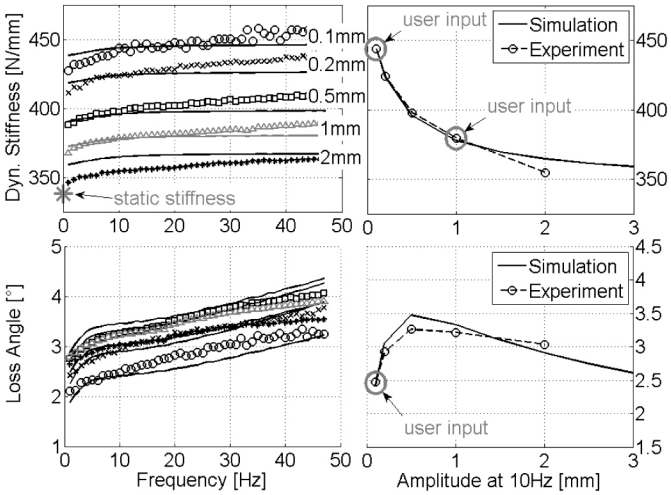

Figure 5. Dynamic behavior of elastomer bushing and simulation results for given user inputs at two displacement amplitudes at 10 Hz.

Cab Mount Modeling

Model Requirements

Standard bushing models in MBS environments do not take the Payne effect into account but give only a trade-off for a small amplitude range. To overcome this limitation various non-linear model approaches for elastomer parts can be found in literature. Sjøberg gave good insight into elastomer behavior [4] and developed models for a similar purpose. Berg [5] described a practical approach to model an amplitude-dependent friction force which was similarly used in [4] and [6]. Accuracy under sinusoidal excitation appears to be sufficient but the details of the numerical implementation into MBS will highly affect computing time, numerical stability and results under transient excitation. These models are not available for the chosen MBS environment whereas others lack a stable and easy to use parameter identification process.

For durability load prediction or misuse analyses the main purpose is to simulate dynamic behavior correctly at transient excitations using MBS environment; under the assumption that the mounts behavior at quasi-static and sinusoidal excitation is roughly known from experiments. Frequency domain analyses using transfer path models are not sufficient because stiffness and damping changes significantly and the excitations are not sinusoidal. Key requirements for the needed mount model are numerical stability under MBS environment; user-friendliness; model flexibility for a wide range of applications and computing time; in the priority as listed. Beside elastomer parts, similar models are also needed for hydraulically damped mounts.

Model Structure

The basic layout of the presented new non-linear model goes back to the approach of Pfeffer and Hofer [7] and uses a logarithmic increase of friction force like suggested by Lambertz [8]. It was chosen for this study because of the high accuracy and because only few model input parameters are needed that can be easily derived from standard experimental data. Numerical stability and the implementation into MBS environment had already been successfully validated [9], [10].

An extended model for hydraulically damped mounts is also available but out of scope of this study [11]. VI-grade offers a specifically tailored plug-in for use within the ADAMS/Car software and additional graphical user tools for easy parameter identification are available. Using this software, the bushing models can also be conveniently validated under sinusoidal and transient excitation, before the actual full-vehicle simulation in MBS environment is started.

Figure 6 shows the modular model structure with linear part for frequency dependence (F_{lin}) in parallel to a non-linear part for amplitude dependence due to the friction force (F_{NL}).

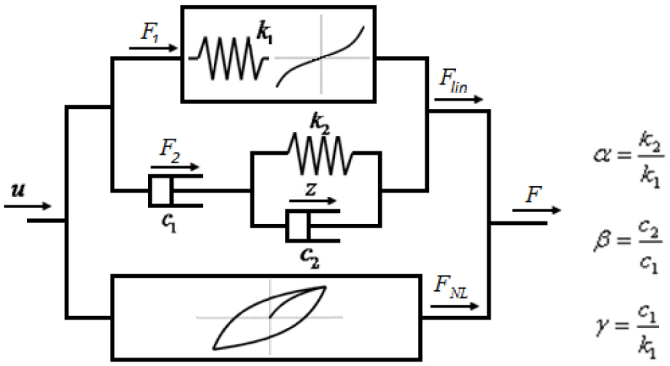

Figure 6. Model structure with linear, frequency dependent part in parallel to non-linear part for amplitude dependence

k_1 represents the main spring which may directly refer to the measured static stiffness k_{stat}. Non-linear static stiffness characteristics can be implemented here, so that k_1 is continuously calculated around the operating point from a table data approximation as shown in Figure 2.

k_2, c_1 and c_2 are linear spring and dashpot elements. In the following α, β and γ define the ratios of the spring and damper elements given in Figure 6.

Linear Frequency Dependent Part

If only the linear frequency dependent part of the model is used (F_{NL}=0) the resulting force F=F_{lin} can be calculated using the following equation:

$$F = k_1\left(u + \frac{c_1}{k_1}\cdot\left(\dot{u} - \dot{z}\right)\right) = k_1\left(u + \gamma\left(\dot{u} - \dot{z}\right)\right) \tag{4}$$

Where u is the overall displacement and $\dot{u}$ is the velocity. z is the displacement at the second spring k_2 and $\dot{z}$ is the derivative of z.

$\dot{z}$ is estimated by:

$$\dot{z} = \frac{1}{1+\beta}\cdot\left(\dot{u} - \left(\frac{\alpha}{\gamma}\right)\cdot z\right) \tag{5}$$

The force F_1 at the main spring is

$$F_1 = k_1 \cdot u\,. \tag{6}$$

And the force F_2 at the dashpot is

$$F_2 = k_2 z + c_2\dot{z} = c_1\left(\dot{u} - \dot{z}\right) \tag{7}$$

Even without the amplitude dependent friction part, the simulation gives a good fit for a small amplitude range, as shown in Fig. 7. In this case the stiffness k_1 has to be greater than the measured static stiffness k_{stat} in order to reach the wanted dynamic stiffness and compensate for the missing non-linear model part. E.g. k_1=355 N/mm for 0.2mm.

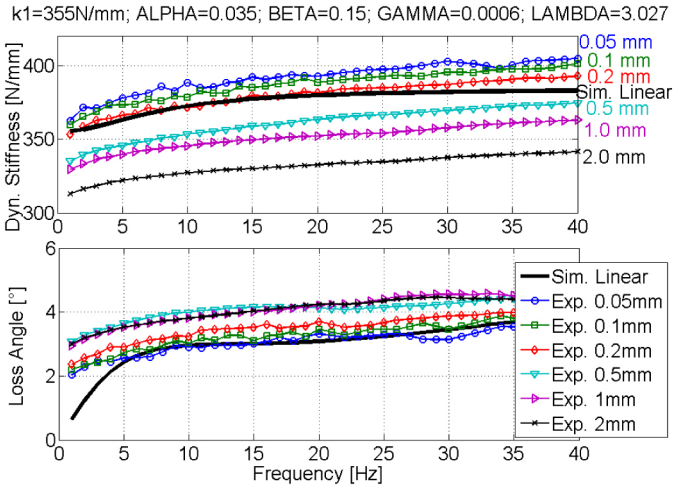

Figure 7. Evaluation of linear, frequency dependent model part: good fit for whole frequency range but simulation results are the same for any amplitude.

The linear part of the model on its own can already be used for frequency domain analyses or as a simplified model version [12]. Compared with the standard spring-damper model (see fig. 4) this linear model part already leads to improved accuracy, particularly for the damping characteristics. However, as any linear model approach the significant amplitude dependent properties are not taken into account but the model parameters have to be chosen in a way to offer a good trade-off for the whole amplitude range.

Non-Linear Amplitude Dependent Part

To give a good fit for all amplitudes an additional non-linear model part is needed. A logarithmic force increase was originally suggested by Lambertz [8] and proved to be beneficial because it accurately maps the wanted behavior at sinusoidal excitation. This part on its own creates additional damping and decreasing stiffness over amplitude.

$$F_{NL}(u) = RDL \cdot \ln\left(1 + \rho \cdot u\right) \tag{8}$$

Equation (8) is only defined within one branch of the hysteresis loop; in between two turning points of motion. To avoid a piecewise defined function, the displacement Δu since the last turning point of motion u_{TP} is used as input for calculation of force over time.

$$\Delta u = \left| u_{TP_i} - u_{TP_{i-1}} \right| \tag{9}$$

If displacement is used as input for force calculation, a force jump may appear at the beginning of the simulation in case the preload leads to a displacement offset. To improve the model start-up behavior it is beneficial to calculate the non-linear force from the integral of velocity, so that it always starts at zero:

$$F_{NL} = \int \frac{dF_{NL}}{dt} dt = \int \left(\frac{RDL \cdot \rho}{(1 + \rho \cdot \left| u_{TP_i} - u_{TP_{i-1}} \right|)} \cdot \dot{u} \right) dt \tag{10}$$

The resulting non-linear friction force F_{NL} at sinusoidal excitation is shown in Fig 8. Starting stiffness (A) at zero offset and after a full cycle at −2mm are the same. After the first turning point of motion (B) the slope of nonlinear force meets the starting point at C. Stiffness for the first half cycle A-B-C (+/−1mm) is significantly higher than the overall stiffness from B-D (+/−2mm). Using this approach, the friction force is not symmetrical around zero.

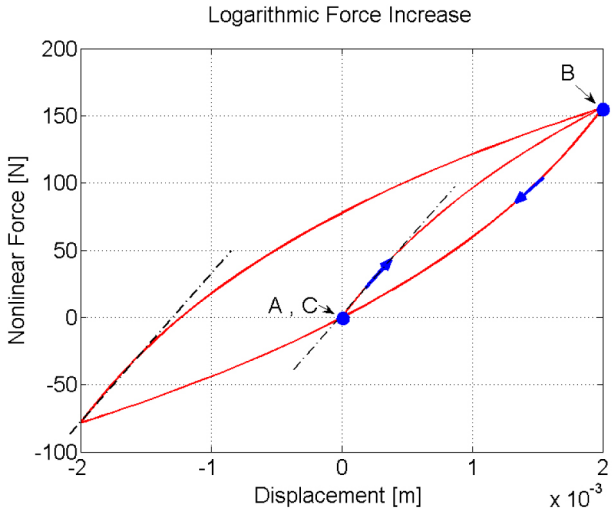

Figure 8. Logarithmic increase of non-linear friction force at sinusoidal excitation: Starting stiffness after turning points of motions are equal.

Logarithmic increase of friction force leads to the wanted behavior at sinusoidal excitation with increased damping over amplitude and decreasing stiffness over amplitude. $RDL \cdot \rho$ defines the starting stiffness at very small excitation. RDL is used to define the wanted stiffness and ρ leads to decreasing stiffness over amplitude. Figure 5 showed an example for model accuracy using the standard automatic parameter identification process.

Optional Force Limitation or Relaxation

Using the logarithmic friction force the behavior at sinusoidal excitation is mapped very well. However, in the physical parts additional relaxation can be observed where the material's internal stress is reduced over time. If this relaxation is not taken into account, unwanted model behavior may occur at superimposed, transient or random excitation. Unexpected force or displacement drift is reported for several non-linear model approaches.

It is very difficult to find good model parameters for relaxation over time for all possible test procedures and numerical details of simulations such as solver and integration time steps; because preloading, frequency, amplitude and the resulting non-linear friction forces cannot be foreseen.

Instead of relaxation over time, an additional limitation of the friction force was found to be beneficial for easy parameter identification, accurate results and numerical stability. Using this force limitation the accuracy at sinusoidal excitation stays qualitatively the same but model start-up behavior and model performance under transient or superimposed excitation are significantly improved. Here, the friction force does not disappear over time but is limited to a certain value and thereby forced to centre around zero in any case. The resulting force-displacement loops of the entire model lie are very similar to real parts. Smaller loops always lie inside the biggest force-displacement loop, even if preload changes or the static stiffness reaches progression. Figure 9 shows non-linear force increase for several amplitudes if this force limitation is taken into account. Please note that the friction force is now symmetric to zero whereas the purely logarithmic approach is not.

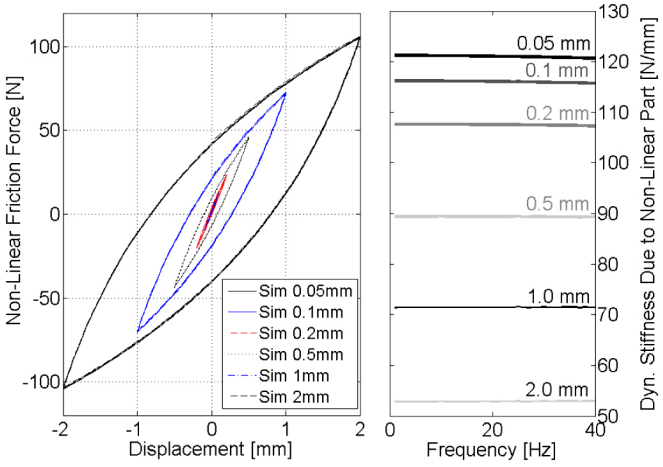

Figure 9. Nonlinear friction force with limit F_{max}=150 N at sinusoidal excitation and resulting dynamic stiffness: Force centers at zero and is symmetric.

The maximum friction force F_{max} has impact on loss angle over amplitude and is automatically calculated during the parameter estimation process. It may refer to the model internal parameters RDL and/or k_{stat}:

$$F_{\max} = F_{\max rel} \cdot k_{stat} \tag{11}$$

$$F_{\max\, rel} = n \cdot RDL \tag{12}$$

n is in the range of 0.1…1000. *n*=10 gives a good compromise for most cases. Alternatively, $F_{max\ rel}$ can be referred to static stiffness or taken from the hysteresis width *HW* at quasi-static excitation. Fig. 10 shows simulation for static stiffness curve using F_{max}=150N to ensure the overall hysteresis width is smaller than 300N (+/−150N).

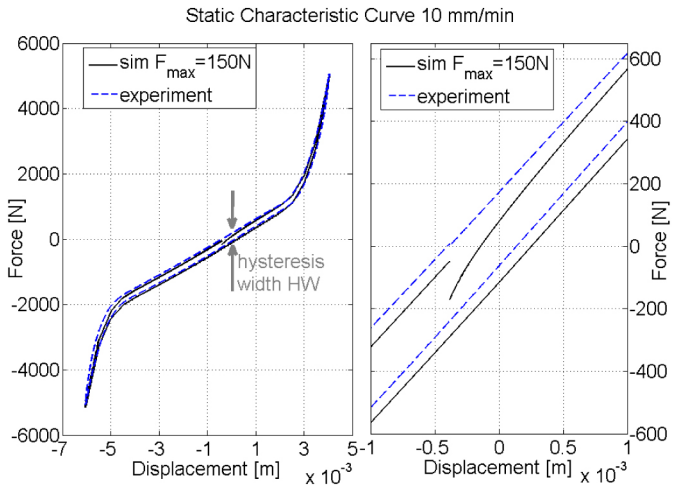

Figure 10. Measured hysteresis width HW to derive the maximum non-linear friction force F_{max}.

The simulation of the complete non-linear model is very close to the measured static hysteresis. This proofs numerical stability at very slow excitation and validates the correct overall force of a complete non-linear model using a table data with 21 values for the static stiffness curve. Model accuracy will be high under any preloading conditions.

Parameter Identification

Simulation results in Fig. 5 are very accurate under sinusoidal excitation even though only few input parameters are given for parameter identification. Each direction needs the following input data, listed in Table 1.

Static stiffness k_{stat} in N/m is calculated around the operating point with a given preload F_{av} leading to a displacement offset s_{av} as shown in figures 2 and 3. The normal operating point for parameter identification is usually given from drawings. If the preload changes during simulation, e.g. while braking or due to different loading conditions of the vehicle, the correct operating point is automatically calculated from the non-linear table data. Dynamic hardenings DH_1 and DH_2 are calculated from dynamic stiffness k_{dyn} at the layout frequency for specific amplitudes SA_1 and SA_2, divided by the static stiffness k_{stat}.

The damping characteristics are defined by the input parameter *delta* that represents the measured loss angle for the smaller amplitude SA_1 around the layout frequency *FREQ*.

Table 1. User input for parameter identification of new non-linear bushing model. Example values refer to Figure 5.

Parameter:	Symbol:	Value:
Static stiffness	k_{stat}	338 e3 N/m
Dynamic Hardening 1	DH_1	444/338 =1.314
@ Smaller amplitude 1	SA_1	0.1 e-3m
Dynamic Hardening 2	DH_2	380/338=1.124
@ Higher amplitude 2	SA_2	1.0e-3m
Loss angle	*delta*	2.47°@0.1mm
Layout frequency	*FREQ*	10 Hz
Maximum friction force	F_{max}	150N@2.0mm

If (parts of) the dynamic measurements are not available but only the static stiffness is known, an educated guess will also lead to reliable simulation results. It is therefore easy to get a basis for further investigations during an early phase of development; where the physical mounts may not be available, yet. Graphical user interfaces (GUI) are provided for parameter identification and to generate property files for Adams format.

Figure 11. Screenshot parameter identification GUI for automatic parameter estimation and export to property files for Adams.

For parameter identification, the frequency dependent model part can be analytically calculated in the frequency domain under the assumption that the static stiffness is constant around the operating point. With the excitation frequency Ω, overall displacement $\hat{U}$ and displacement $\hat{Z}$ at dashpot c_2:

$$i\Omega\hat{Z}e^{i\Omega t} = \frac{1}{1+\beta}\left(i\Omega\hat{U}e^{i\Omega t} - \left(\frac{\alpha}{\gamma}\right)\cdot\hat{Z}e^{i\Omega t}\right) \tag{13}$$

Rearranging:

$$\hat{Z} = \hat{U}\left((1+\beta) + \frac{\alpha}{i\Omega\gamma}\right)^{-1} \tag{14}$$

Substituting into

$$\widehat{F} = k_{stat} \cdot \widehat{U}\left(1 + i\Omega\gamma\left(1 - \left((1+\beta) + \frac{\alpha}{i\Omega\gamma}\right)^{-1}\right)\right) \tag{15}$$

The complex value of stiffness is described by K_d. The absolute value of K_d is the dynamic stiffness k_{dyn}.

$$k_{dyn} = |K_d| = \left|\frac{\widehat{F}(\Omega)}{\widehat{U}(\Omega)}\right| \tag{16}$$

The contributions of the individual model parts to the overall dynamic stiffness and loss angle cannot be simply added. Instead the real and imaginary components must be calculated separately from which the overall dynamic stiffness k_{dyn} is derived.

$$K_d = k_{dyn}\cos\delta + \left(k_{dyn}\sin\delta\right)\cdot i \tag{17}$$

The loss angle δ is the complex argument (or phase) of the complex dynamic stiffness K_d:

$$\delta = \arg\left(\frac{\widehat{F}(\Omega)}{\widehat{U}(\Omega)}\right) \tag{18}$$

These equations are computed in the parameter identification tool to find the best possible fit for the linear frequency dependent model part. The model internal parameters α, β and γ are tuned to ensure the resulting loss angle δ meets the user input *delta* within a certain tolerance. A brief parameter study is given in [12].

For calculation of the complete non-linear model k_{stat} can be substituted by a current stiffness k_{calc} for the specific frequency, amplitude and preload. The dynamic hardening and damping due to the amplitude dependent part including force limitation are finally calculated running a very simple simulation and iteratively changing *RDL*, ρ and F_{max} for a good fit over amplitude. If necessary, the model parameters for frequency dependence α, β and γ are then adjusted again.

In the latest practical implementation the whole model is scaled by the static stiffness at the operating point k_{stat} in N/m. This way it is easy to tune the mount characteristics by changing only k_{stat}. The loss angle characteristics will then stay the same but only dynamic stiffness changes.

Parameter Identification Process

Using the provided GUI for parameter identification all model internal parameters are calculated within a few seconds, without the need of time consuming manual iteration process. The process is intuitive and most steps are performed semi-automatically:

1. Choose direction
2. Load static stiffness curve and chose preload (operating point)
3. Load available dynamic measurements
4. Automatic parameter identification:
   a. Input parameters DH_1, DH_2, SA_1, SA_2, *FREQ* and *delta* are automatically derived from experiments.
   b. In case measurement data is missing, the model input parameters can be manually entered.
5. Plot results at sinusoidal excitation
6. Export model parameters into property file for Adams format.

Evaluation of Bushing Model

Non-linear static stiffness characteristics were taken into account by using table data from Figure 2 for the main spring k_1 of the model. The measured loss area (of the force-displacement loop) at very slow excitation and the progressive areas of the static stiffness curve are mapped very accurately as already shown in Figure 10 for an example bushing.

Amplitude dependence due to the Payne effect is covered using the logarithmic force increase over the displacement since the last turning point of motion. An additional limitation of this friction force improves start-up behavior at the beginning of simulation and ensures correct behavior under superimposed and transient excitations.

Sinusoidal Excitation

Figure 5 gave an example simulation that has been used to describe the parameter identification process. Figure 12 now presents actual simulation results for the tested mount type C that is used for further validation. Results at sinusoidal excitation are very accurate over the whole amplitude range.

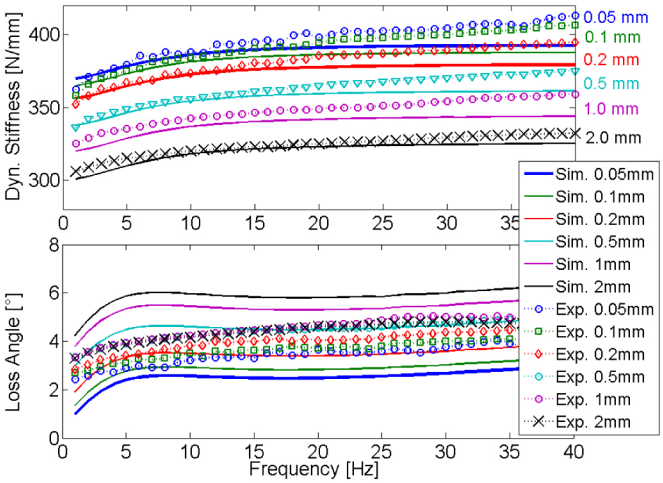

Figure 12. Model evaluation of complete non-linear model under sinusoidal excitation.

Model parameters are derived analytically from the equations for frequency domain; neglecting non-linear static stiffness curve, integration solver and time step etc. Accuracy of the dynamic stiffness over the whole amplitude range has higher priority over an optimal tuning of loss angle.

Durability Loads from Experiment

Model parameter identification is based only on quasi-static and sinusoidal excitation after the bushing has reached a steady-state. However, it is known that elastomeric parts exhibit different behavior under transient excitation. Here, the mount will vibrate mainly at a certain resonance frequency but the excitation amplitude is declining from its maximum value to zero after each single obstacle or input.

To evaluate the accuracy of the full-vehicle model using the new non-linear bushing models under transient excitation, the mount loads have been measured during on-road tests for durability. Based on these data a transient displacement signal has been generated as input for the mount test rig. The measured resulting forces from the test rig are qualitatively very similar to the loads during on-road tests.

Figure 13 presents the transient input displacement signal. The road contained in-phase bumps, out-of phase bumps, diagonal trenches, random potholes, cobblestones, alternating potholes, and transverse trenches. The following figures show model evaluation under such transient excitation for the mount type C which showed the biggest overall excitation range in the durability load signal.

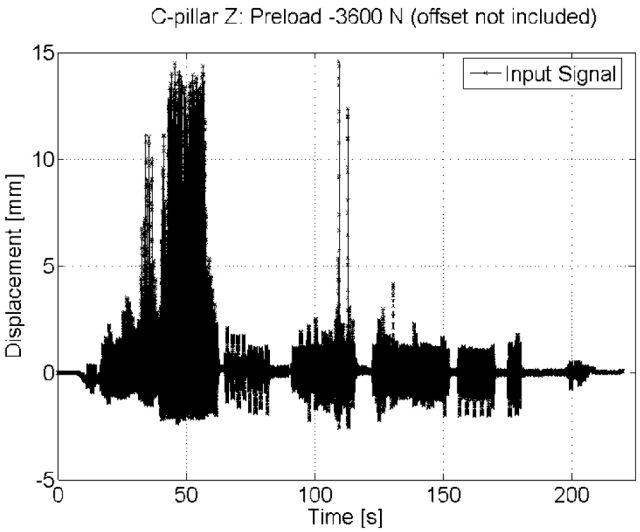

Figure 13. Input of transient durability load signal without offset due to preload

Figure 14 shows the resulting simulated and measured force over the displacement. The preload for parameter identification was significantly lower than during the durability load signal for model validation (see also Figure 2). Nevertheless, simulation results are very accurate. It can be seen that the non-linear characteristic of the underlying static stiffness is mapped very well.

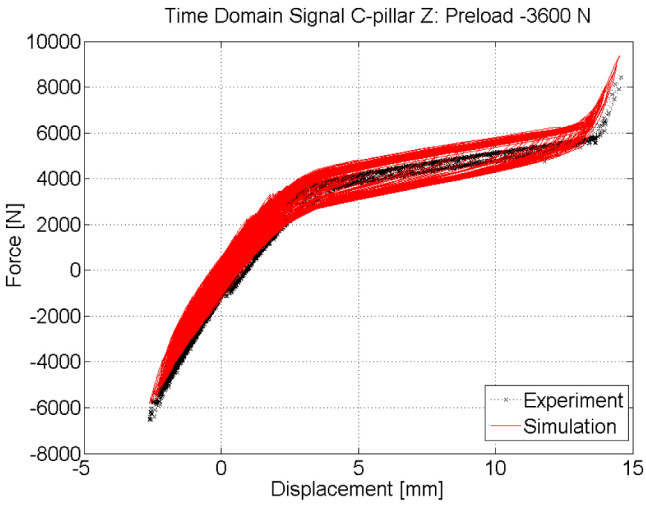

Figure 14. Model validation: Force-displacement loop of transient durability load signal

Figures 15 and 16 present the mounts load over time and details thereof. Overall, the simulation results for the mounts are very accurate. Further analyses will reveal the potential for improvement within full-vehicle simulation due to these new non-linear bushing elements.

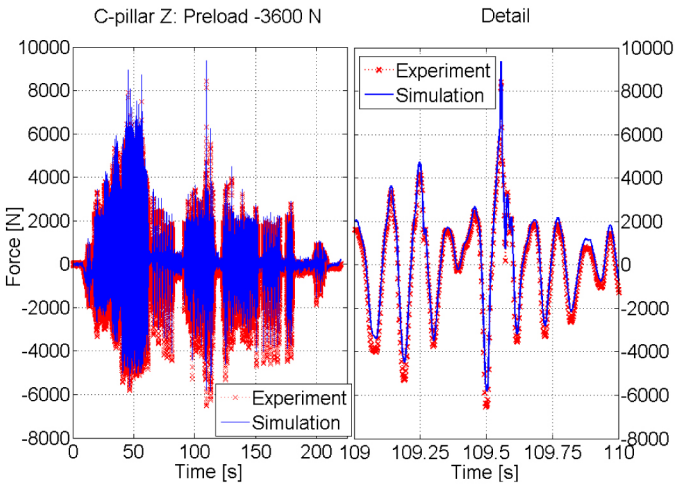

Figure 15. Model validation at transient input signal

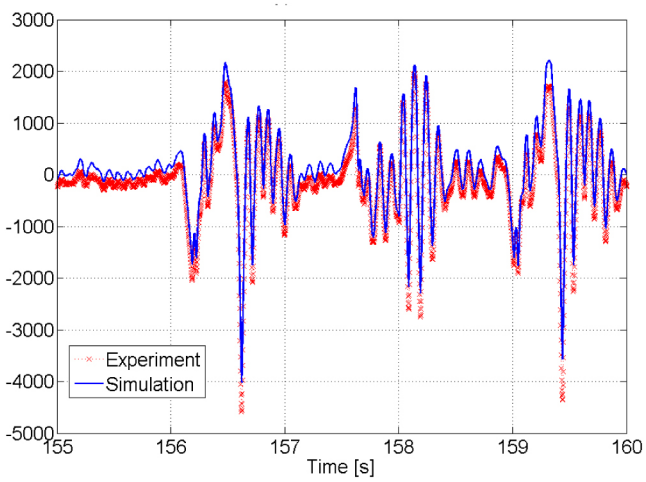

Figure 16. Model validation at transient input signal: Detail

Summary/Conclusions

MBS simulations are key in the vehicle development process. To accurately simulate the behavior of mounts and bushings it is not sufficient to take into account the progression of static stiffness curve. The Payne effect leads to significant dynamic hardening rations that depend on excitation amplitude. To improve the MBS full-vehicle simulation new non-linear models for mounts and bushings were presented and evaluated under sinusoidal and transient excitations.

The presented model has been originally developed for the purpose of ride comfort simulation for passenger cars. In this study it was used for durability load analyses of light duty trucks. In this case the excitation covers a wider amplitude range and the highly non-linear static stiffness characteristics are likewise relevant. Using the presented model increases the simulation accuracy. The model parameters can be easily derived from standard experimental data. The parameter identification process is briefly described; model internal parameters are semi-automatically derived from experiment using provided graphical user interfaces. Using the new amplitude dependent model within MBS environment the simulation results can be significantly improved for durability load analyses, prediction of ride comfort or ride handling. Results from full-vehicle simulation for durability loads will be published in the near future.

References

1. Roy, N. and Villaire, M., “Virtual Road Load Data Acquisition using Full Vehicle Simulations,” SAE Technical Paper 2013-01-1189, 2013, doi:10.4271/2013-01-1189.
2. Yu, Y., Naganathan, N. G., and Dukkipati, R. V., 2001, “A literature review of automotive vehicle engine mounting systems,” Mechanism and Machine Theory 36, 123-142.
3. Payne, A. R., “The Dynamic Properties of Carbon Black-Loaded Natural Rubber Vulcanizates Part I,” Journal of Applied Polymer Science, 1962, 6(19):57-63.
4. Sjøberg, M., “On Dynamic Properties of Rubber Isolators”, PhD Thesis, KTH Stockholm, 2002.
5. Berg, M., “A Non-Linear Rubber Spring Model for Rail Vehicle Dynamics Analysis,” Vehicle System Dynamics, 1998, 30: 197-212
6. Sedlaczek, K. Dronka, S. and Rauh, J., “Advanced modular modelling of rubber bushings for vehicle simulations,” Vehicle System Dynamics, 2011, 49(5): 741-759.
7. Pfeffer, P. E. and Hofer, K., “Simple Non-Linear Model for Elastomer and Hydro-Mountings,” *to Optimise Overall Vehicle Simulation*, 2002., ATZ worldwide, 2002, 2002-05
8. Lambertz, S., “Nichtlineares Materialgesetz für technische Gummiwerkstoffe mit deformationsabhängigen Eigenschaften und seine experimentelle Überprüfung an Gummifederelementen,” Berichte aus der Werkstofftechnik,. PhD Thesis, Aachen: Shaker, 1993.
9. Pfeffer, P. E., “Modelling and Simulation of the Elastomer and Hydromount Models (Generation 2) and their implementation in ADAMS,” 3rd VI-grade Users Conference, 13th -14th October 2010, Bad Nauheim, Germany
10. Buechler, H.-J., “Application of a new elastomer and hydromount model integrated in the full vehicle simulation process at Porsche: analysis of drive train vibrations on the example of the Panamera Diesel,” 4th VI-grade Users Conference, 18th-19th October 2011, Udine, Italy
11. Scheiblegger, C.; Pfeffer, P. E.; Karrer, H.; Geiger, N., “Modelling of Elastomer and Hydro Mounts for Ride Comfort and Handling Simulation,” 13th International VDI Congress Tires-Chassis-Road, 25th-26th October 2011; VDI Berichte, 2137; 247-268
12. Scheiblegger, C., Lin J. and Karrer H., “New non-linear bushing model for ride comfort and handling simulation: Focussing on linearization and the implementation into MBS environment,” Proceedings of the FISITA 2012 World Automotive Congress; Volume 10: Chassis Systems and Integration Technology; doi:10.1007/978-3-642-33795-6_38.

Contact Information

Christian.Scheiblegger@hm.edu

Acknowledgments

All experiments for mount characterization were carried out at Conti Tech Vibration and Control, Hanover. The Authors would like to thank the dept. of product testing development for consultancy and the valuable discussions regarding mount testing in general. Further thank goes to VI-grade for providing a customer tailored test version of user plug-in for Adams/Car and the support and advice for this study.

The Engineering Meetings Board has approved this paper for publication. It has successfully completed SAE’s peer review process under the supervision of the session organizer. The process requires a minimum of three (3) reviews by industry experts.

ISSN 0148-7191

http://papers.sae.org/2014-01-0880

6 HYDRO MOUNT MODEL

This chapter explains and introduces the newly developed hydro mount model within a study for durability loads of a light truck. The model shows excellent agreement to experimental data of a hydraulically damped cab mount and it also copes with more complex sorts of hydro mounts. The process to derive model parameters is briefly described and validated under the harsh conditions of the daily development process of a vehicle manufacturer. Other areas of use for the model are discussed. In the context of this thesis the hydro mount model is described and the use within MBS environment is evaluated.

6.1 Paper B 'Modeling Hydro Mounts in Vehicles for Durability Load Analyses, Ride Comfort and Vehicle Dynamics Simulation'

Paper B1 Scheiblegger, C., Roy, N., Hillis, A. J., and Pfeffer, P., "*Modeling Hydro Mounts in Vehicles for Durability Load Analyses, Ride Comfort and Vehicle Dynamics Simulation,*" AVEC 2016, Munich.

- **Hydro Mount Model**
- The author conducted most of the research independently. Model development and description, parameter identification and presentation of the results were his responsibility. (approx. 90% of content).

Paper B2 Scheiblegger, C., Roy, N., Hillis, A. J., and Pfeffer, P., "*Hydro mounts: An in-depth look at modeling hydro mounts in vehicles for durability load analyses, ride comfort and vehicle dynamics simulation*," Vehicle Dynamics International, Annual Showcase 2017.

- **Hydro Mount Model**
- Due to high interest on Paper B1 after the conference presentation and its publication, the authors were invited to republish the content for a wider public in a journal. (90% contribution of the lead author).

6.2 Contribution to Research

A new non-linear hydro mount model for MBS full-vehicle simulation is presented and validated through the example of durability load analyses for a light duty truck with hydro cab mounts. Starting from a simple modeling approach with constant stiffness for the main rubber

and chamber rubber, the principal phenomena of hydro mount behaviour are studied in detail. Accurate results are reached by correctly implementing the amplitude dependence of the mount's underlying rubber parts. The model is evaluated with experiments from a component test rig that covered a wide amplitude range; measured data from on-road durability events was used as the input.

The significance and originality of this article is that hydro mount behaviour is only predicted accurately, if the amplitude dependence of the underlying elastomer parts is taken into account. To cover the great diversity of mounts in the overall research, the hydro cab mount represents a rather simple design as a starting point.

For this research, the hydro mount model has been implemented into MBS environment with full functionality. Similar models exist for simple passive hydro mounts but there is no such flexible modelling approach for different types of mounts. The user tools for parameter optimisation developed in this study were evaluated by industry partners and proved to be practical and usable for the early phase of vehicle development.

Modeling Hydro Mounts in Vehicles for Durability Load Analyses, Ride Comfort and Vehicle Dynamics Simulation

Christian Scheiblegger [1], Nantu Roy [2], Peter Pfeffer [3], Andrew Hillis [4]
[1] CSC Vehicle Dynamics, [2] Fiat-Chrysler-Automobiles, [3] Munich University of Applied Sciences, [4] University of Bath
E-mail: Christian.Scheiblegger@CSC-Vehicle-Dynamics.com

Hydraulically damped mounts and bushings are crucial for vehicle handling, ride comfort and noise vibration and harshness (NVH). Multi-body simulation (MBS) software is used to calculate loads and vibrations; where simple mount models lead to trade-offs in the overall vehicle simulation accuracy.
A model for many sorts of hydro mounts is presented. Accurate results are reached by correctly implementing the amplitude dependence of the mount's underlying rubber parts.
The model is evaluated with experiments from a component test rig; with transient test signals from on-road durability events. Accuracy of full-vehicle simulation improves significantly, so that physical vehicle tests can be reduced to save costs and development time.

Modeling and Simulation / Vehicle Dynamics, Suspension / Integrated chassis control systems

1. INTRODUCTION

For heavy duty and light duty trucks reliability and robustness are key requirements and therefore the accurate prediction of durability load is crucial during development process. Multi body simulation tools are used to simulate the impact of different stiffness and position of the mounts and bushings in the early phase of development [1]. Prediction of road load using full-vehicle simulation is described in [2], where the tyre model has been validated and the excitation at wheel carrier / spindle loads proved to be correct. For further analyses along the load-path over suspension, frame into the body the level of details for all bushing elements needs to be increased. Fig. 1 shows the model of the pick-up truck used for this survey with several elastomer mounts and a hydro cab mount (C-pillar) being marked.

Elastomer mounts are widely used in automotive and railway applications [3]. Such parts exhibit amplitude dependent behavior due to the Payne effect [4]. The mounts stiffness and damping characteristics are sensitive to the excitation amplitude and frequency as well as preload conditions. This non-linear behavior also affects hydraulically damped mounts due to their underlying rubber parts.

In the standard development process, the amplitude dependence of rubber parts is not considered within the MBS environment but simple spring-damper models are used for cab mounts, suspension bushings and jounce bumpers. In [5] new amplitude-dependent bushing models were used for all cab mounts within the ADAMS/Car environment to improve full-vehicle simulation for durability loads. [6] discusses the overall improvement of full-vehicle simulation due to improved models for elastomer cab mounts and flexible car body structures, for a truck without hydro mounts. This paper presents a practical approach to model different sorts of hydro mounts in full-vehicle simulation.

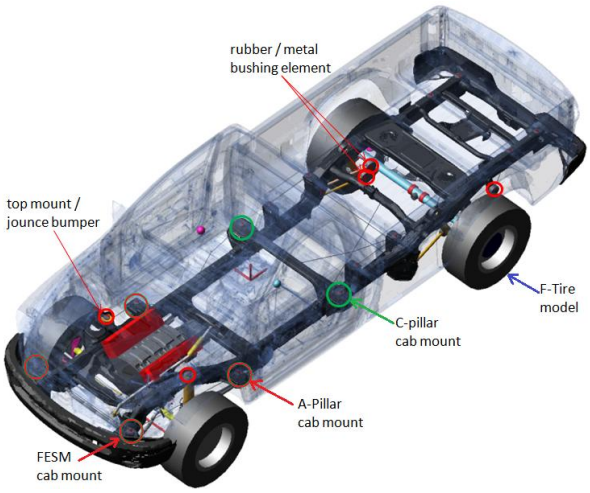

Fig. 1. The ADAMS model of a full-size pickup truck with a hydro cab mount (C-pillar) and several elastomer mounts

2 HYDRO MOUNT BEHAVIOUR

Fig. 2 shows photograph and scheme of the hydraulically damped cab mount that has been used for this survey. This cab mount is divided into the main rubber carrier on top and the hydraulic section with its fluid filled rubber chambers and the fluid channel.

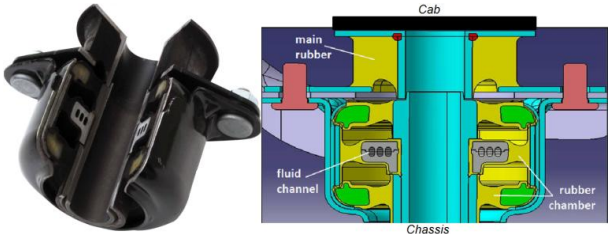

Fig. 2. Hydraulically damped cab mount with its main components.

Static stiffness k_{stat}, dynamic stiffness k_{dyn}, and loss angle δ are widely used to characterise mounts and bushings. This experimental data is used to derive model parameters for mount models within full-vehicle simulation. [7-9]. The mount's static stiffness k_{stat} depends on the loading conditions. Therefore, the following characteristics may depend on the preload.

The main rubber part carries the gravitational load of the cab and offers some damping. Under dynamic excitation a pressure difference from upper to lower chamber forces the fluid to pulsate with the spiral-formed fluid channel. A water-glycerin mix or oils are used as liquid.

Hydraulically damped mounts and bushings use the tuned mass damping effect (TMD) and additional fluid damping to generate high dynamic stiffness and high damping around the tuned resonance frequency. Hydro mounts changes dynamic stiffness and damping properties very significantly over frequency and over amplitude as shown in Fig. 3.

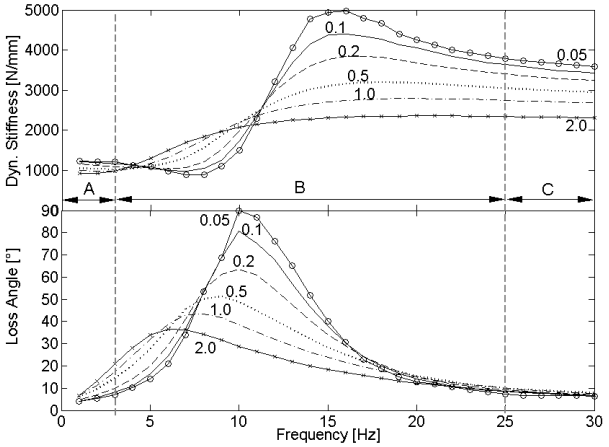

Fig. 3. Measured dynamic stiffness and loss angle of hydro cab mount for amplitude 0.05 mm – 2.0 mm

Measurement data at low frequency (A) already shows relevant difference in stiffness, due to amplitude dependence of main rubber. Fluid damping in the orifice and fluid friction lead to additional damping in the resonance frequency range (B). The internal damping also restricts the fluid flow at high frequencies (C). At high frequency fluid pulsation stops, so that the overall stiffness can be assumed to be main rubber stiffness plus stiffness against chamber compliance.

The hydro mount's typical resonance peak goes back to the tuned mass damping effect. Under certain operating conditions, the fluid inside the channel pulsates counter-phase-wise to the excitation. The rubber chambers act as a spring with volumetric stiffness to restrict chamber compliance. The fluid mass inside the channel is amplified by the hydraulic lever arm and acts as TMD mass. At high excitation the movement of the cab or powertrain is limited and damped at the same time. The fluid mass inside the channel, the rubber stiffness and chamber compliance are tuned to give high damping at certain resonance frequency. To study these underlying phenomena, a basic model is presented. The level of details will then be continuously increased to cover all effects.

3 HYDRO MOUNT MODEL

3.1 Model Structure

The principal hydro mount phenomena are discussed with the model approach as shown in Fig. 4. The presented model is of a modular structure where hydro mount model behavior is a superposition of:

- *Elastomer behavior* of its underlying rubber parts where c_T represents the main rubber stiffness (in vertical direction). The chamber stiffness c_B represents the resistance against puffing of chamber when pressure increases (chamber compliance, volumetric stiffness). Both springs for main rubber c_T and chamber rubber c_B are to be calculated from a sub-model for elastomer that takes into account amplitude dependence due to the Payne effects. c_T and c_B are to be regarded as complex stiffness and depend on the current preload, frequency, amplitude.
- *Tuned mass damping effect* with chamber compliance c_B, main rubber stiffness c_T and fluid mass m_K as main factors of impact. The virtual fluid mass m_K is known from channel length l_K, channel area A_K and fluid density ρ_F. The pulsation in the fluid channel is amplified over hydraulic lever arm, where the areas of the main spring A_0, the chamber A_B and fluid channel area A_K are relevant.
- Additional *fluid damping* in the channel and orifice depending on the velocity of fluid flow; damping coefficients d and β for linear or non-linear fluid damping.

Physically meaningful parameters are used to model the mount. A force on top of the hydro mount due to gravitational load leads to deflection u_0 of the main rubber spring c_T and increase of pressure in upper chamber p_0:

$$F = c_T \cdot u_0 + p_0 \cdot A_B \qquad (1)$$

When pressure p_0 increases due to the force F the chamber displacement (deflection) u_B results from the pressure in the upper chamber p_o.

$$p_0 \cdot A_B = u_B \cdot c_B \qquad (2)$$

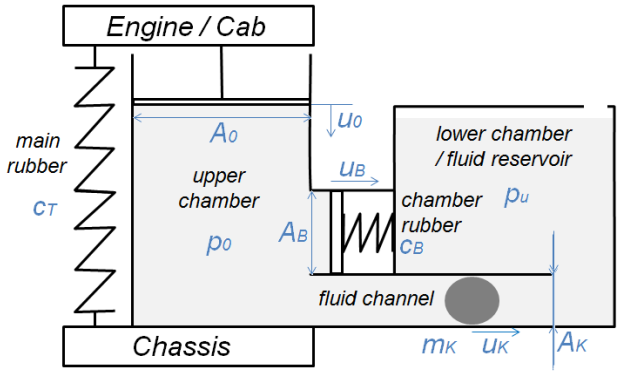

Fig. 4. Simple hydro mount model for principal investigations.* Springs represent complete nonlinear amplitude-dependent elastomer sub-models.

The fluid (mass m_K and displacement u_K) flows through the channel with length l_K and cross sectional area A_K while d and β are damping coefficients for linear and non-linear fluid damping in the channel, respectively:

$$m_K \cdot \ddot{u}_K = p_0 \cdot A_K - d \cdot \dot{u}_K - d \cdot \beta \cdot \dot{u}_K{}^2 \cdot sign(\dot{u}_K) \quad (3)$$

In simple passive engine mounts the lower chamber consists of a flexible rubber diaphragm membrane and acts as fluid reservoir with atmospheric pressure p_u=0. Even if the lower chamber is physically closed and under pressure, this assumption p_u=0 still gives a good agreement to experimental data, as will be discussed, later on.

For further simplification it is assumed that the main rubber area is the same as chamber area.

$$A_0 \approx A_B \quad (4)$$

A change of input displacement at slow excitation does not affect the pressure p_0 inside the mount because fluid flows freely through the channel without relevant damping and mass inertia. Therefore, input displacement u_0 only goes into the calculation of F_T due to the rubber spring c_T. Chamber deflection of u_B is calculated from the integral of velocity du_0 over time; thereby eliminating a constant displacement offset due to static gravitational load onto the mount.

$$u_B = \int \left(\dot{u}_0 - \dot{u}_K \frac{A_K}{A_B} \right) \quad (5)$$

Pressure can be calculated as:

$$p_0 = \frac{u_B \cdot c_B}{A_B} = \int \left(\dot{u}_0 - \dot{u}_K \frac{A_K}{A_B} \right) \cdot \frac{c_B}{A_B} \quad (6)$$

The model approach shown in Fig. 4 has been implemented into MBS environment, a software plug-in for MSC.Adams/Car is available from VI-grade [10-13]. Furthermore, sophisticated graphical user interfaces have been developed for import of measurement data, parameter estimation and export into parameter files. These tools include a virtual mount test rig and have been used for the following hydro mount design analyses. All sub-functionalities of the hydro mount model can be deactivated.

3.2 Non-linear Fluid Damping

Beside the fluid mass' inertia, a velocity-proportional term with damping coefficient d and an additional non-linear damping term with coefficient ß contribute to the damping in the fluid channel. It may be suggested that linear and non-linear parts should be regarded entirely separated, so that:

$$p_0 \cdot A_K = m_K \cdot \ddot{u}_K + d \cdot \dot{u}_K + \beta \cdot \dot{u}_K{}^2 \cdot sign(\dot{u}_K) \quad (7)$$

However, numerous tests where the mount model parameters were identified for different sorts of hydro mounts (and hydro bushings) proved that it is beneficial to assume the main damping coefficient d has impact on the non-linear damping term ß, also.

$$p_0 \cdot A_K = m_K \cdot \ddot{u}_K + d \cdot \left(\dot{u}_K + \beta \cdot \dot{u}_K{}^2 \cdot sign(\dot{u}_K) \right) \quad (8)$$

This way the main characteristics can be estimated easily and fast via the damping coefficient d. Parameter variation for ß then gives fine-tuning of the behaviour. This coupling of linear and non-linear damping leads to significant simplifications and improved stability for a semi-automatic parameter estimation process where many model internal parameters are varied for a good fit to experimental data.

For model implementation into a practical tool for hydro mount simulation and design studies, several options for fluid damping are useful. So, a more general formulation is used, where:

$$F_{fluid} = p_0 \cdot A_K = F_{TMD} + F_{damp1} + F_{damp2} \quad (9)$$

With $F_{TMD} = m_K \cdot \ddot{u}_K$ and $F_{damp1} = d \cdot \dot{u}_K$ (10)

Plus additional non-linear damping

$$F_{damp2} = \beta \cdot \dot{u}_K{}^2 \cdot sign(\dot{u}_K) \quad (11)$$

Or alternatively

$$F_{damp2} = \beta \cdot \dot{u}_K{}^3 \quad (12)$$

For the final model implementation the grade of nonlinearity can be changed via exponential coefficient n_{POW}. where n_{POW}=1, 2 or 3. A continuous formulation for changing signs for velocity is needed to ensure low computing times when variable time step solvers are used. The sign of velocity is therefore calculated using a tangens-hyperbolicus-function with gradient factor k_{SingD}. The discontinuous sign function and its derivative is thereby replaced with continuous function.

$$F_{damp2} = \beta \cdot \dot{u}_K{}^{n_{POW}} \cdot \tanh(k_{SignD} \cdot \dot{u}_K) \quad (13)$$

3.3 Elastomer Model

For hydro mount models it is often assumed that main rubber stiffness and chamber stiffness are constant. In reality main rubber stiffness c_T and chamber rubber stiffness c_B change over frequency and over amplitude.

* German notation for springs has been kept with cT for the dynamic stiffness of main rubber (top mount/Tragfeder) and cB of chamber rubber (bulge stiffness/Blähfeder) because earlier model versions are still in use that refer to cT and cB as model parameters in the user interfaces.

Table 1 shows model parameters for the cab mount for the basic model approach when main rubber *cT* and chamber compliance *cB* are assumed to be constant springs and fluid damping is non-linear. With this simplification underlying effects can already be studied. Due to such simplifications the table values may but must not be equal to physical part's geometry. Instead, model parameters are estimated first and then automatically tuned for a good fit to experimental data.

Table 1. Model parameters for basic hydro mount model with constant stiffness for main rubber and chamber rubber.

Parameter:	**Symbol:**	**Value:**
Stiffness top mount (main rubber)	c_T	1e3 kN/m
Effective piston area chamber	A_B	8.586e-3 m²
Area of fluid channel	A_K	8.191e-5m²
Length of fluid channel	l_K	0.248428 m
Fluid damping coefficient linear	D	0.333 Ns/m
Non-linear fluid damping coeff.	β	1.393 Ns²/m²
Effective channel fluid mass	m_K	0.019333 kg
Chamber stiffness	c_B	1643e3 N/m

Fig. 6 gives measurement for three amplitudes (markers) and simulation results (in solid lines) using the table values below derived from automatic parameter optimisation.

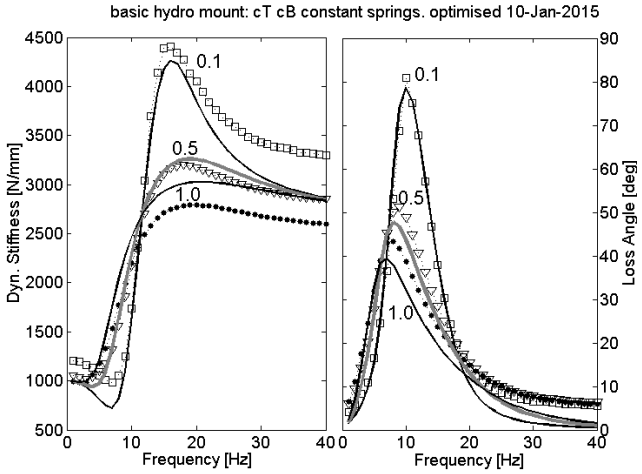

Fig. 5. Simulation (solid lines) assuming constant springs for main rubber and chamber rubber

Simulation results look good at first glance, but such a simplified model reveals the following drawbacks because stiffness for main rubber c_T and chamber rubber c_B are considered to be constant:

- Stiffness of main rubber is constant so that static and dynamic stiffness are the same. The static stiffness is estimated too high if c_T is tuned for good results under dynamic excitation; the static equilibrium of the full-vehicle model will be inaccurate, leading to severe drawbacks if the simulation runs for complex 3D excitation.
- The calculated stiffness is the same for all amplitudes at low frequency (1Hz) and at high frequency (>30Hz). In contrast, measurement shows relevant differences due to the elastomer behavior.
- The simulation behavior at transient excitation might be different to the real parts, due to simplifications.

For better results and to make the hydro mount model flexible for all sorts of different hydro mounts and hydro bushings, it is vital to accurately model the elastomer's amplitude dependence and frequency dependence.

Standard bushing models in MBS environments do not take the elastomer amplitude dependence due to the Payne effect into account. For accurate results, it is crucial that the hydro mount's elastomer parts are modeled in details. For the simulation of durability loads high amplitudes and changing preloads are of interest, so that special care has to be taken in terms of modeling the elastomer parts of a hydro mount. [5] describe a new non-linear model for elastomer mounts that is used as sub-module for the elastomeric parts (main rubber c_T and chamber rubber c_B) within the hydro mount model in Fig. 4.

Similar non-linear models for conventional rubber mounts and bushings that take into account amplitude dependence are presented in [23-28]. There are many papers onto the topic but only few models have been implemented into MBS environment with full functionality to prove practical use and numerical stability. Others lack easy to use tools for fast parameter identification.

Main outcome of this research is that all sorts of (passively) hydraulically damped mounts and bushings can be simulated equally well, (only) if the underlying model approaches for the elastomer parts are accurate.

3.3 Optional Hydro Mount Features

Beside the simple hydro cab mount the presented mount model is also able to accurately map different sorts of hydro mounts and hydraulic suspension bushings. A decoupling functionality and bypass valve for hydro suspension bushings are also implemented in the model, but not discussed herein. A linearized model version for high frequencies and its specific extension for active hydraulic engine mounts is discussed in [33].

3.4 Parameter Identification Process

The parameter estimation process is performed semi-automatically with the help of sophisticated graphical user-interfaces. The following work steps are recommended:

A) Load measurement data for static and dynamic experiments
B) Define preloading conditions for static stiffness
C) Automatically set initial values for the parameter optimization to commence on.

D) Decide for the level of details of the model. Depending on existing measurement data and physical mount properties, certain nonlinearities are taken into account or can be neglected for simplification. E.g. if the mount is decoupled at small amplitudes or has additional bypass valve more parameters need to be varied.
E) Run automatic parameter optimization program.
F) Calculation of damping coefficients, for fluid pressure in the upper chamber and elastomer properties are automatically carried out.
G) Export model parameters to property file

The automatic parameter optimisation process takes in average 5-15 minutes, depending on the given measured amplitudes and frequency steps and how many model internal parameters are varied. Due to the complexity of the programming it is not further discribed, herein.

4 MODEL EVALUATION

4.1 Sinusoidal Excitation

The cab mount shown in Fig. 1 is used for further validation. Fig. 6 presents actual simulation results for the full non-linear model including amplitude dependence for elastomer parts.

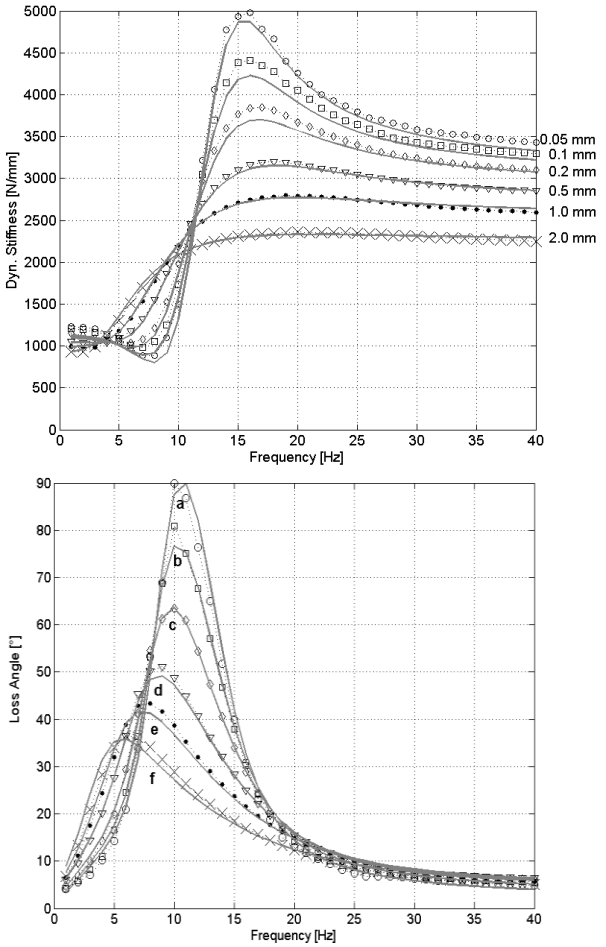

Fig. 6. Hydro mount model evaluation under sinusoidal excitation: Simulation (solid lines) and measurement for amplitudes 0.05 mm (a) 0.1 mm (b) 0.2 mm (c)0.5 mm (d) 1.0 mm (e) and 2.0mm (f)

The springs for c_T and c_B in the principal model scheme (Fig. 4) are represented by a full non-linear elastomer model including amplitude dependence.
All measured amplitudes 0.05 mm, 0.1 mm, 0.2 mm, 0.5 mm, 1.0 mm and 2.0 mm have been used during the automatic parameter optimisation routine.

Error values are calculated for each amplitude and frequency for loss angle as well as frequency during parameter optimization. In this case, the error sums for dynamic stiffness and loss angle have been weighted equally important.

Results at sinusoidal excitation are very accurate over the whole amplitude range if amplitude dependent effects due to the underlying rubber parts are taken into account. This type of mount has no decoupler or bypass valve, so that it can be compared with most passive hydraulic engine mounts.

Transient behavior / reaching steady state

At most tests on the component test rig, transient phenomena are neglected because the mount is fixed onto the test rig on both sides. Per test definition, the mount is allowed to reach steady state before force-displacement loops are recorded and dynamic stiffness and loss angle are calculated thereof.
In contrast, for real world excitation the behavior before reaching steady-state is crucial to tune the mounts and bushings. Additional to the dynamic stiffness and loss angle (or other parameters to characterize the damping properties) the actual transient response at freely damped vibration is relevant. [14, 16, 19] discuss some limitations of similar modeling approaches for the prediction of transient excitations.

For model evaluation in this study, transient test rig signals have been derived from real on-road tests as input on the mount test rig. Moreover, the improvement of such hydro mount model into full-vehicle simulation had been briefly studied in [5, 20].

In this paper, the dynamic characteristics are mainly studied from dyn. stiffness and loss angle because these are the most commonly used parameters for standard dynamic measurement data. [14] suggest to use complex imaginary stiffness instead of loss angle for the hydro mount characterization. In any case, the calculation of complex stiffness is based on the assumption of elliptical hysteresis loops but that is not always the case. Therefore, transient signals have also been used for the model evaluation.
Hydro mount behavior at transient excitation and limitations of modeling approaches are discussed in [15-19]. [21] studies the transient response of hydro mounts and also revealed that the force during expansion is significantly lower than under compression, due to limited pressure. Measurement data for pressure inside the mount has not been available for our studies, because the parts would have to be destroyed.
[22] discuss the scattering of measurement data within the samples of a batch of hydraulic engine mounts and

found the characteristics can highly vary over the production range. In order to eliminate this influence, on-road vehicle tests have been performed with the specific mounts after they had been tested on the test rig.

4.2 Durability Loads from Experiment

Model parameter identification is based only on quasi-static and sinusoidal excitation after the bushing has reached a steady-state. However, it is known that elastomeric parts exhibit different behavior under transient excitation. Here, the mount will vibrate mainly at a certain resonance frequency but the excitation amplitude is declining from its maximum value to zero after each single obstacle or input.

To evaluate the accuracy of the full-vehicle model using the new non-linear bushing models under transient excitation, the mount loads have been measured during on-road tests for durability. Based on these data a transient displacement signal has been generated as input for the mount test rig. The measured resulting forces from the test rig are qualitatively very similar to the loads during on-road tests.

Fig. 7 presents the transient input displacement signal with high deflections. The road contained in-phase bumps, out-of phase bumps, diagonal trenches, random potholes, cobblestones, alternating potholes, and transverse trenches. The following model evaluation shows results for the hydraulically damped cab mount.

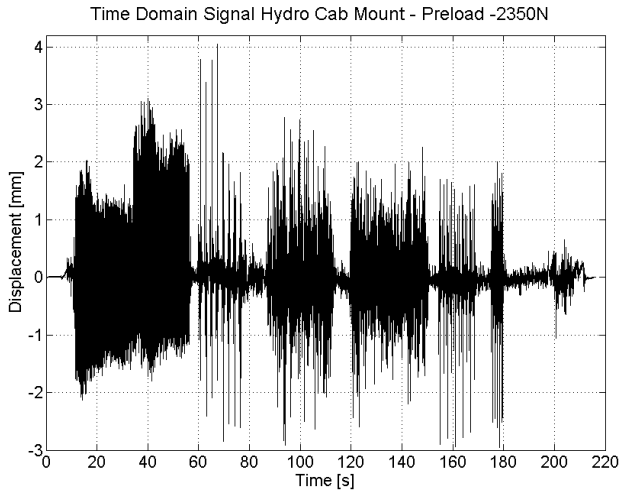

Fig. 7. Input of transient durability load signal without offset due to preload

Fig. 9 gives the resulting simulated and measured force over the displacement. The resulting force offset due to preload has been terminated for the following plots. The preload for parameter identification was significantly lower than during the durability load signal for model validation. Nevertheless, simulation results are very accurate. Please note that the overall force-displacement loops are not purely elliptical because the internal pressure inside the mount's chamber is limited during decompression after high deflections; damping is much higher under compression. The good results prove that the pressure inside the upper chamber was modeled correctly and accurately.

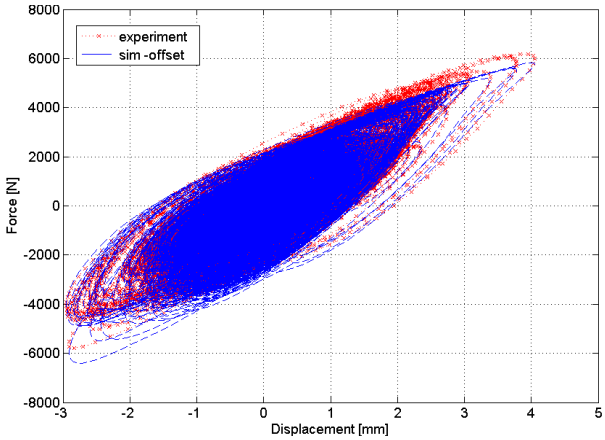

Fig. 8. Model validation: Force-displacement loop of transient durability load signal

Figs. 10 and 11 present the mounts load over time and details thereof. Overall, the simulation results for the mounts are very accurate.

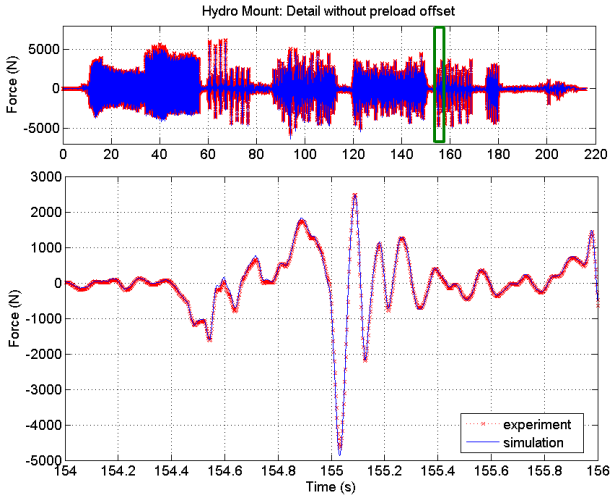

Fig. 9. Model validation at transient input signal

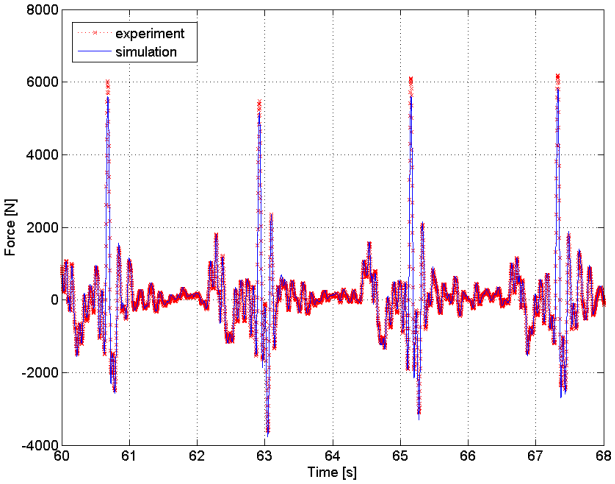

Fig. 10. Model validation at transient input signal: Detail

The model evaluation under sinusoidal excitation already proved a very high model performance over a wide amplitude range. The evaluation with a transient time signal on the mount test rig also confirms a very high level of accuracy.

SUMMARY / CONCLUSIONS

MBS simulations are vital for the vehicle development process and the bushing elements along the load path are crucial for the overall accuracy of the full vehicle model. Elastomer parts exhibit significant dynamic hardening ratios that depend on excitation amplitude and preload. This behavior also highly affects hydro mounts due to its underlying rubber parts.

A non-linear hydro mount model for MBS full-vehicle simulation was presented and validated on the example of durability load analyses for a light duty truck with hydro cab mounts. Starting from a simple modeling approach with constant stiffness for main rubber and chamber rubber, the principal phenomena of hydro mount behavior have been studied. Similar models exist for simple passively damped hydro engine mounts but there is no such flexible modeling approach for different types of mounts: simple passive hydro engine mounts as well as partially or fully decoupled hydro engine mounts can be covered and results are also accurate for hydro suspension bushings.

Main conclusion of this investigation is that hydro mount behavior is only mapped accurately, if the amplitude dependence of the underlying elastomer parts is taken into account. To improve accuracy of other existing mount models in MBS it is recommended to implement the amplitude dependent characteristic of the underlying elastomer parts.

The model evaluation under transient excitations has covered a wider amplitude range; simulation showed very good agreement to measured loads. With the presented model for the hydro cab mount the full-vehicle simulation accuracy improved significantly. Testing times and prototypes can therefore be reduced, to save cost and development time.

REFERENCES

1. Yang X and Xu P. "Road Load Analysis Techniques in Automotive Engineering," Metal Fatigue Analysis Handbook 2012. p. 1-60.
2. Roy, N. and Villaire, M., "Virtual Road Load Data Acquisition using Full Vehicle Simulations," SAE Technical Paper 2013-01-1189, 2013, doi:10.4271/2013-01-1189
3. Yu, Y., Naganathan, N. G., and Dukkipati, R. V., "A literature review of automotive vehicle engine mounting systems," Mechanism and Machine Theory, 2001, Vol. 36, 123-142 .
4. Payne, A. R., "The Dynamic Properties of Carbon Black-Loaded Natural Rubber Vulcanizates Part I," Journal of Applied Polymer Science, 1962, 6(19):57-63.
5. Scheiblegger, C., Roy, N., Silva Parez, O., Hillis, A. et al., "Non-Linear Modeling of Bushings and Cab Mounts for Calculation of Durability Loads," SAE Technical Paper 2014-01-0880, 2014, doi:10.4271/2014-01-0880
6. Roy, N., Scheiblegger, C., Darling, J. et al., "Durability Loads Prediction of Body-on-Frame Vehicles using Full Vehicle Simulation," Int. Journal of Passenger Cars, forthcoming
7. VDI standard, "VDI 3880: Damping of Materials and Members: Damping of Solids," ed, 2004.
8. DIN standard 53 535, "Grundlagen für dynamische Prüfverfahren," ed. Berlin: Beuth Verlag, 1982.
9. Cardillo, R.M., "Dynamic testing of elastomer mountings," *Journal of Applied Polymer Science*, vol. 8, pp. 53-71, 1964.
10. www.vi-grade.com.
11. Pfeffer, P., "Modelling and Simulation of the Elastomer and Hydromount Models (Generation 2) and their implementation in ADAMS," 3rd VI-grade Users Conference, 13th -14th October 2010, Bad Nauheim, Germany
12. Buechler, H.-J., "Application of a new elastomer and hydromount model integrated in the full vehicle simulation process at Porsche: analysis of drive train vibrations on the example of the Panamera Diesel," 4th VI-grade Users Conference, 18th-19th October 2011, Udine, Italy
13. Pfeffer P., Scheiblegger, C., Roy, N., Ortmann, C. "Models for elastomeric and hydraulically damped vibration isolators within full vehicle simulation" 2014 VI-grade Users Conference, 11th-12th April 2014, Pollenzo – Bra (CN), Italy
14. Barker, M., "The Behaviour of Non-Linear Hydraulic Isolators" In: Engineering Integrity, 2004, Vol. 15, No. 1, pp.28–42.
15. Singh, R., Tiwari, M., Adiguna, H., Hrovat, D. et al. "Transient Response Evaluation of a Hydraulic Engine Mount," In: Sound and vibration, 2002, Vol. 36, No.7, pp.30–35.
16. Lee, J.-H.; Bae, M.-S.; Kim, K.-J., "Limitations of Mechanical Model With Lumped Mass in Representing Dynamic Characteristics of Hydraulic Mount," (SAE 2003-01-1466) In: SAE Transactions; Journal of Passenger Cars - Mechanical Systems, Vol. 112, No. 1, pp.1679–1683, doi: 10.4271/2003-01-1466
17. Lee, J.-H. and Kim, K.-J.,"An Efficient Technique for Design of Hydraulic Engine Mount via Design Variable-Embedded Damping Modeling," In: Journal of Vibration and Acoustics, 2005, Vol. 127, No. 1, pp.93–99
18. He, S., Singh, R., "Discontinuous compliance nonlinearities in the hydraulic engine mount," In: Journal of Sound and Vibration, 2007, Vol. 307, pp.545–563
19. Lee, J.H., Singh, R., "Critical analysis of analogous mechanical models used to describe hydraulic engine mounts, " In: Journal of Sound and Vibration, 2008, Vol. 311, pp.1457–1464. doi:10.1016/j.jsv.2007.10.021.

20. Scheiblegger, C., Pfeffer, P. E., Karrer, H., Geiger, N., "Modelling of Elastomer and Hydro Mounts for Ride Comfort and Handling Simulation," 13th International VDI Congress Tires-Chassis-Road, 25th-26th October 2011; VDI Berichte, 2137; 247-268
21. Adiguna, H., Tiwari, M., Singh, R., Tseng, H. E. et al., "Transient response of a hydraulic engine mount," *Journal of Sound and Vibration*. 2003, 268 (2):217-248, doi: 10.1016/s0022-460x(03)00076-2.
22. Mitsch, M., Mack, W. and Falkner, A., "On the scattering of test data and the significance of the standard coefficients 'dynamic stiffness' and 'loss angle' for hydraulic engine mounts," *Vehicle System Dynamics*, vol. 48: 387-403, 2010, doi: 10.1080/00423110902898077.
23. Sjøberg, M., "On Dynamic Properties of Rubber Isolators", PhD Thesis, KTH Stockholm, 2002.
24. Berg, M., "A model for rubber springs in the dynamic analysis of rail vehicles," In: Proceedings of the Institution of Mechanical Engineers, Part F: Journal of Rail and Rapid Transit, 1997, Vol. 211.
25. Berg, M., "A Non-Linear Rubber Spring Model for Rail Vehicle Dynamics Analysis," Vehicle System Dynamics, 1998, 30: 197-212
26. Dronka, S., Rauh, J., "Modell zur Simulation von Fahrwerks-Gummilagern. Eigenschaften – Modellstruktur – Parametrierung," In: VDI-Berichte, 2007, Vol. 2003, pp.371–390
27. Sedlaczek, K. Dronka, S. and Rauh, J., "Advanced modular modelling of rubber bushings for vehicle simulations," Vehicle System Dynamics, 2011, 49(5): 741-759.
28. Williams, H. T., Whear, R., "Elastomer Models for Virtual Mounting Systems," SAE Technical Paper 2005-01-1075, 2005, doi: 10.4271/2005-01-1075
29. Pfeffer, P. E. and Hofer,K., "Simple Non-Linear Model for Elastomer and Hydro-Mountings," *to Optimise Overall Vehicle Simulation,* 2002., ATZ worldwide, 2002, 2002-05
30. Lambertz, S., "Nichtlineares Materialgesetz für technische Gummiwerkstoffe mit deformationsabhängigen Eigenschaften und seine experimentelle Überprüfung an Gummifederelementen," Berichte aus der Werkstofftechnik,. PhD Thesis, Aachen: Shaker, 1993.
31. Peeken, H., Lambertz, S. (1994): Nichtlineares Materialmodell zur Beschreibung des Spannungs-Dehnungsverhaltens gefuellter Kautschuk-Vulkanisate. In: Konstruktion: Organ Der VDI Gesellschaft Konstruktion und Entwicklung, Vol. 46, No. 1, pp.9–15.
32. Scheiblegger, C., Lin, J. and Karrer, H., "New non-linear bushing model for ride comfort and handling simulation: Focussing on linearization and the implementation into MBS environment," Proceedings of the FISITA 2012 World Automotive Congress, 2013, Volume 10: Chassis Systems and Integration Technology; doi: 10.1007/978-3-642-33795-6_38
33. Hausberg, F., Scheiblegger, C., Pfeffer, P., Plöchl, M., Hecker, S., Rupp, S., "Experimental and analytical study of secondary path variations in active engine mounts," Journal of Sound and Vibration, **340** (2015), 22 - 38.
34. Whear, R., Williams, H. T., "Advanced Hydraulically Damped Elastomeric Component Models," In: SAE Transactions; Journal of Passenger Cars - Mechanical Systems, 2005, Vol. 114,
35. Sauer, W., Guy, Y., "Hydro Bushings - Innovative NVH Solutions in Chassis Technology," SAE Technical Paper 2003-01-1475, 2003, doi: 10.4271/2003-01-1475

ACKNOWLEDGEMENTS

All experiments for mount characterization were carried out at Conti Tech Vibration and Control, Hanover. The Authors would like to thank the dept. of product testing development for consultancy and the valuable discussions regarding mount testing in general. Further thank goes to VI-grade for providing a customer tailored test version of user plug-in for Adams/Car and the support and advice for this study.

7 STUDY ON ACTIVE HYDRO MOUNTS

This chapter discussed active engine mounts (AEM) as a more complex extention of the previously discussed types of elastomer and hydro mounts. Although the models are not designed specificially for AEM parts of it can be used to cope with their behaviour. Within the context of this thesis this paper gives a wider context of areas of use for the presented mount models, the methodology for parameter estimation and underlying mathematical methods to cover similar suspension parts and vibration isolators. The investigation also had lead to further conclusions for future research.

7.1 Paper C 'Experimental and analytical study of secondary path variations in active engine mounts'

Hausberg, F., Scheiblegger, C., Pfeffer, P., Plöchl, M. et al., "Experimental and analytical study of secondary path variations in active engine mounts," Journal of Sound and Vibration. 2015, 340:22–38, doi: 10.1016/j.jsv.2014.11.024.

- **Model Linearization and Study on Active Hydro Mounts**
- As second author, C. Scheiblegger was responsible for model development and parameter identification for the rubber part and other components of the hydro mount. Contribution is approx. 30%.

7.2 Contribution to Research

Active engine mounts (AEMs) provide an effective solution to further improve the acoustic and vibrational comfort of passenger cars. Typically, adaptive feedforward control algorithms, e.g., the filtered-x-least-mean-squares (FxLMS) algorithm, are applied to cancel disturbing engine vibrations. These algorithms require an accurate estimate of the AEM active dynamic characteristics, also known as the secondary path, in order to guarantee control performance and stability.

Within the research context of this thesis, this article outlines how parts of the presented models can be used to study AEM behaviour. The simple basic linear hydro mount model approach presented in chapter 7 was extended with an actuator model to be able to predict AEM behaviour. The elastomer components are represented by the linearized model because the frequency range is much higher. The user tools have been improved for high frequency analyses and were used to derive model parameters of the hydro mount model and its elastomer components. The study proved that the linear model approach is capable of

mapping frequency characteristics accurately enough up to 400 Hz, confirming the model's flexibility.

The article focuses on the experimental and theoretical study of secondary path variations in AEMs. The impact of three major influences, namely non-linearity, change of preload and component temperature is experimentally analyzed. The test results are theoretically investigated with a linear AEM model that incorporates an appropriate description for elastomeric components. A special experimental set-up extends the model validation of the active dynamic characteristics to higher frequencies up to 400 Hz.

The theoretical and experimental results show that significant secondary path variations are merely observed in the frequency range of the AEM actuator's resonance frequency. These variations mainly result from the change of the component temperature. As the stability of the algorithm is primarily affected by the actuator's resonance frequency, the findings of this paper facilitate the design of AEMs with simpler adaptive feedforward algorithms. From a practical point of view, it may further be concluded that algorithmic countermeasures against instability are only necessary in the frequency range of the AEM actuator's resonance frequency.

Journal of Sound and Vibration 340 (2015) 22–38

Contents lists available at ScienceDirect

Journal of Sound and Vibration

journal homepage: www.elsevier.com/locate/jsvi

Experimental and analytical study of secondary path variations in active engine mounts

Fabian Hausberg [a,c], Christian Scheiblegger [b,d], Peter Pfeffer [b], Manfred Plöchl [c,*], Simon Hecker [e], Markus Rupp [f]

[a] Audi AG, I/EF-35, Engine/Gearbox Mountings, 85045 Ingolstadt, Germany
[b] Munich University of Applied Sciences, Department of Mechanical, Automotive and Aeronautical Engineering, Lothstr. 64, 80335 München, Germany
[c] TU Wien, Institute of Mechanics and Mechatronics, Getreidemarkt 9, 1060 Wien, Austria
[d] University of Bath, Department of Mechanical Engineering, Bath BA2 7AY, United Kingdom
[e] Munich University of Applied Sciences, Department of Electrical Engineering and Information Technology, Lothstr. 64, 80335 München, Germany
[f] TU Wien, Institute of Telecommunications, Gusshausstr. 25, 1040 Wien, Austria

ARTICLE INFO

Article history:
Received 18 April 2014
Received in revised form
10 November 2014
Accepted 17 November 2014
Handling Editor: J. Lam
Available online 17 December 2014

ABSTRACT

Active engine mounts (AEMs) provide an effective solution to further improve the acoustic and vibrational comfort of passenger cars. Typically, adaptive feedforward control algorithms, e.g., the filtered-x-least-mean-squares (FxLMS) algorithm, are applied to cancel disturbing engine vibrations. These algorithms require an accurate estimate of the AEM active dynamic characteristics, also known as the secondary path, in order to guarantee control performance and stability. This paper focuses on the experimental and theoretical study of secondary path variations in AEMs. The impact of three major influences, namely nonlinearity, change of preload and component temperature, on the AEM active dynamic characteristics is experimentally analyzed. The obtained test results are theoretically investigated with a linear AEM model which incorporates an appropriate description for elastomeric components. A special experimental set-up extends the model validation of the active dynamic characteristics to higher frequencies up to 400 Hz. The theoretical and experimental results show that significant secondary path variations are merely observed in the frequency range of the AEM actuator's resonance frequency. These variations mainly result from the change of the component temperature. As the stability of the algorithm is primarily affected by the actuator's resonance frequency, the findings of this paper facilitate the design of AEMs with simpler adaptive feedforward algorithms. From a practical point of view it may further be concluded that algorithmic countermeasures against instability are only necessary in the frequency range of the AEM actuator's resonance frequency.

1. Introduction

Due to the higher demand for fuel economy and legal restrictions to reduce emissions, an increased use of modern engine-concepts, e.g., cylinder-on-demand (COD), downsizing, turbochargers, can be observed in today's vehicles. However, in combination with lightweight car bodies, it becomes an increasingly challenging task to satisfy the noise, vibration and harshness (NVH)

* Corresponding author at: TU Wien, Institute of Mechanics and Mechatronics, Getreidemarkt 9, 1060 Wien, Austria. Tel.: +43 (1) 58801 325125.
E-mail address: manfred.ploechl@tuwien.ac.at (M. Plöchl).

http://dx.doi.org/10.1016/j.jsv.2014.11.024
0022-460X/

Nomenclature

A_A decoupler area (m^2)
A_B equivalent bulking area (m^2)
A_K cross-sectional area of fluid channel (m^2)
A_S secondary path amplitude (dimensionless)
A_T equivalent piston area of main rubber spring (m^2)
B magnetic field strength (T)
c_1, c_2 stiffness coefficients of elastomer model (N/m)
c_A actuator stiffness (N/m)
$c_{B,\mathrm{dyn}}$, $C_{B,\mathrm{dyn}}(s)$ dynamic stiffness of main rubber bulking properties (N/m)
$c_{B,1}$, $c_{B,2}$ main rubber spring bulge stiffness 1 and 2 (N/m)
$c_{T,\mathrm{dyn}}$, $C_{T,\mathrm{dyn}}(s)$ dynamic stiffness of main rubber spring (N/m)
$c_{T,1}$, $c_{T,2}$ main rubber spring stiffness 1 and 2 (N/m)
$C_{A,\mathrm{dyn}}(s)$ actuator transfer function (N/m)
$C_{K,\mathrm{dyn}}(s)$ fluid channel transfer function (N/m)
d_1, d_2 stiffness coefficients of elastomer model (N s/m)
d_A actuator damping (N s/m)
$d_{B,1}$, $d_{B,2}$ main rubber spring bulge damping 1 and 2 (N s/m)
d_K damping coefficient induced by loss of fluid flow along inertia track (N s/m)
$d_{K,\mathrm{quad}}$ quadratic damping coefficient induced by loss of fluid flow along inertia track ($N\,s^2/m^2$)
$d_{T,1}$, $d_{T,2}$ main rubber spring damping 1 and 2 (N s/m)
$d(n)$ chassis vibration (dimensionless)
$e(n)$ error signal (dimensionless)
$f_1(t)$, $F_1(s)$, $f_2(t)$, $F_2(s)$ internal forces of elastomer model (N)
$f_A(t), F_A(s)$ actuator force (N)
$f_x(t), F_x(s)$ transmitted force to the engine (N)
$f_y(t), F_y(s)$ transmitted force to the chassis (N)
$i(t)$ current (A)
j complex unit $\mathrm{j}=\sqrt{-1}$
k_M voice coil constant ($kg\,m/A\,s^2$)
l coil length (m)
l_K length of fluid channel (m)
L moving coil inductance (H)
m_A actuator mass (kg)
m_K fluid mass of inertia track (kg)
n sample number (dimensionless)
$p(n)$ impulse response of $P(z)$ (dimensionless)
$p_i(t)$ pressure inside upper fluid chamber (N/m^2)
$P(z)$ primary path (dimensionless)
$P_{xx}(s)$ passive dynamic AEM characteristics $F_x(s)/X_T(s)$ (N/m)
$P_{yx}(s)$ passive dynamic AEM characteristics $F_y(s)/X_T(s)$ (N/m)
r engine order (dimensionless)
R moving coil resistance (Ω)
s Laplace variable (dimensionless)
$s(n)$ impulse response of $S(z)$ (dimensionless)
$\hat{s}(n)$ impulse response of $\hat{S}(z)$ (dimensionless)
$s_{p,1}$, $s_{p,2}$, $s_{p,3}$ poles of $P_{xx}(s), P_{yx}(s), S_x(s), S_y(s)$ (dimensionless)
$s_{yx,1}$, $s_{yx,2}$, $s_{x,1}$, $s_{y,1}$ zeros of $P_{xx}(s), P_{yx}(s), S_x(s), S_y(s)$ (dimensionless)
$S(z)$ secondary path (dimensionless)
$S_x(s)$ active dynamic AEM characteristics $F_x(s)/U(s)$ (N/V)
$S_y(s)$ active dynamic AEM characteristics $F_y(s)/U(s)$ (N/V)
$\hat{S}(z)$ secondary path estimate (dimensionless)
t continuous time (s)
T sample time (s)
$u(n)$ control output of adaptive filter (dimensionless)
$u'(n)$ control output of adaptive filter filtered by secondary path dynamics (dimensionless)
$U(t), U(s)$ voltage (V)
$U_{\mathrm{ind}}, U_R, U_L$ induced, resistance, inductance voltage (V)
$v(n)$ engine vibration (dimensionless)
$w(n)$ complex filter weight (dimensionless)
$x_A(t), X_A(s)$ displacement of actuator mass (m)
$x(t), X(s)$ displacement of elastomer model at engine side (m)
$x_B(t), X_B(s)$ displacement of upper fluid chamber bulking area (m)
$x_K(t), X_K(s)$ displacement of fluid in inertia track (m)
$x_T(t), X_T(s)$ displacement of AEM at engine side (m)
$x(n)$ complex reference signal (dimensionless)
$x'(n)$ complex reference signal filtered by secondary path estimate (dimensionless)
$y(t), Y(s)$ displacement of AEM at chassis side (m)
z variable of z transform
$z(t), Z(s)$ internal displacement of elastomer model (m)
φ_S secondary path phase angle (deg)
$\kappa_{B,\mathrm{dyn}}$ volumetric compliance of upper fluid chamber (m^5/N)
μ adaptation step-size
ρ_f Fluid density (kg/m^3)
ω engine speed (rad/s)
AEM active engine mount
COD cylinder on demand
FIR finite impulse response
FxLMS filtered-x least mean squares
HEM hydraulic engine mount
LMS least mean squares
NVH noise, vibration and harshness
SISO single input single output

demands of the customer. While passive engine mounts reach their technical limits in solving this task, active engine mounts (AEMs) provide an effective contribution to further improve the acoustic and vibrational comfort of passenger cars.

Several concepts for AEMs have been proposed in the past [1–13]. They have all in common that a conventional passive hydraulic engine mount (HEM) is extended by an actuator, e.g., of electromagnetic or piezoelectric type, to generate active

forces in order to suppress disturbing engine vibrations. Such a commercial AEM with a moving coil actuator, whose series development is described in [14], has been studied and is shown in Fig. 1. The upper fluid chamber is bounded by the main rubber spring which supports the static engine weight. Fluid is forced through the fluid channel into the lower chamber, when the main spring is compressed. The fluid's inertia acts like a tuned mass damper and provides additional damping to counteract low frequency (< 20 Hz) engine vibrations induced by road disturbances. A diaphragm separates the upper from the lower fluid chamber. In contrast to a passive HEM, the diaphragm cannot move freely, since a moving coil actuator is attached to it. Through the control of the actuator, the pressure in the upper chamber can be influenced and therefore a force is generated in order to cancel high frequency engine disturbances (> 20 Hz).

To control an AEM, it is common practice to incorporate an accelerometer or a load cell at the chassis side to provide an error signal to an adaptive feedforward algorithm. Especially the application of finite impulse response (FIR) filters whose coefficients are adapted with the filtered-x-least-mean-squares (FxLMS) algorithm [4,15,16] or one of its variants [10,17] is widely used. These adaptive control algorithms require an estimate of the plant response, to act as an internal plant model, for their correct operation. The so-called secondary path $S(z)$ includes the entire response between the output of the control signal and the measurement of the error signal [18]. However, model errors, resulting from secondary path changes during the operation of the AEM, degrade the performance of the FxLMS algorithm or even may result in its instability. In this case, either an online system identification scheme [15,19] or a method to increase the algorithm's robustness to model errors [18,20–22] must be employed. While the first may be computationally demanding and often requires the injection of a significant amount of identification noise, the latter implies a certain performance degradation.

In this context, and in order to clarify if any online identification or robustness schemes are necessary, this research mainly focuses on the experimental and analytical study of secondary path variations in AEMs. The FxLMS algorithm and the importance of the secondary path estimate for its application are reviewed in Section 2. Next, a linear analytical AEM model with an appropriate description for elastomeric components is developed and experimentally verified in Section 3. In contrast to existing work on AEM models [5–8], in Section 4, the experimental validation of the engine mount's secondary path is extended to higher frequencies up to 400 Hz. In Section 5, the assumption of the secondary path's linearity, which is a requirement for the application of the FxLMS algorithm, and the impact of the two major influences, temperature as well as preload, are investigated. The secondary path changes that are observed in the experiments are interpreted with the aid of the developed AEM model.

It was found that significant changes in the secondary path are limited to the frequency range of the engine mount actuator's resonance frequency. Hence, online identification or robustness measures may be omitted, if the AEM is designed such that the resonance frequency is shifted outside of the adaptive algorithm's frequency range of operation.

2. Stability of the FxLMS algorithm

A widespread method for the control of AEMs is the application of the Narrowband-FxLMS algorithm. While its foundation, the LMS algorithm, was already proposed in 1960 [23], it has been Morgan [24], who suggested the FxLMS algorithm for applications with an additional filter in the cancelation path of the adaptive filter. This section gives a short introduction of the FxLMS algorithm in order to provide a better understanding of the subsequent sections.

Fig. 2 shows a computationally efficient complex variant of the Narrowband-FxLMS algorithm. The vibration $d(n)$ at the chassis, which is to be canceled, results from the engine vibration $v(n)$ transmitted through the passive dynamic characteristics P

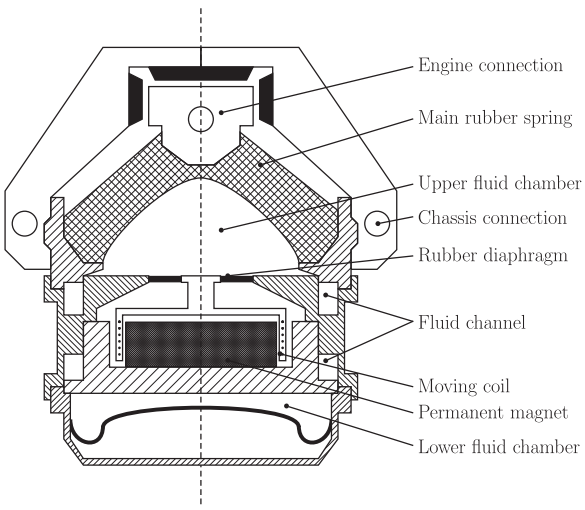

Fig. 1. Schematic diagram of an active engine mount.

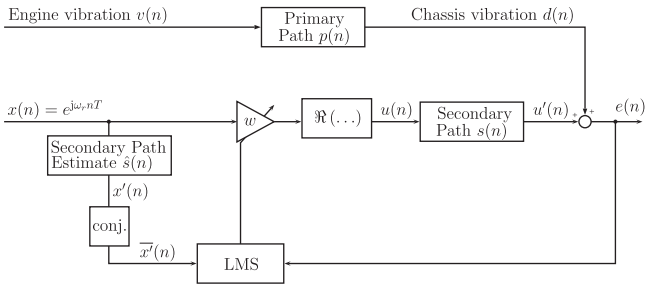

Fig. 2. Block diagram of the complex Narrowband-FxLMS algorithm.

(z) of the AEM represented by its impulse response $p(n)$. The error signal $e(n)$ measured at the chassis side is given by

$$e(n) = d(n) + s(n) * u(n) = d(n) + u'(n) \tag{1}$$

where $u(n)$ is the control output of the adaptive filter and $s(n)$ is the impulse response of the secondary path $S(z)$, representing the active dynamic characteristics of the AEM.

The engine speed ω obtained from a crankshaft tachometer multiplied by the engine order r, to be canceled, generates a complex reference signal $x(n)$. In order to compensate for the dynamics of the secondary path $S(z)$, the complex reference signal has to be filtered with a secondary path estimate $\hat{S}(z)$. It is common practice to model the estimate of the secondary path impulse $\hat{s}(n)$ response as an FIR filter. However, in order to reduce the computational load for generating the filtered reference signal $x'(n)$, the estimated secondary path is taken into account by its amplitude $A_S(r\omega)$ and phase angle $\varphi_S(r\omega)$. In this case the complex filtered reference signal is given by

$$x'(n) = A_S(r\omega) e^{j\varphi_S(r\omega)} e^{jr\omega nT} \tag{2}$$

According to Widrow [25], the complex conjugate $\overline{x}'(n)$ of the reference signal $x'(n)$ has to be applied in the weight update equation of a complex-valued LMS algorithm. Therefore, the complex filter weight $w(n)$ is updated according to

$$w(n+1) = w(n) + \mu \overline{x}'(n) e(n), \tag{3}$$

in order to minimize the mean square of $e(n)$ in Eq. (1). The convergence rate and stability of the algorithm are determined by the step-size parameter μ. Finally, the control signal $u(n)$ is obtained by multiplying the complex filter weight with the complex reference signal and taking the real part of the signal:

$$u(n) = \mathcal{R}\{w(n)x(n)\}. \tag{4}$$

The secondary path estimate $\hat{S}(z)$ is of significant importance in the application of the FxLMS algorithm. Modeling errors, resulting from changes during the operation of the AEM, may lead to severe performance degradation or even instability. It has been shown in several studies [24,26–29] that for the cancelation of narrowband signals in single-input–single-output (SISO) systems, the phase error between the secondary path $S(z)$ and its estimate $\hat{S}(z)$ must not exceed 90°. Otherwise, the algorithm may become unstable. In addition, many active noise and vibration control systems perform the adaptive filtering operation in the time domain. In this case, the stability bound depends on the ratio between the sampling rate and the input frequency as well on the inherent time delay in the active vibration control system. Depending on the chosen step size μ, the algorithm may become unstable for phase errors well below 90° [30].

3. Analytical model

3.1. Elastomer model

The main rubber spring is a central part of an AEM. Its stiffness, damping and bulking properties contribute substantially to the engine mount's dynamic transfer function. Carbon black filled rubber components have an amplitude- and frequency-dependent transfer behavior [31]. However, in AEMs, the main rubber spring is often modeled with a linear spring element [5,6] or a damper in parallel to a spring element (Kelvin–Voigt Model) [7,8]. Such models offer good agreement for dynamic stiffness over frequency but the damping characteristics are only a rough estimation [32]. To overcome this problem, in this paper, the main rubber spring and its bulking properties are each modeled with two dampers and one spring in parallel to another spring as shown in Fig. 3. This approach has already been applied in [32-35] as part of a nonlinear elastomer model in conventional HEMs. The underlying model has been developed to map amplitude-dependent characteristics of elastomeric materials. Since the experiments in this paper are limited to small amplitudes, the amplitude-dependency is neglected in order to keep the model linear.

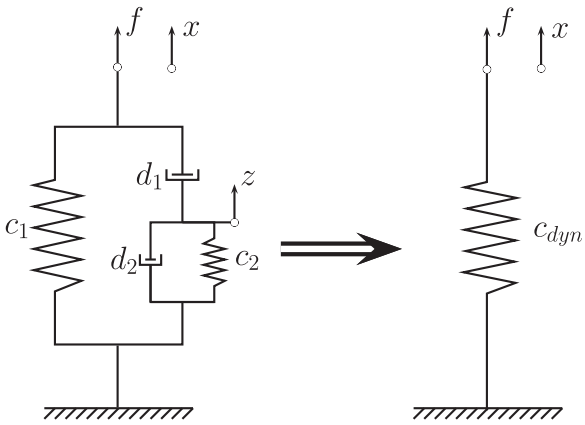

Fig. 3. Linear dynamic model for AEM elastomer components.

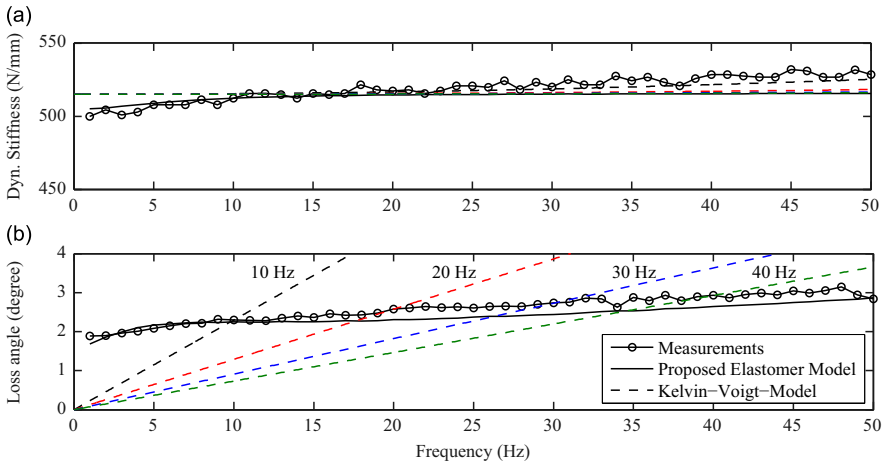

Fig. 4. Simulated and measured dynamic characteristics of a conventional elastomeric mount. (a) Dynamic stiffness; (b) loss angle. *Key*: Measurements (-o-); simulation of proposed elastomer model (—); simulation of Kelvin–Voigt Model for different layout frequencies (- -).

Expressions for the force f_1 and f_2 in the left and right parts, respectively, of the elastomer model in Fig. 3 are written as follows:

$$f_1(t) = c_1 x(t), \tag{5}$$

$$f_2(t) = c_2 z(t) + d_2 \dot{z}(t) = d_1(\dot{x}(t) - \dot{z}(t)). \tag{6}$$

The summation of Eqs. (5) and (6) yields

$$f(t) = f_1(t) + f_2(t) = c_1 x(t) + d_1(\dot{x}(t) - \dot{z}(t)). \tag{7}$$

Finally, the transfer function of the elastomer model can be derived from Eqs. (6) and (7) in the Laplace domain as follows:

$$C_{\mathrm{dyn}}(s) = \frac{F(s)}{X(s)} = c_1 + \frac{d_1 c_2 s + d_1 d_2 s^2}{c_2 + (d_1 + d_2)s}. \tag{8}$$

Fig. 4 shows the comparison of the measured dynamic stiffness and loss angle of a conventional elastomeric mount to the simulated transfer behavior of a Kelvin–Voigt Model and the model of Fig. 3. While both models show a good agreement of the mount's dynamic stiffness, only the proposed elastomer model resembles the phase angle of the measurement in the whole frequency range. In contrast, the Kelvin–Voigt Model maps the measured loss angle solely at one design frequency [32].

3.2. AEM model

The analytical description of the transfer behavior of conventional, passive HEMs has been subject of intensive research for several decades. Various linear and nonlinear models have been developed [36–41]. In contrast, there exist only a limited number of publications regarding the modeling of AEMs [5–8]. Fig. 5(a) illustrates the lumped parameter linear model used

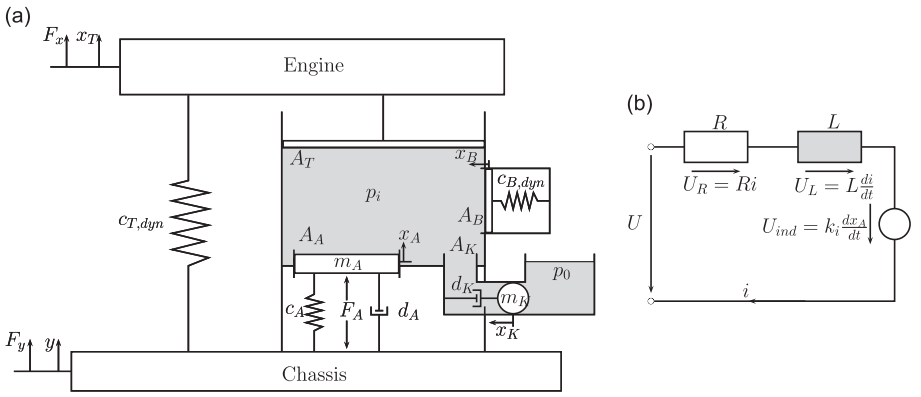

Fig. 5. Linear lumped parameter model of AEM. (a) Mechanical model; (b) electrical circuit of moving coil actuator.

in this paper to derive the transfer behavior of an AEM. It can be regarded as an extension of the model developed by Lee and Lee [6], who introduced three major concepts. First, the actuator dynamics are taken into account in order to properly explain the engine mount's passive and active characteristics. Second, the transmitted forces to the chassis and the engine are assumed to be unequal, since the inertia effects of the actuator inside the mount are not negligibly small. Finally, the actuator runner's dynamic characteristics are represented in terms of force rather than displacement.

This paper incorporates the elastomer model of Section 3.1 into the model of Lee and Lee [6] to express the main rubber spring's dynamic properties $c_{T,\mathrm{dyn}}$. The experimental validation is extended to higher frequencies to clearly indicate the effect of the actuator's dynamics on the AEM's secondary path. In contrast to the widespread use of the volumetric compliance, the bulking properties of the upper fluid chamber are explicitly expressed by the degree of freedom $x_B(t)$, the bulking area A_B and another elastomer model $c_{B,\mathrm{dyn}}$. However, these are straightforwardly transferred to the volumetric compliance as follows:

$$\kappa_{B,\mathrm{dyn}} = \frac{A_B^2}{c_{B,\mathrm{dyn}}}. \tag{9}$$

The equations for the system shown in Fig. 5(a) are derived as follows. The pressure $p_i(t)$ in the upper fluid chamber is in equilibrium with the bulking properties of the main rubber spring:

$$-p_i(t)A_B = c_{B,\mathrm{dyn}}x_B(t). \tag{10}$$

The volumetric stiffness of the lower fluid chamber is neglected, since it is considerably smaller than that of the upper fluid chamber [42]. Therefore, it is assumed that the pressure in the lower chamber is equal to the ambient pressure [36,37]. Newton's law for the fluid channel which connects the upper chamber to the lower chamber becomes

$$m_K\ddot{x}_K(t) + d_K\dot{x}_K(t) = -p_i(t)A_K. \tag{11}$$

In a first step, the fluid damping d_K is assumed to be linearly dependent on the flow velocity $\dot{x}_K$. However, it will be shown in Section 5.1 that this assumption is not valid for different excitation amplitudes. The equivalent mass m_K of the fluid within the fluid channel can be obtained from the channel length l_K, the cross sectional area A_K and the fluid's density ρ_f:

$$m_K = \rho_f A_K l_K. \tag{12}$$

According to [6], it is assumed that the fluid channel is connected to the absolute reference frame rather than to the chassis. The fluid's friction force is not transmitted vertically to the chassis, since the fluid flows in the peripheral direction. Otherwise, the fluid's inertia would cause a difference between the force transmitted to the chassis and the force transmitted to the engine. However, it has been experimentally shown in [43] that the fluid's inertia does not contribute to any differences between these two forces.

The fluid is considered to be incompressible and thus the continuity equation for the upper chamber becomes

$$A_A\dot{x}_A(t) + A_K\dot{x}_K(t) + A_B\dot{x}_B(t) = A_T\dot{x}_T(t), \tag{13}$$

where A_A is the cross sectional area of the diaphragm, x_A is the actuator displacement, A_T is the equivalent piston area of the main rubber spring and x_T is the displacement of the AEM at the engine side. The actuator dynamics are taken into account as a mass–spring–damper system with mass m_A, spring constant c_A and damping coefficient d_A. The actuator's force f_A is acting on the cross sectional area A_A of the diaphragm. The application of Newton's law can be written as

$$m_A\ddot{x}_A(t) + d_A\dot{x}_A(t) + c_Ax_A(t) = f_A(t) - p_i(t)A_A. \tag{14}$$

In Eq. (14), and the following derivations, it is assumed that the chassis-side degree of freedom $y(t)$ is fixed. This simplification is valid, because the AEM is clamped at this side during the experimental validation in Section 4.

In contrast to [6], the AEM of this research incorporates a moving coil actuator, which employs the Lorentz–Force Principle. The force $f_A(t)$ of a current carrying conductor of length l in a magnetic field is proportional to the field strength B

and the current $i(t)$:

$$f_A(t) = Bli(t) = k_M i(t), \tag{15}$$

where k_M is the voice coil constant. Fig. 5(b) shows the electrical circuit of the moving coil actuator. The resistance R and the inductance L of the coil are assumed to be linear and frequency independent. In addition, the coil's movement changes its magnetic field and therefore a voltage $U_{\mathrm{ind}}(t)$ is induced. According to the second law of Kirchhoff, it follows

$$U(t) = U_R(t) + U_L(t) + U_{\mathrm{ind}}(t) = Ri(t) + L\frac{\mathrm{d}i(t)}{\mathrm{d}t} + k_M \dot{x}_A(t), \tag{16}$$

where $U(t)$ is the input voltage, $U_R(t)$ is the voltage in the coil resistance and $U_L(t)$ is the voltage in the coil inductance. Finally, the force transmitted to the engine $f_x(t)$ and the force transmitted to the chassis $f_y(t)$ can be expressed as

$$f_x(t) = -c_{T,\mathrm{dyn}} x_T + p_i(t) A_T \tag{17}$$

$$\begin{aligned} f_y(t) &= c_{T,\mathrm{dyn}} x_T - p_i(t)(A_T - A_A) + c_A x_A(t) + d_A \dot{x}_A(t) - f_A(t) \\ &= c_{T,\mathrm{dyn}} x_T - p_i(t) A_T - m_A \ddot{x}_A, \end{aligned} \tag{18}$$

where the main rubber spring's dynamic characteristics are governed by $c_{T,\mathrm{dyn}}$. The comparison of Eqs. (17) and (18) already shows that due to the actuator's inertia the forces $f_x(t)$ and $f_y(t)$ are unequal.

From Eqs. (10)–(18) expressed in the Laplace domain, two transfer functions

$$P_{xx}(s) = \frac{F_x(s)}{X_T(s)} = -C_{T,\mathrm{dyn}}(s) - \frac{A_T^2}{\dfrac{A_B^2}{C_{B,\mathrm{dyn}}(s)} + \dfrac{A_K^2}{C_{K,\mathrm{dyn}}(s)} + \dfrac{A_A^2}{C_{A,\mathrm{dyn}}(s)}}, \tag{19}$$

$$P_{yx}(s) = \frac{F_y(s)}{X_T(s)} = C_{T,\mathrm{dyn}}(s) + \frac{A_T^2 - \dfrac{m_A A_A A_T}{C_{A,\mathrm{dyn}}(s)} s^2}{\dfrac{A_B^2}{C_{B,\mathrm{dyn}}(s)} + \dfrac{A_K^2}{C_{K,\mathrm{dyn}}(s)} + \dfrac{A_A^2}{C_{A,\mathrm{dyn}}(s)}}, \tag{20}$$

describing the passive dynamic characteristics of the AEM, and two transfer functions

$$S_x(s) = \frac{F_x(s)}{U(s)} = \frac{k_M A_A A_T}{C_{A,\mathrm{dyn}}(s)(R + Ls)\left(\dfrac{A_B^2}{C_{B,\mathrm{dyn}}(s)} + \dfrac{A_K^2}{C_{K,\mathrm{dyn}}(s)} + \dfrac{A_A^2}{C_{A,\mathrm{dyn}}(s)}\right)}, \tag{21}$$

$$S_y(s) = \frac{F_y(s)}{U(s)} = \frac{-k_M\left(A_A A_T + m_A s^2\left(\dfrac{A_B^2}{C_{B,\mathrm{dyn}}(s)} + \dfrac{A_K^2}{C_{K,\mathrm{dyn}}(s)}\right)\right)}{C_{A,\mathrm{dyn}}(s)(R + Ls)\left(\dfrac{A_B^2}{C_{B,\mathrm{dyn}}(s)} + \dfrac{A_K^2}{C_{K,\mathrm{dyn}}(s)} + \dfrac{A_A^2}{C_{A,\mathrm{dyn}}(s)}\right)}, \tag{22}$$

describing the active dynamic characteristics of the AEM are obtained. In Eqs. (19)–(22), the following operators have been introduced:

$$C_{A,\mathrm{dyn}}(s) = m_A s^2 + \left(d_A + \frac{k_M^2}{R + Ls}\right) s + c_A, \tag{23}$$

$$C_{K,\mathrm{dyn}}(s) = m_K s^2 + d_K s, \tag{24}$$

$$C_{T,\mathrm{dyn}}(s) = c_{T,1} + \frac{d_{T,1} c_{T,2} s + d_{T,1} d_{T,2} s^2}{c_{T,2} + (d_{T,1} + d_{T,2}) s}, \tag{25}$$

$$C_{B,\mathrm{dyn}}(s) = c_{B,1} + \frac{d_{B,1} c_{B,2} s + d_{B,1} d_{B,2} s^2}{c_{B,2} + (d_{B,1} + d_{B,2}) s}. \tag{26}$$

4. Experimental validation

4.1. Test rigs

The experimental validation of the analytical model, that has been derived in the preceding section, is carried out with two different test rigs. A conventional servo-hydraulic test rig, whose layout is shown in Fig. 6, is employed for the measurement of the passive dynamic characteristics P_{yx}. While the upper part of the engine mount is excited with a

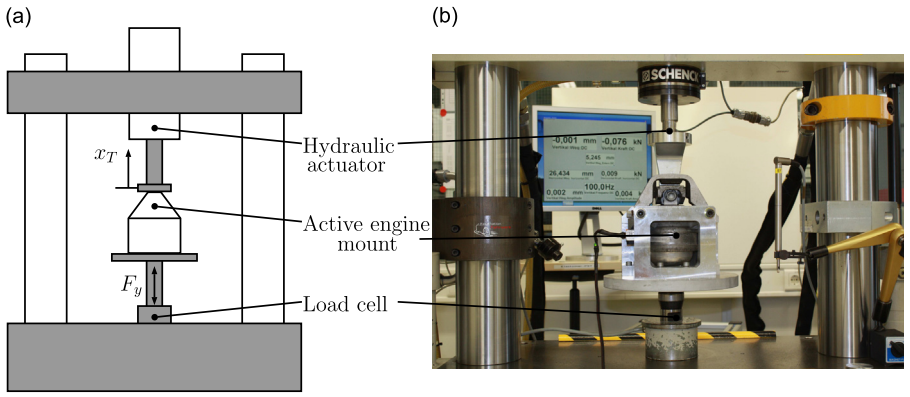

Fig. 6. Conventional servo-hydraulic test rig for measurement of $P_{yx}(s)$. (a) Schematic diagram; (b) experimental setup.

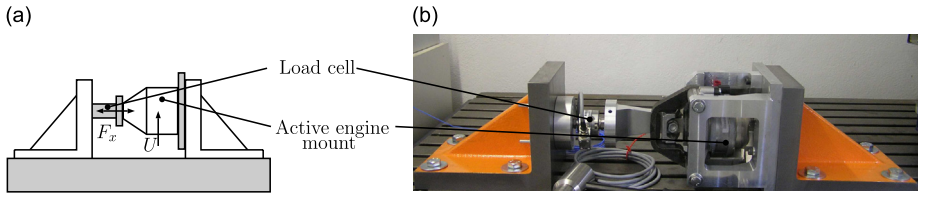

Fig. 7. AEM test rig for measurement of $S_x(s)$. (a) Schematic diagram; (b) experimental setup.

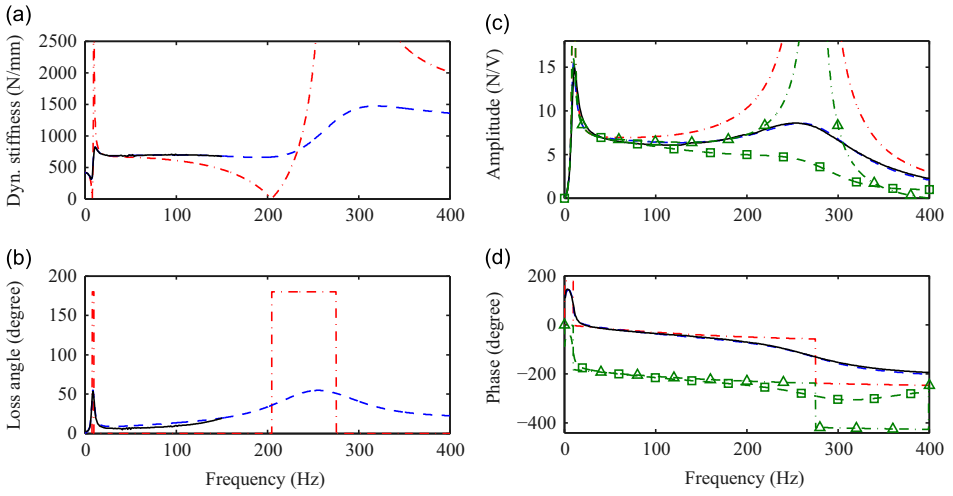

Fig. 8. Experimental validation of analytical AEM model. (a) Amplitude of AEM passive dynamic characteristics $P_{yx}(s)$; (b) phase of AEM passive dynamic characteristics $P_{yx}(s)$. *Key*: Measurement (—); simulation of damped model (- -); simulation of undamped model (-·-). (c) Amplitude of AEM active dynamic characteristics $S_x(s)$ and $S_y(s)$; (d) phase of AEM active dynamic characteristics $S_x(s)$ and $S_y(s)$. *Key*: Measurement of $S_x(s)$ (—); simulation of damped model of $S_x(s)$ (- -); simulation of undamped model of $S_x(s)$ (-·-); simulation of damped model of $S_y(s)$ (-□-), Simulation of undamped model of $S_y(s)$ (-Δ-).

sinusoidal displacement of predefined amplitude of 0.1 mm, a load cell measures the reaction force at the engine mount's chassis side. Both signals are postprocessed in order to obtain the amplitude and phase angle of Eq. (20), commonly referred to as dynamic stiffness and loss angle, respectively. The maximum test frequency of this test rig is limited to 150 Hz, due to the restricted dynamics of the hydraulic exciter and structural resonances in the higher frequency range.

Since this work focuses on the analytical and experimental study of the engine mount's active transfer behavior, the test rig shown in Fig. 7 has been developed. The AEM and a load cell are clamped between two massive L-shaped steel plates with a preload corresponding to the proportional engine weight. A sinusoidal control signal is applied to the engine mount's actuator. Due to the requirement of a compact stiff design, the force measurement is restricted to the engine side. Thereby, the test rig allows the experimental validation of the engine mount's active dynamic characteristics S_x of Eq. (21) up to a maximum frequency of 400 Hz. The transfer function S_y is obtained by simulation, which will be explained in the next sections.

4.2. Experimental results

Fig. 8 shows the comparison of the experimental and analytical results for the passive and active dynamic characteristics. In addition, the result of an undamped simulation model is shown in each diagram. These will be further discussed in Section 4.3 to identify characteristic poles and zeros in the AEM's transfer behavior. The simulated curves of the dynamic stiffness and the loss angle in Fig. 8(a) and (b) are in good agreement with the measurement results up to the maximum test frequency of 150 Hz. Furthermore, Fig. 8(c) and (d) shows that the developed analytical model is capable to describe the active dynamic characteristics $S_x(s)$ of the engine mount up to a frequency of 400 Hz. Table 1 summarizes the parameters that have been experimentally identified in order to obtain the simulation results of this section. The geometric parameters of the AEM have been determined by means of a part dismantling. Afterwards, the remaining parameters have been identified by solving a nonlinear least-squares curve fitting problem (based on the Trust-Region-Reflective Algorithm from [44]) between the analytical and the experimental results within reasonable limits.

4.3. Characteristic poles and zeros

In this section, characteristic poles and zeros in the active and passive dynamic characteristics S_x, S_y and P_{yx} are identified. As will be shown in Section 5, these are of great importance in the experimental analysis of the secondary path variations. In order to simplify the following derivation, an undamped simulation model without any effects of mutual inductance is considered and Eqs. (23)–(26) become

$$C_{A,\mathrm{dyn}}(s) = m_A s^2 + c_A, \tag{27}$$

$$C_{K,\mathrm{dyn}}(s) = m_K s^2, \tag{28}$$

$$C_{T,\mathrm{dyn}}(s) = c_{T,1}, \tag{29}$$

$$C_{B,\mathrm{dyn}}(s) = c_{B,1}. \tag{30}$$

An approximate solution for the characteristic poles and zeros is obtained under further simplifying assumptions. First, the transfer behavior of the AEM is dominated in the lower frequency range (< 25 Hz) by the dynamics of the fluid channel. Hence, the actuator mass m_A is neglected to calculate the poles and zeros in this frequency range. Second, in the frequency range above 25 Hz the fluid channel is hydraulically closed and all corresponding terms are omitted in order to obtain analytical expressions for the poles and zeros. With these assumptions, and following the same derivation from Section 3.2 to obtain Eqs. (20) and (21) result in

$$P_{yx,\mathrm{lowfreq}}(s) = \frac{m_K\left(A_A^2 c_{B,1} c_{T,1} + A_B^2 c_A c_{T,1} + A_T^2 c_A c_{B,1}\right)s^2 + A_K^2 c_A c_{B,1} c_{T,1}}{m_K\left(A_A^2 c_{B,1} + A_B^2 c_A\right)s^2 + A_K^2 c_A c_{B,1}} \tag{31}$$

Table 1
Experimentally identified parameters of the analytical AEM model.

Symbol	Name	Value	Unit
$c_{T,1}$	Main rubber spring stiffness 1	418.1	N/mm
$c_{T,2}$	Main rubber spring stiffness 2	48.1	N/mm
$d_{T,1}$	Main rubber spring damping 1	268.7	N s/m
$d_{T,2}$	Main rubber spring damping 2	11.1	N s/m
$c_{B,1}$	Main rubber spring bulge stiffness 1	180.4	N/mm
$c_{B,2}$	Main rubber spring bulge stiffness 2	272.9	N/mm
$d_{B,1}$	Main rubber spring bulge damping 1	1525.7	N s/m
$d_{B,2}$	Main rubber spring bulge damping 2	62.9	N s/m
A_T	Equivalent piston area of main rubber spring	3872.4	mm^2
A_B	Equivalent bulking area	2362.2	mm^2
A_A	Decoupler area	1683.9	mm^2
A_K	Cross-sectional area of fluid channel	92.5	mm^2
l_K	Length of fluid channel	328.8	mm
d_K	Fluid damping	0.4	N s/m
ρ_f	Fluid density	1000	kg/m^3
c_A	Actuator stiffness	53.5	N/mm
d_A	Actuator damping	19.5	N s/m
m_A	Actuator mass	105.8	g
R	Moving coil resistance	3.7	Ω
L	Moving coil inductance	3.5	mH
k_M	Voice coil constant	14.0	kg m/As^2

and

$$S_{x,\mathrm{lowfreq}}(s) = -S_{y,\mathrm{lowfreq}}(s) = \frac{k_M A_A A_T c_{B,1} m_K s^2}{(R+Ls)\left(m_K\left(A_A^2 c_{B,1} + A_B^2 c_A\right)s^2 + A_K^2 c_A c_{B,1}\right)} \tag{32}$$

as simplified transfer functions for the lower frequency range. Likewise, neglecting the fluid channel dynamics leads to

$$P_{yx,\mathrm{highfreq}}(s) = \frac{m_A\left(A_B^2 c_{T,1} + c_{B,1}\left(A_T^2 - A_T A_A\right)\right)s^2 + A_B^2 c_A c_{T,1} + A_A^2 c_{B,1} c_{T,1} + A_T^2 c_A c_{B,1}}{m_A A_B^2 s^2 + A_A^2 c_{B,1} + A_B^2 c_A}, \tag{33}$$

$$S_{x,\mathrm{highfreq}}(s) = \frac{k_M A_A A_T c_{B,1}}{(R+Ls)\left(m_A A_B^2 s^2 + A_A^2 c_{B,1} + A_B^2 c_A\right)} \tag{34}$$

and

$$S_{y,\mathrm{highfreq}}(s) = -\frac{k_M\left(m_A A_B^2 s^2 + A_A A_T c_{B,1}\right)}{(R+Ls)\left(m_A A_B^2 s^2 + A_A^2 c_{B,1} + A_B^2 c_A\right)} \tag{35}$$

as simplified transfer functions for the higher frequency range.

With these simplified transfer functions, two complex conjugate poles are analytically identified:

$$s_{p,1}^2 = -\frac{A_K^2}{\left(\frac{A_B^2}{c_{B,1}} + \frac{A_A^2}{c_A}\right)m_K} \tag{36}$$

$$s_{p,2}^2 = -\frac{\left(\frac{A_B^2}{c_{B,1}} + \frac{A_A^2}{c_A}\right)c_A}{\frac{A_B^2}{c_{B,1}} m_A}. \tag{37}$$

In addition, the simplified transfer functions in Eqs. (32), (34) and (35), representing the active dynamic characteristics, each possesses another single pole at

$$s_{p,3} = -\frac{R}{L}, \tag{38}$$

resulting from the electrical circuit of the engine mount's actuator.

The complex conjugate poles in Eqs. (36) and (37) correspond to the natural frequencies of the AEM. The first pole $s_{p,1}$ is dominated by the vibration system consisting of the mass in the fluid channel and the elasticities of the upper chamber. This frequency is referred to as the fluid channel's resonance frequency. The second pole $s_{p,2}$ can be associated with the vibration system composed of the actuator's mass and the elasticities of the upper chamber. It is referred to as the actuator's resonance frequency. Finally, the zeros of Eqs. (31)–(35) are obtained by setting their numerator to zero. This results in

$$s_{yx,1}^2 = -\frac{A_K^2}{\left(\frac{A_B^2}{c_{B,1}} + \frac{A_A^2}{c_A} + \frac{A_T^2}{c_{T,1}}\right)m_K} \tag{39}$$

$$s_{yx,2}^2 = -\frac{\left(\frac{A_B^2}{c_{B,1}} + \frac{A_A^2}{c_A} + \frac{A_T^2}{c_{T,1}}\right)c_A}{\left(\frac{A_B^2}{c_{B,1}} + \frac{A_T^2 - A_A A_T}{c_{T,1}}\right)m_A} \tag{40}$$

for the passive dynamic characteristics $P_{yx,\mathrm{lowfreq}}$ and $P_{yx,\mathrm{highfreq}}$ and

$$s_{x,1}^2 = 0 \tag{41}$$

for the active dynamic characteristics $S_{x,\mathrm{lowfreq}}$ and $S_{y,\mathrm{lowfreq}}$. In addition, $S_{y,\mathrm{highfreq}}$ possesses a zero at

$$s_{y,1}^2 = -\frac{A_A A_T c_{B,1}}{A_B^2 m_A}. \tag{42}$$

The corresponding simulation results of Eqs. (20)–(22) with neglection of all damping parameters are shown in Fig. 8 as dot-dashed curves. A closer look at Fig. 8(a) and (b) shows that the passive dynamic characteristics are dominated in the lower frequency (<25 Hz) by the close sequence of the complex conjugate zero $s_{yx,1}$ and the complex conjugate pole $s_{p,1}$. It is interesting to note that the local maximum in the loss angle, which is an important measure for the engine mount's

capability to dampen low frequency eigenmodes of the engine, results from the corresponding sequence of a $+180^\circ$ and a -180° phase shift. In the frequency range above the fluid channel's resonance frequency, an increase in the engine mount's dynamic stiffness can be observed. Since the fluid channel is hydraulically closed, the fluid cannot flow from the working chamber into the compensation chamber. Due to the actuator's dynamics, the passive dynamic characteristics of the AEM significantly differ from those of a conventional, passive HEM in the higher frequency range. Between the second complex conjugate zero $s_{yx,2}$ and the second complex conjugate pole $s_{p,2}$ another increase in the dynamic stiffness as well as a phase shift of $+180^\circ$ and -180° can be observed. The increase in dynamic stiffness can be explained by the fact that the actuator's mass m_A is at rest above its resonance frequency and thus the stiffness c_A is ineffective.

As expected, Fig. 8(c) and (d) shows that the amplitudes of the active dynamic characteristics S_x and S_y start at the origin and the phases show a shift of $+180^\circ$ due to the zeros of $s_{x,1}$. In the frequency range of the first pole $s_{p,1}$ the actuator's excitation frequency coincides with the resonance frequency of the fluid channel and the amplitude curves reach a first local maximum. The phase angles show a continuous decrease due to the pole $s_{p,3}$ of the electric circuit. Another local maximum in the amplitudes of the active transfer functions can be observed at the frequency of the second pole $s_{p,2}$. The slope of the corresponding -180° phase shift is affected by the damping properties. In contrast to S_x, the transfer function S_y possesses another zero, Eq. (42), which can be observed by the phase shift of 180° at the end of the corresponding phase curve.

5. Experimental analysis of secondary path variations

In the previous section, an analytical model of an AEM has been developed, which is capable to describe the passive and active transfer behavior in the frequency range of interest. This model will be applied in this section to analytically and experimentally investigate the impact of environmental influences occurring in the vehicle on the engine mount's active transfer function. First, it is clarified if an AEM can be treated as a linear device with respect to its secondary path. Afterwards, the effects of the two major influences ambient temperature and change of preload are discussed.

5.1. Nonlinearity

The application of adaptive algorithms such as the FxLMS-algorithm in active vibration control requires a sufficiently linear secondary path. Small nonlinearities might already adversely affect the achievable vibration compensation [45]. However, several studies have shown that conventional, passive HEMs exhibit a highly nonlinear, amplitude-dependent behavior, due to the elastomer material, the fluid channel's dynamics and the characteristics of the decoupling membrane [37,38,46–53]. Hence, this section analyses if it is a valid assumption to treat an AEM's secondary path as being linear.

The active dynamic characteristics $S_x(s)$ are measured for two different input voltages. Since for this experiment no equivalent transfer function $P_{yx}(s)$ exists, in addition, the transfer behavior of the actuator alone has been determined. Therefore, the actuator has been removed from the AEM and the transfer function between the input voltage and an accelerometer positioned at the actuator's diaphragm is measured. The test results as well as the corresponding simulation results are shown in Fig. 9. The active dynamic characteristics $S_x(s)$ and $S_y(s)$ exhibit a slight amplitude-dependent nonlinearity which is particularly pronounced in the area of the characteristic poles that have been derived in Section 4.3. At the fluid channel's resonance frequency, the transfer function amplitude decreases with increasing input voltage. Therefore, the previously chosen linear approach to model the fluid dynamics in Eq. (11) is extended by a nonlinear damping

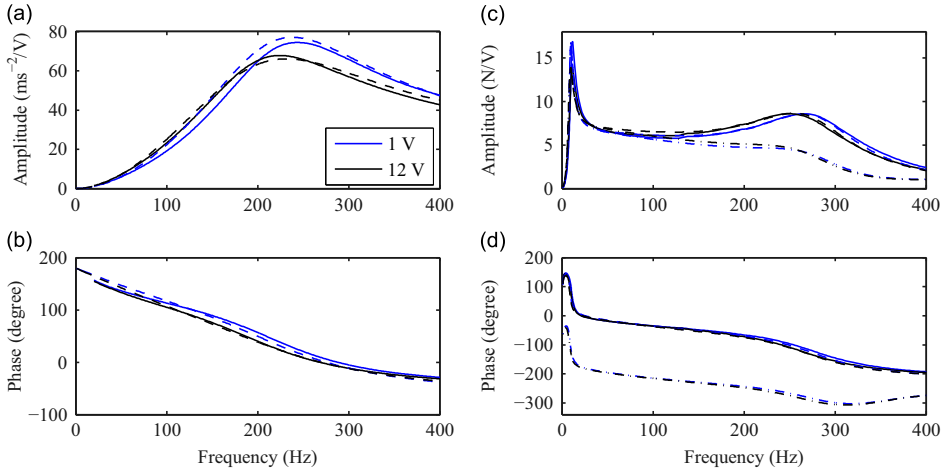

Fig. 9. AEM transfer functions for different input voltages. (a) Amplitude of AEM actuator transfer function; (b) phase of AEM actuator transfer function. *Key*: Measurement (—); simulation (- -). (c) Amplitude of AEM active dynamic characteristics $S_x(s)$ and $S_y(s)$; (d) phase of AEM active dynamic characteristics $S_x(s)$ and $S_y(s)$. *Key*: Measurement of $S_x(s)$ (—); simulation of $S_x(s)$ (- -); simulation of $S_y(s)$ (-··-).

parameter $d_{K,\mathrm{quad}}$ to

$$m_K\ddot{x}_K(t)+d_K\dot{x}_K(t)+d_{K,\mathrm{quad}}|\dot{x}_K(t)|\dot{x}_K(t)=-p_i(t)A_K. \tag{43}$$

A similar extension has been used before in [39] for nonlinear modeling of a conventional HEM. While the linear parameter d_K covers the fluid damping for the laminar flow, the turbulent flow is covered by the nonlinear parameter $d_{K,\mathrm{quad}}$. The very good agreement between the simulation results and the experimental results in Fig. 9 has been obtained by setting the parameters to d_K and $d_{K,\mathrm{quad}}$ to 0.35 N s/m and 0.1 N s^2/m^2, respectively.

Besides the described amplitude-dependent nonlinearity in the area of the fluid channel's resonance frequency, another distinct nonlinearity can be observed at the resonance frequency of the actuator. The resonance frequency is shifted to lower frequencies with increasing input voltage. An equivalent behavior can be observed in the transfer function of the engine mount's actuator. A possible explanation may be given by the observation of the analytically identified pole location in Eq. (37). Since the mass m_A of the actuator can be assumed to be constant, only the parameters c_A and d_A remain as possible causes for the described nonlinearity. These parameters describe the stiffness and damping properties of the actuator's elastomer diaphragm. It has been shown in [31] that the dynamic stiffness and the loss angle of carbon black-filled elastomers have a strong amplitude-dependent behavior. While the dynamic stiffness decreases with increasing excitation amplitude, the loss angle initially rises steeply until it reaches a maximum to slightly decrease afterwards [31,54]. In this study, this phenomenon commonly known as the *Payne Effect* [31] is taken into account by incorporation of amplitude-dependent parameters c_A and d_A whose resulting dynamic stiffness and loss angle are shown in Fig. 10. Due to lack of material test results the qualitative characteristics have been adapted to the results of [54]. Fig. 9 shows that the extended nonlinear simulation model is in good agreement with the experimental results.

Finally, it can be summarized that the AEM shows a slight amplitude-dependent nonlinearity which is more pronounced in the areas of its characteristic resonance frequencies. However, the nonlinearity in the area of the fluid channel's resonance is not relevant for the application of adaptive feedforward control, since the algorithm's operating frequency is

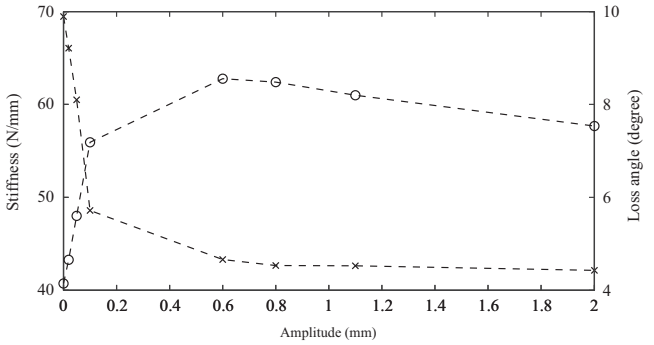

Fig. 10. Characteristics of amplitude-dependent stiffness (- × -) and loss angle (-o-) of elastomer actuator diaphragm.

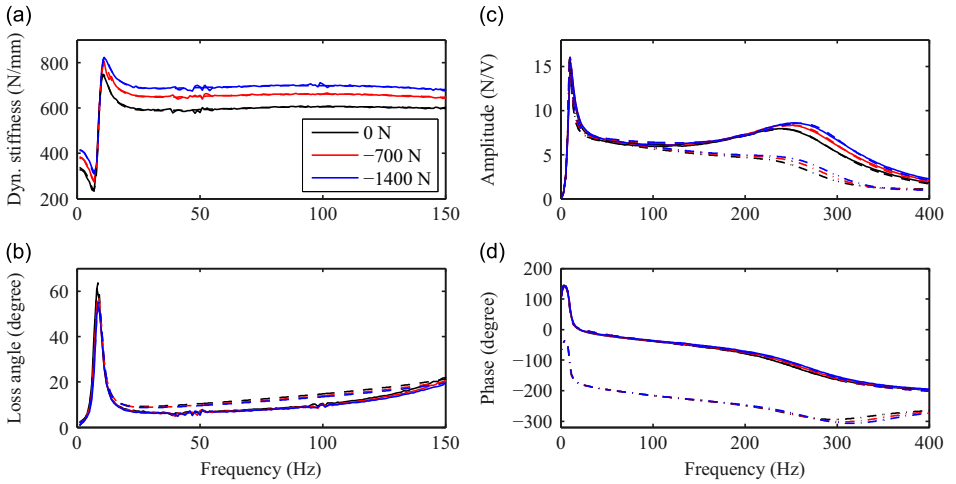

Fig. 11. AEM transfer functions for different preloads. (a) Amplitude of AEM passive dynamic characteristics $P_{yx}(s)$; (b) phase of AEM passive dynamic characteristics $P_{yx}(s)$. *Key*: Measurement (—); simulation (- -). (c) Amplitude of AEM active dynamic characteristics $S_x(s)$ and $S_y(s)$; (d) phase of AEM active dynamic characteristics $S_x(s)$ and $S_y(s)$. *Key*: Measurement of $S_x(s)$ (—); simulation of $S_x(s)$ (- -); simulation of $S_y(s)$ (- · -).

usually significantly higher. Furthermore, the nonlinearity at the actuators resonance frequency also tends to be of minor importance, since the resulting amplitude and phase errors in the AEM's secondary path are relatively small.

5.2. Preload

During the measurements of the previous sections, it has been assumed that the preload of the AEM remains constant. However, considerable quasi-static changes in the engine mount's preload may occur during the operation in a vehicle. These changes result from road disturbances or the drive torque, whose reaction torque has to be supported by the engine mounts. It has been revealed that conventional, passive HEMs exhibit preload-dependent parameters [39,55,56]. Since an adaptive algorithm for the control of an AEM has to be stable in every driving situation, this section analyses the impact of preload changes on the AEM's secondary path.

In addition to the results of Section 4.2, where the preload has been set to -1400 N, two measurements of the transfer functions $P_{yx}(s)$ and $S_x(s)$ are carried out at preloads of -700 N and 0 N. Fig. 11 compares the corresponding experimental and analytical results for the passive and active dynamic characteristics. Only in the area of the actuator's resonance frequency, moderate changes of the active dynamic characteristics $S_x(s)$ and $S_y(s)$ can be observed. Decompression of the engine mount shifts the actuator's resonance frequency to lower frequencies and reduces the corresponding transfer function amplitude. The amplitude of the passive dynamic characteristics $P_{yx}(s)$ is shifted to higher stiffness with increasing preload.

For the analytical discussion of the obtained test results the engine mount's static stiffness characteristics shown in Fig. 12 are considered. The three different preloads corresponding to the previously discussed dynamic measurements are marked in the static stiffness characteristic. Between these operating points, the characteristic is not linear but shows a slightly progressive behavior. This corresponds to an increase in the main rubber stiffness which can also be observed in the passive dynamic characteristics $P_{yx}(s)$ in Fig. 11 at low frequencies. In addition, it has been shown in [39,56] that the damping and bulking properties of the main rubber exhibit a preload dependency as well. Hence, the analytical results of Fig. 10 have been obtained by solving another least-squares curve fitting problem, where the main rubber properties $C_{B,\mathrm{dyn}}(s)$ and $C_{T,\mathrm{dyn}}(s)$ are assumed to be variable while the remaining model parameters are fixed at their initial values of Section 4.2. The identified parameters for the different preloads are shown in Table 2. The stiffness and damping terms decrease with increasing preload. Only the parameters $d_{B,2}$ and $d_{T,2}$ slightly vary around their initial values. The experimental validation of these results in component measurements could be subject of further research.

The identified static stiffness parameters $c_{T,1}$ for the different preloads are shown in the static stiffness characteristic of Fig. 12. The progression of the curve is slightly overestimated by the identified parameters. Since the main rubber spring is modeled linearly, its amplitude dependency is neglected. Therefore, the existing difference between the static stiffness and

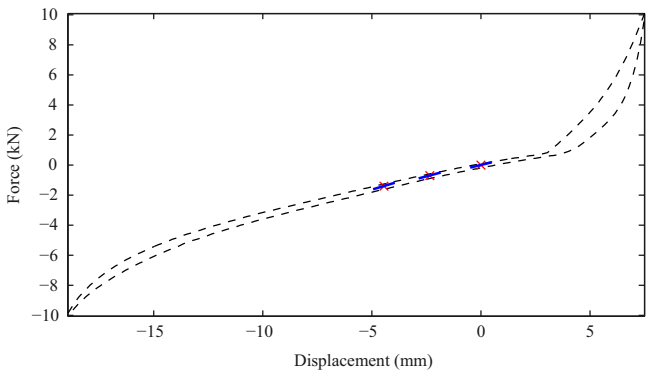

Fig. 12. Static stiffness characteristics of AEM (- -); different preload operating points (×); analytical approximated static stiffness in operating points (—).

Table 2
Experimentally identified model parameters for different preloads.

Symbol	Name	Unit	Preload −1400 N	Preload −700 N	Preload 0 N
$c_{T,1}$	Main rubber spring stiffness 1	N/mm	418.1	386.4	339.4
$c_{T,2}$	Main rubber spring stiffness 2	N/mm	48.1	43.5	37.9
$d_{T,1}$	Main rubber spring damping 1	N s/m	268.7	235.7	183.3
$d_{T,2}$	Main rubber spring damping 2	N s/m	11.1	11.3	11.7
$c_{B,1}$	Main rubber spring bulge stiffness 1	N/mm	180.4	178.9	173.5
$c_{B,2}$	Main rubber spring bulge stiffness 2	N/mm	272.9	248.3	221.5
$d_{B,1}$	Main rubber spring bulge damping 1	N s/m	1525.7	1344.2	1070.6
$d_{B,2}$	Main rubber spring bulge damping 2	N s/m	62.9	64.5	68.1

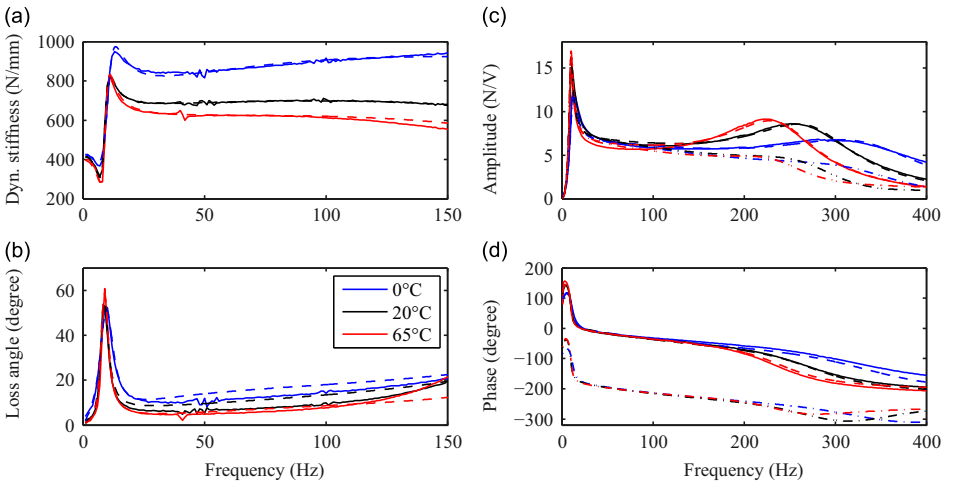

Fig. 13. AEM transfer functions for different component temperatures. (a) Amplitude of AEM passive dynamic characteristics $P_{yx}(s)$; (b) phase of AEM passive dynamic characteristics $P_{yx}(s)$. *Key*: Measurement (—); Simulation (- -). (c) Amplitude of AEM active dynamic characteristics $S_x(s)$ and $S_y(s)$; (d) phase of AEM active dynamic characteristics $S_x(s)$ and $S_y(s)$. *Key*: Measurement of $S_x(s)$ (—); simulation of $S_x(s)$ (- -); simulation of $S_y(s)$ (-··-).

the dynamic stiffness at low frequencies cannot be properly represented and results in an overestimation of the static stiffness [32].

The final consideration of Fig. 11 shows a very good agreement between the experimental and the analytical results. For the application of adaptive control it can be summarized that the impact of a preload change on the AEM's secondary path is limited to the area of the actuator's resonance frequency. In this frequency range only moderate amplitude and phase errors are observed.

5.3. Temperature

Due to their positioning close to the combustion engine, AEMs are exposed to significant temperature variations. It is stated in [38,42] that conventional, passive HEMs possess temperature dependent parameters, but no measurements are given. Since elastomer materials exhibit a pronounced temperature dependence, this section analyses the impact of component temperature on the AEM's secondary path.

The test results of the previous sections have been obtained at a temperature of approximately 20 °C. Fig. 13 additionally shows the passive and active dynamic characteristics $P_{yx}(s)$ and $S_x(s)$ measured at a component temperature of 0 °C and 65 °C. In addition, the simulation results of $P_{yx}(s)$, $S_x(s)$ and $S_y(s)$ are shown. The transfer functions $S_x(s)$ and $S_y(s)$ exhibit temperature-dependent changes in the whole frequency range, which are significantly pronounced in the area of the characteristic resonance frequency associated with the fluid channel and the actuator, respectively. While the amplitude maximum at the fluid channel's resonance decreases with decreasing temperature, the actuator's resonance frequency is shifted to higher frequencies. In the passive dynamic characteristics $P_{yx}(s)$, an overall decrease of the dynamic stiffness can be observed with increasing component temperature. In addition, the loss angle maximum at the fluid channel's resonance is increased.

Elastomeric materials exhibit a significant temperature dependence. While the stiffness of unfilled elastomers increases with increasing temperature, filled elastomers may behave completely differently, due to the complex relationships that arise from the fillers. Depending on the material composition, a decrease of stiffness with increasing temperature may be observed [57]. In addition, a temperature dependence of the fluid properties can be expected as well. According to the procedure of Section 5.2, the adjustment of the analytical model to the experimental results is again formulated as a nonlinear curve-fitting problem. In this case, the parameters of the elastomer components, i.e., the main rubber spring and the actuator's diaphragm, and the fluid channel properties, i.e., density and channel friction, are assumed to be variable within certain limits. The three identified parameter sets by which the simulation results of Fig. 13 were obtained are summarized in Table 3. The measured decrease of the amplitude in $S_x(s)$ and the loss angle $P_{yx}(s)$ at the fluid channel's resonance at lower temperatures can be explained with an increase of the flow losses in the channel. The shift of the actuator's resonance frequency to lower values with increasing temperature is mainly justified with an decrease of the main rubber spring's bulking stiffness.

5.4. Superimposed phase error

Fig. 14 summarizes the maximum phase differences of $S_x(s)$ and $S_y(s)$ which occurred in the simulations of the preceding sections. The previous analysis assumed that the analyzed environmental influences act independently from each other.

Table 3
Experimentally identified model parameters for different component temperatures.

Symbol	Name	Unit	0 °C	20 °C	65 °C
$c_{T,1}$	Main rubber spring stiffness 1	N/mm	427.6	418.1	398
$c_{T,2}$	Main rubber spring stiffness 2	N/mm	174.2	48.1	11.6
$d_{T,1}$	Main rubber spring damping 1	N s/m	359.6	268.7	184.8
$d_{T,2}$	Main rubber spring damping 2	N s/m	36.7	11.1	4.7
$c_{B,1}$	Main rubber spring bulge stiffness 1	N/mm	369.3	180.4	100.0
$c_{B,2}$	Main rubber spring bulge stiffness 2	N/mm	367.5	272.9	202.0
$d_{B,1}$	Main rubber spring bulge damping 1	N s/m	758.9	1525.7	3224.7
$d_{B,2}$	Main rubber spring bulge damping 2	N s/m	77.5	62.9	82.6
d_K	Fluid damping	N s/m	1.2	0.4	0.3
ρ_f	Fluid density	kg/m^3	1030	1000	990
c_A	Actuator stiffness	N/mm	83.6	53.5	53.4
d_A	Actuator damping	N s/m	40.0	19.5	0.1

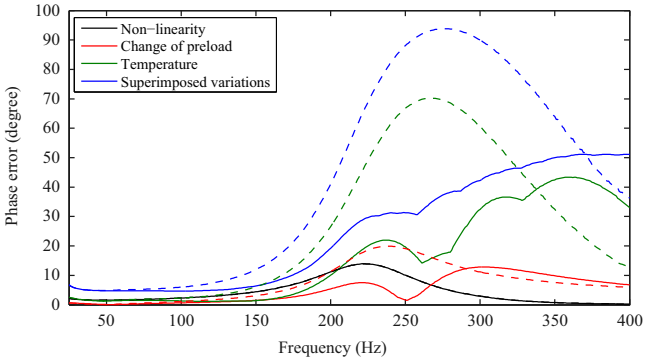

Fig. 14. Simulated phase errors and their analytical superposition ($S_x(s)$ (- -); $S_y(s)$ (—)).

However, in a vehicle application, it is more likely that several influences and their impact on the AEM's secondary path variations are superimposed. Since a plain summation of the phase errors of the individual influences would be an incorrect approach, the nonlinear AEM model is employed in order to estimate the maximum phase error in a realistic application scenario. Therefore, the percentage changes of the model parameters, which have been individually identified in the preceding experiments, are combined in several simulation runs resulting in a set of transfer functions representing the active dynamic characteristics of the AEM. The maximum superimposed phase error is obtained by taking the difference between the enveloping maximum and minimum phase curve of this set. The corresponding analytical results are shown in Fig. 14, as well.

From observation of Fig. 14 three major conclusions can be drawn. First, the superimposed phase error of $S_x(s)$ exceeds 90°, while the phase error of $S_y(s)$ reaches approximately 50°. However, as has been stated in Section 2, depending on the implementation of the FxLMS algorithm, even phase errors well below 90° may lead to instability. Second, it must be noted that the component temperature has the most significant impact of all considered environmental influences on the AEM's secondary path. Third, relevant phase errors are limited to the frequency range of the AEM actuator's resonance frequency above 200 Hz. As a consequence, the AEM should be designed in a way that the actuator's resonance frequency is not within the operating range of the adaptive algorithm. However, the design of an AEM may be limited by certain requirements, e.g., maximum force output or dynamic stiffness of the main rubber spring. As a result, the actuator's resonance frequency may lie within the algorithm's operating range. In this case, additional countermeasures against the algorithm's instability, such as online identification or robustness schemes, have to be applied, but can be limited to the frequency range of the actuator's resonance.

6. Conclusions

In this paper, an experimental and analytical investigation of secondary path variations in AEM has been carried out. The impact of nonlinearity, component temperature and change of preload was experimentally analyzed. It was found that significant secondary path changes are limited to the frequency range of the AEM actuator's resonance frequency above 200 Hz. While the impact of nonlinearity and change of preload was of minor importance, the change of the component temperature mainly contributed to the total phase error. The results of this research are supposed to bridge the gap between the design of an AEM and the application of an adaptive feedforward control algorithm to it. First, an AEM design shifting the actuator's resonance frequency out of the operating range of the adaptive algorithm can significantly ease its application.

Second, knowing that major secondary path errors are limited to the actuator's resonance frequency, appropriate algorithmic countermeasures against instability, such as online identification or robustness schemes, can be restricted to this frequency range. This may lead to computationally more efficient and less performance-degrading methods. Although the above-mentioned findings have been derived in the context of adaptive feedforward algorithms, they are also relevant for non-adaptive feedforward algorithms, which are often proposed for the application in AEMs in order to omit additional feedback sensors [6,9]. Since these algorithms are not capable to adapt to any changes in the transfer characteristics of an AEM, their performance will be degraded not only by the observed secondary path changes, but also by the variations in the passive transfer path.

Acknowledgments

The authors gratefully acknowledge the technical and financial support of Audi AG. In addition, the authors would like to thank Anton Petrov for designing the AEM test rig and conducting some of the measurements. The authors would also like to thank Manuel Behner and Tobias Nussbaumer for their preliminary work in building the analytical model of the AEM.

References

[1] K. Aoki, T. Shikata, Y. Hyoudou, T. Hirade, T. Aihara, Application of an Active Control Mount (ACM) for Improved Diesel Engine Quietness, SAE Paper 1999-01-0832, 1999, pp. 1–6.
[2] P. Fursdon, A. Harrison, D. Stoten, The design and development of a self-tuning active engine mount, *IMechE European Conference on Vehicle Noise and Vibration*, 2000, pp. 21–32.
[3] A. Gennesseaux, Research for New Vibration Isolation Techniques: From Hydro-mounts to Active Mounts, SAE Paper 931324, 1993, pp. 491–499.
[4] A. Hillis, A. Harrison, D. Stoten, A comparison of two adaptive algorithms for the control of active engine mounts, *Journal of Sound and Vibration* 286 (2005) 37–54.
[5] Y.-W. Lee, C.-W. Lee, Dynamic analysis and control of an active engine mount system, *Proceedings of the Institution of Mechanical Engineers, Part D: Journal of Automobile Engineering* 216 (2002) 921–931.
[6] B.-H. Lee, C.-W. Lee, Model based feed-forward control of electromagnetic type active control engine-mount system, *Journal of Sound and Vibration* 323 (2009) 574–593.
[7] H. Mansour, S. Arzanpour, M. Golnaraghi, Active decoupler hydraulic engine mount design with application to variable displacement engine, *Journal of Vibration and Control* 17 (2011) 1498–1508.
[8] H. Mansour, S. Arzanpour, M. Golnaraghi, Design of a solenoid valve based active engine mount, *Journal of Vibration and Control* (2011) 1–12 (published online before print).
[9] H. Matsuoka, T. Mikasa, H. Nemoto, NV Countermeasure Technology for a Cylinder-On-demand Engine—Development of Active Control Engine Mount, SAE Paper 2004-01-0413, 2004, pp. 149–154.
[10] Y. Nakaji, S. Satoh, T. Kimura, T. Hamabe, Y. Akatsu, H. Kawazoe, Development of an active control engine mount system, *Vehicle System Dynamics* 32 (1999) 185–198.
[11] D. Swanson, Active Engine Mounts for Vehicles, SAE Paper 932432 , 1993, pp. 1–9.
[12] C. Togashi, K. Ichiryu, Study on Hydraulic Active Engine Mount, SAE Paper 2003-01-1418, 2003, pp. 1–7.
[13] T. Ushijima, S. Kumakawa, Active Engine Mount with Piezo-actuator for Vibration Control, SAE Paper 930201, 1993, pp. 1–8.
[14] S. Römling, S. Vollmann, T. Kolkhorst, Active engine mount system in the new Audi S8, *MTZ Worldwide* 74 (2013) 34–38.
[15] A. Hillis, Multi-input multi-output control of an automotive active engine mounting system, *Proceedings of the Institution of Mechanical Engineers, Part D: Journal of Automobile Engineering* 225 (2011) 1492–1504.
[16] F. Hausberg, S. Vollmann, P. Pfeffer, S. Hecker, M. Plöchl, T. Kolkhorst, Improving the convergence behavior of active engine mounts in vehicles with cylinder-on-demand engines, *Proceedings of the 42nd International Congress and Exposition on Noise Control Engineering, Internoise 2013*, Innsbruck, 2013, pp. 5244–5252.
[17] P. Fursdon, The design and control of the Avon active engine mount, *Proceedings of the 4th Styrian Noise, Vibration and Harshness Congress*, Graz, 2006, pp. 1–10.
[18] S. Elliott, *Signal Processing for Active Control*, Academic Press, London, San Diego, 2001.
[19] C. Bao, S.P., H. van Brussel, Comparison of two-on-line identification algorithms for active noise control, *Proceedings of the 2nd Conference on Recent Advances in Active Control of Sound and Vibration*, 1993, pp. 38–54.
[20] A. Berkhoff, A technique for improved stability of adaptive feedforward controllers without detailed uncertainty measurements, *Smart Materials and Structures* 21 (2012) 1–12.
[21] R. Fraanje, M. Verhaegen, N. Doelman, Increasing the robustness of a preconditioned Filtered-x LMS algorithm, *IEEE Signal Processing Letters* 11 (2004) 285–288.
[22] R. Fraanje, S. Elliott, M. Verhaegen, Robustness of the Filtered-x LMS algorithm—Part II: *Robustness enhancement by minimal regularization for norm bounded uncertainty*, *IEEE Transactions on Signal Processing* 55 (2007) 4038–4047.
[23] B. Widrow, M. Hoff, Adaptive switching circuits, *Proceedings of IRE WESCON Convention Record*, 1960, pp. 96–104.
[24] D. Morgan, An analysis of multiple correlation cancellation loops with a filter in the auxiliary path, *IEEE Transactions on Acoustics, Speech and Signal Processing ASSP* 28 (1980) 454–467.
[25] B. Widrow, J. McCool, M. Ball, The complex LMS algorithm, *Proceedings of the IEEE* 63 (1975) 719–720.
[26] D. Morgan, C. Sanford, A control theory approach to the stability and transient analysis of the Filtered-x LMS adaptive notch filter, *IEEE Transactions on Signal Processing* 40 (1992) 2341–2346.
[27] S. Snyder, C.H. Hansen, The influence of transducer transfer functions and acoustic time delays on the implementation of the LMS algorithm in active noise control systems, *Journal of Sound and Vibration* 141 (1990) 409–424.
[28] S. Elliott, I. Stothers, P. Nelson, A multiple error LMS algorithm and its application to the active control of sound and vibration, *IEEE Transactions on Acoustics, Speech and Signal Processing* 35 (1987) 1423–1434.
[29] M. Rupp, A. Sayed, Robust FxLMS algorithm with improved convergence performance, *IEEE Transactions on Speech and Audio Processing* 6 (1998) 78–85.
[30] C.H. Hansen, S.D. Snyder, *Active Control of Noise and Vibration*, Chapman & Hall, London, UK, 1997.
[31] A. Payne, The dynamic properties of carbon black-loaded natural rubber vulcanizates. Part I, *Journal of Applied Polymer Science* 6 (1962) 57–63.
[32] C. Scheiblegger, J. Lin, H. Karrer, New nonlinear bushing model for ride comfort and handling simulation—Focussing on linearization and the implementation into mbs environment, *FISITA 2012 World Automotive Congress,* Bejing, 2012, pp. 461–473.
[33] C. Scheiblegger, P. Pfeffer, H. Karrer, N. Geiger, Modelling of elastomer and hydro mounts for ride comfort and handling simulation, *13th International VDI Congress Tires-Chassis-Road*, Hanover, Germany, 2011, pp. 247–268.

[34] C. Scheiblegger, A. Hillis, N. Roy, O. Silva Parez, P. Pfeffer, J. Darling, linear modeling of bushings and cab mounts for calculation of durability loads, *Proceedings of the SAE 2014 World Congress*, 2014-01-0880, Detroit, USA, 2014.
[35] P. Pfeffer, K. Hofer, Simple non-linear model for elastomer and hydro-mountings to optimise overall vehicle simulation, *ATZ Worldwide* 104 (2002) 5–7.
[36] R. Singh, G. Kim, P. Ravindra, Linear analysis of automotive hydro-mechanical mount with emphasis on decoupler characteristics, *Journal of Sound and Vibration* 158 (1992) 219–243.
[37] J. Colgate, C. Chang, Y. Chiou, W. Liu, L. Keer, Modelling of a hydraulic engine mount focusing on response to sinusoidal and composite excitations, *Journal of Sound and Vibration* 184 (1995) 503–528.
[38] G. Kim, R. Singh, A study of passive and adaptive hydraulic engine mount systems with emphasis on non-linear characteristics, *Journal of Sound and Vibration* 179 (1995) 427–453.
[39] A. Geisberger, A. Khajepour, M. Golnaraghi, Non-linear modelling of hydraulic mounts: *Theory and experiment*, *Journal of Sound and Vibration* 249 (2002) 371–397.
[40] J. Lee, R. Singh, Critical analysis of analogous mechanical models used to describe hydraulic engine mounts, *Journal of Sound and Vibration* 311 (2008) 1457–1464.
[41] R. Singh, S. He, Anatomy of a real-life non-linear device: Hydraulic engine mount, *Proceedings of the IMAC-XXV*, 2007, pp. 1–8.
[42] G. Kim, R. Singh, Nonlinear analysis of automotive hydraulic engine mount, *Journal of Dynamic Systems, Measurement and Control* 115 (1993) 482–487.
[43] J. Lee, M. Bae, K. Kim, Limitations of Mechanical Model with Lumped Mass in Representing Dynamic Characteristics of Hydraulic Mount, SAE Paper 2003-01-1466, 2003, pp. 1679–1683.
[44] MATLAB R2011a Optimization Toolbox User's Guide, The Mathworks Inc., Natick, USA, 2011.
[45] M. Costa, J. Bermudez, N. Bershad, Statistical analysis of the FxLMS algorithm with a nonlinearity in the secondary-path, *ISCAS '99. Proceedings of the 1999 IEEE International Symposium on Circuits and Systems,* 1999, pp. 166–169.
[46] T. Jeong, R. Singh, Inclusion of measured frequency- and amplitude-dependent mount properties in vehicle or machinery models, *Journal of Sound and Vibration* 245 (2001) 385–415.
[47] G. Jazar, M. Golnaraghi, Nonlinear modeling, experimental verification and theoretical analysis of a hydraulic engine mount, *Journal of Vibration and Control* 8 (2002) 87–116.
[48] M. Golnaraghi, G. Jazar, Development and analysis of a simplified nonlinear model of a hydraulic engine mount, *Journal of Vibration and Control* 7 (2001) 495–526.
[49] J. Christopherson, G. Jazar, Dynamic behavior comparison of passive hydraulic engine mounts. Part 1: *Mathematical analysis*, *Journal of Sound and Vibration* 290 (2006) 1040–1070.
[50] J. Christopherson, G. Nazar, Dynamic behavior comparison of passive hydraulic engine mounts. Part 2: *Finite element analysis*, *Journal of Sound and Vibration* 290 (2006) 1071–1090.
[51] R. Fan, Z. Lu, Fixed points on the nonlinear dynamic properties of hydraulic engine mounts and parameter identification method: *Experiment and theory*, *Journal of Sound and Vibration* 305 (2007) 703–727.
[52] J.-Y. Yoon, R. Singh, Indirect measurement of dynamic force transmitted by a nonlinear hydraulic mount under sinusoidal excitation with focus on super-harmonics, *Journal of Sound and Vibration* 329 (2010) 5249–5272.
[53] Y. Yu, N. Naganathan, R. Dukkipati, A literature review of automotive vehicle engine mounting systems, *Mechanism and Machine Theory* 36 (2001) 123–142.
[54] M. Sjöberg, On Dynamic Properties of Rubber Isolators, PhD Thesis, KTH Royal Institute of Technology Stockholm, 2002. URL ⟨http://www.diva-portal.org/smash/get/diva2:9268/FULLTEXT01.pdf⟩.
[55] H. Adiguna, M. Tiwari, R. Singh, H. Tseng, D. Hrovat, Transient response of a hydraulic engine mount, *Journal of Sound and Vibration* 268 (2003) 217–248.
[56] M. Tiwari, H. Adiguna, R. Singh, Experimental characterization of a nonlinear hydraulic engine mount, *Noise Control Engineering Journal* 51 (2003) 39–49.
[57] A. Grambow, Bestimmung der Materialparameter gefüllter Elastomere in Abhängigkeit von Zeit, Temperatur und Beanspruchungszustand, PhD Thesis, Rheinisch-Westfälische Technische Hochschule Aachen, 2002. URL ⟨http://darwin.bth.rwth-aachen.de/opus3/volltexte/2003/492/pdf/GrambowAndreas.pdf⟩.

8 MODEL VALIDATION IN AN MBS ENVIRONMENT

The paper in this chapter discussed the entire simulation process of a vehicle when the newly develomed elastomer mounts are used. Within the context of this thesis it gives a wider perception onto the topic, where other factors of impact become more important. Beside the underlying model accuracy the focus of this study is more on the usability and practicality of the fully implemented models within an entire full-vehicle simulation in the daily development process. The positive impact of the new mount model is proven and assessed.

8.1 Paper D 'Durability Loads Prediction of Body-on-Frame Vehicles using Full Vehicle Simulation'

Roy, N., Scheiblegger, C., Darling, J., and Pfeffer, P., "*Durability Loads Prediction of Body-on-Frame Vehicles using Full Vehicle Simulation,"* Int. Journal of Passenger Cars, SAE Technical Paper 2017-01-9675. RETRACTION

- **Full-vehicle study to validate the models in MBS environment**
- As second author, C. Scheiblegger was responsible for model development for bushing elements, design of experiment and data processing, support for parameter identification and presentation of the outcomes; regarding the bushing elements. (Content approx. 40%).

This peer-reviewed paper was published and distributed for several months. It had to be withdrawn by the author of this thesis on request of Fiat-Chrysler Automobiles' legal department due to 'an issue regarding third-party rights in the manuscript'. Meanwhile, the lead author had left the company.

Therefore, the article is exclusively attached in the original hardback version of this thesis, for review of the examiners and supervisors.

8.2 Contribution to Research

This article puts the presented research area in a wider context and discusses the use of full vehicle simulation techniques developed in ADAMS/Car for the prediction of durability loads of a pickup truck. To improve simulation, a practical approach that takes into account the body mounts' non-linear amplitude-dependent behaviour has been used for this survey. A comparison of experimental and model simulation results for one of the most severe proving ground events was made in terms of time histories, power spectral densities, level crossing counting and relative pseudo damage. A parameter study on the effect of changing preloads

has been carried out. The validated full-vehicle model was used for detailed parameter studies and tolerance analyses in a very early phase of the development to significantly improve product quality and development process.

The significance of this article is that non-linear mount models are positively validated for use in the early phase of development at a car manufacturer. The gap between principal research investigations and applied science was closed, to create practical value for industry application. The article evaluates the uses of the new models in an MBS environment. Besides the mount models, other factors highly affect results but the study concludes that the new bushing models significantly contribute to the overall improvement of the full-vehicle simulation. With the successful validation shown in this paper, product quality can now be improved due to the possibility for parameter studies and tolerance-analysis in an early-phase of development. The accuracy of the simulation, including this fine level of detail, can be used to justify a reduction of on-road durability tests and prototypes.

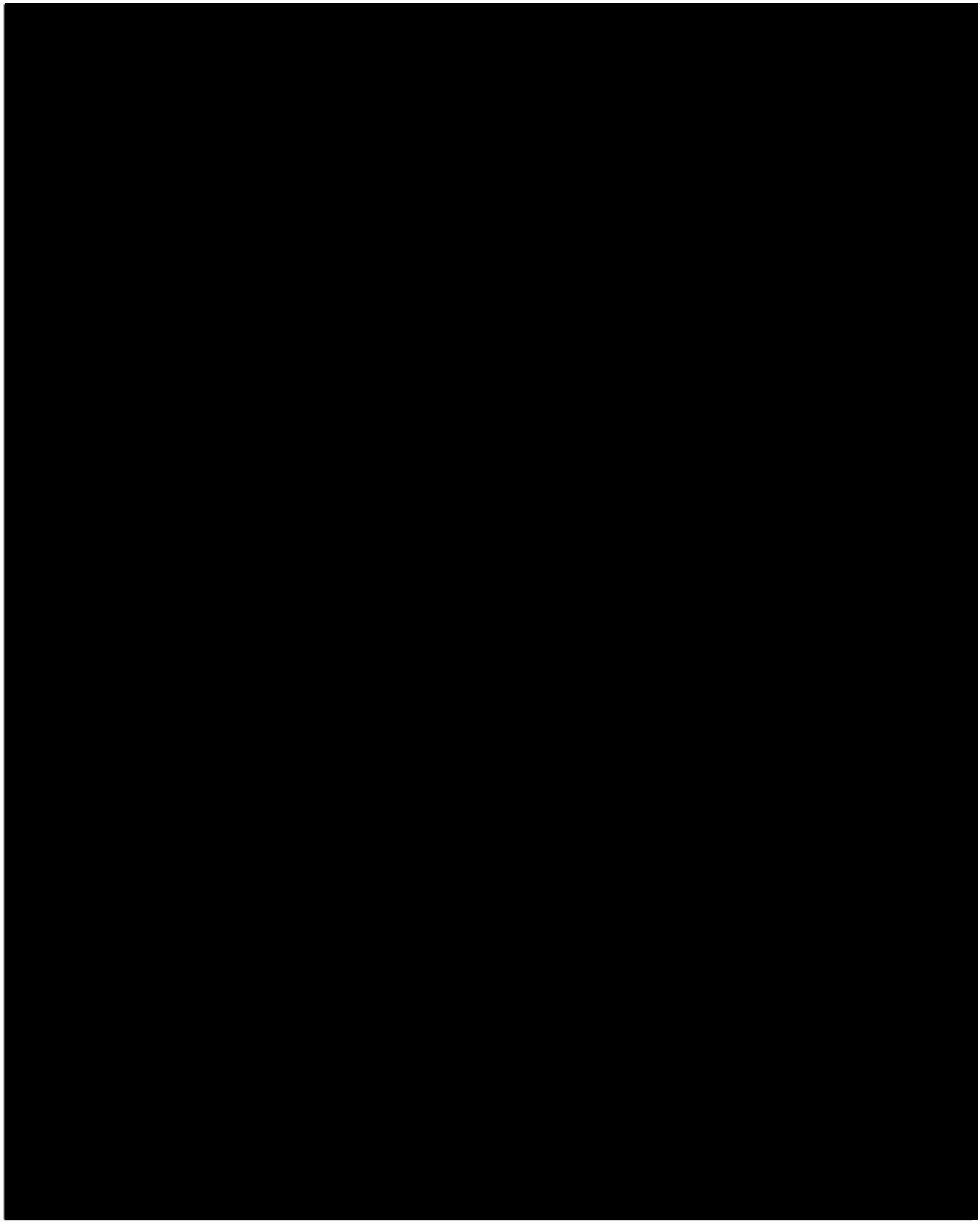

PAPER EXCLUDED IN THIS VERSION BECAUSE RETRACTION

(ONLY FOR EXAMINERS)

9 CONCLUSIONS AND OUTLOOK

New simulation models for engine mounts and suspension bushes have been developed to enhance vehicle simulation. The models fit the amplitude dependent behaviour of the elastomer well and show significantly better results than standard bushing element models. A modular model structure has been chosen to ensure flexibility for different areas of use, where frequency and amplitudes ranges of interest vary and different levels of details are necessary.

Compared with earlier non-linear approaches, the new elastomer model is significantly improved in terms of numerical stability, accuracy and flexibility. Numerical issues for the implementation into MBS have been solved. The prediction of bushes subject to long transient signals is improved with a new term for force limitation. The model can now also be used for other components where friction or higher damping occurs.

Available approaches for hydro mounts already meet the stiffness and damping characteristics for simple passive hydro engine mounts well at sinusoidal input, but results for decoupled mounts and hydro suspension bushes are significantly improved. With the new model, the prediction of transient excitation improves for all types of hydro mounts and bushes. The hydro mount model's accuracy highly benefits from amplitude dependent elastomer elements.

The models have been professionally implemented in a commonly used MBS software environment, with full functionality. Numerical stability and low computing times within all restrictions and possibilities of the goal-software have been proven. A user-mask for Adams has been developed to import model parameter files and define loading conditions; additional scaling factors can be tuned within the MBS environment to take into account tolerances and temperature influences or for design studies. A detailed model evaluation has been carried out in Matlab/Simulink as well as subsequent implementation in MSC Adams/Car. By taking into account the amplitude dependence of rubber bushes, an important source of uncertainty has been eliminated. The overall accuracy of full-vehicle simulation increased.

Successful model validation in an MBS environment has been carried out for ride comfort simulation and durability load analyses. The models can also be used for misuse analyses, acoustics and NVH studies or vehicle handling simulation, with different model parameters.

Further research should quantify the improvements provided within an MBS environment in comparison with standard bushing models, linear model versions and full non-linear approaches in terms of accuracy and computing time.

The automatic parameter optimisation routine in the user tools works very well for hydro engine mounts and should be further improved for hydro suspension bushes. For the elastomer model a rather simple approach for parameter estimation is currently used, based on only one frequency point of interest for two different amplitudes. If all the measured curves are taken into account a parameter optimisation program like the one for hydro mounts would be beneficial for even more accurate results. A force limitation of the friction force is needed to ensure correct behaviour under superimposed and transient long-term signals. The semi-automatic parameter estimation for this factor should be further improved, including a plausibility check and easy switch to change model settings in order to represent a simple friction element. Parts of the elastomer model and the program for parameter estimation can be used to create models for similar suspension components such as suspension damper or jounce bumpers.

Instead of the maximum model accuracy a simple fast and easy to use parameter estimation may be more crucial in the overall context of full-vehicle simulation; therefore the model parameters should also be calculated automatically for a simplified lnearized model version and for a higher frequency range. To further improve the elastomer mount model a more accurate sub-model for frequency dependence can be used, to enhance accuracy over a wider frequency range. A new methodology would be useful to derive reasonable model parameters entirely based on the static stiffness curves, in case detailed measurements are not available.

Overall, the underlying modelling approaches have been proven to be accurate and adequate but the user masks and model implementation in Adams could be further improved as well as user friendliness of the developed parameter identification tools. The benefits of nonlinear model approaches have been proven for load analyses and within a ride comfort study within MSC.Adams/Car. A following up study for ride handling analyses would be useful because here rather more simple MBS tools are used and computing time of each component is even more an issue. All models should be implemented and tested in other MBS software tools.

REFERENCES

Adiguna, H., Tiwari, M., Singh, R., Tseng, H.E. & Hrovat, D., 2003. Transient response of a hydraulic engine mount. Journal of Sound and Vibration, 268(2), pp. 217-248.

Ambrósio, J. & Verissimo, P., 2009. Sensitivity of a vehicle ride to the suspension bushing characteristics. Journal of Mechanical Science and Technology, 23(4), pp. 1075-1082.

Arnold, M., Burgermeister, B., Führer, C., Hippmann, G. & Rill, G., 2011. Numerical methods in vehicle system dynamics: state of the art and current developments. Vehicle System Dynamics, 49(7), pp. 1159-1207.

Arzanpour, S. & Golnaraghi, M.F., 2008. Development of a bushing with an active compliance chamber for variable displacement engines. Vehicle System Dynamics, 46(10), pp. 867-887.

Bachmann, F., 2011. Validation of MSC-Adams Hydro and Elastomer Mounts (Validierung von MSC-Adams Hydro-und Elastomerlagermodellen). Final Year Report, Munich University of Applied Sciencess

Bahnert, T., 2008. Modellbildung und Verifikation verschiedener Dämpfer- und Dämpferlagermodelle für die Simulation von Schwingungskomfort und Akustik: Thesis. Dipl.-Ing., Technische Universität Dresden.

Banks, H.T., 2008. A brief review of some approaches to hysteresis in viscoelastic polymers. Non-linear Analysis: Theory, Methods & Applications, 69(3), pp. 807-815.

Banks, H.T., Pinter, G.A., Potter, L.K., Gaitens, M.J. & Yanyo, L.C., 1999. Modeling of Non-linear Hysteresis in Elastomers under Uniaxial Tension. Journal of Intelligent Material Systems and Structures, 10(2), pp. 116-134.

Barber, A.J., 1999. Accurate Models for Bushings and Dampers using the Empirical Dynamics Method. 1999 European ADAMS User Conference. Berlin.

Barker, M., 2004. The Behaviour of Non-Linear Hydraulic Isolators. Engineering Integrity, 15(1), pp. 28-42.

Berg, M., 1997. A model for rubber springs in the dynamic analysis of rail vehicles. Proceedings of the Institution of Mechanical Engineers, Part F: Journal of Rail and Rapid Transit, 211, p. 14.

Berg, M., 1998. A Non-Linear Rubber Spring Model for Rail Vehicle Dynamics Analysis. Vehicle System Dynamics, 30(3-4), pp. 197-212.

Böhm, J., 2001. Der Payneeffekt: Interpretation und Anwendung in einem neuen Materialgesetz für Elastomere. Dr. rer. nat. Dissertation, Universität Regensburg.

Botev, S., 2008. Digitale Gesamtfahrzeugabstimmung für Ride und Handling. Düsseldorf: VDI-Verl.

Bruni, S., Vinolas, J., Berg, M., Polach, O. & Stichel, S., 2011. Modelling of suspension components in a rail vehicle dynamics context. Vehicle System Dynamics, 49(7), pp. 1021-1072.

Büchler, H.-J., 2011. Application of a new elastomer and hydromount model integrated in the full vehicle simulation process at Porsche: analysis of drive train vibrations on the example of the Panamera Diesel. *4th VI-grade Users Conference.* Udine, Italy.

Cao, D., Song, X. & Ahmadian, M., 2011. Editors' perspectives: road vehicle suspension design, dynamics, and control. Vehicle System Dynamics, 49(1-2), pp. 3-28.

Cardillo, R.M., 1964. Dynamic testing of elastomer mountings. Journal of Applied Polymer Science, 8, pp. 53-71.

Christopherson, J. & Jazar, G.N., 2006a. Dynamic behavior comparison of passive hydraulic engine mounts. Part 1: Mathematical analysis. Journal of Sound and Vibration, 290(3-5), pp. 1040-1070.

Christopherson, J. & Jazar, G.N., 2006b. Dynamic behavior comparison of passive hydraulic engine mounts. Part 2: Finite element analysis. Journal of Sound and Vibration, 290(3-5), pp. 1071-1090.

DIN-53535, 1982. Grundlagen für dynamische Prüfverfahren. DIN 53 535. Berlin: Beuth Verlag.

Eickhoff, B.M., Evans, J.R. & Minnis, A.J., 1995. A Review of Modelling Methods for Railway Vehicle Suspension Components. Vehicle System Dynamics, 24(6-7), pp. 469-496.

Einsle, S. & Steinert, F., 2008. Suspension Simulation. tire.wheel.tech 2008. München, p. 45.

Falkner, A. & Reinalter, W., 2005. The Effect of Road-excited Vibrations on the Load Spectrum, the Required Space and the Ride Comfort. ATZ worldwide, 107(6), pp. 16-18.

Falkner, A. & Reinalter, W., 2006. Consistent vehicle model for determining the design envelope, ride comfort and component load. Vehicle System Dynamics, 44(sup1), pp. 468-478.

Fan, R. & Lu, Z., 2007. Fixed points on the non-linear dynamic properties of hydraulic engine mounts and parameter identification method: Experiment and theory. Journal of Sound and Vibration, 305(4-5), pp. 703-727.

Fischer-von Ronn, N. & Meywerk, M., 2013. Predicting the ride comfort of passenger cars for single-obstacle crossings through an innovative feature extraction method consisting of non-linear geometric approximations of wavelet-transformed acceleration data and airborne sound. Proceedings of the Institution of Mechanical Engineers, Part D: Journal of Automobile Engineering, 228(4), pp. 357-369.

Foumani, M.S., Khajepour, A. & Durali, M., 2003. Application of Sensitivity Analysis to the Development of High Performance Adaptive Hydraulic Engine Mounts. Vehicle System Dynamics, 39(4), pp. 257-278.

Foumani, M.S., Khajepour, A. & Durali, M., 2003. Optimization of Engine Mount Characteristics Using Experimental/Numerical Analysis. Journal of Vibration and Control, 9(10), pp. 1121-1139.

Gan, Z., Hillis, A. J. and Darling, J., 2015. Biodynamic modelling of seated human subjects exposed to uncouples vertical and fore-and-aft whole-body vibration. *Journal of Vibration Engineering and Technologies*, 3 (3), pp. 301-314.

Gao, W., Zhang, N. & Dai, J., 2008. A stochastic quarter-car model for dynamic analysis of vehicles with uncertain parameters. Vehicle System Dynamics, 46(12), pp. 1159-1169.

Georgiou, G., Verros, G. & Natsiavas, S., 2007. Multi-objective optimization of quarter-car models with a passive or semi-active suspension system. Vehicle System Dynamics, 45(1), pp. 77-92.

Giesekus, H., 1995. An alternative approach to the linear theory of viscoelasticity and some characteristic effects being distinctive of the type of material. Rheologica Acta, 34(1), pp. 2-11.

Gipser, M., 2005. FTire: a physically based application-oriented tyre model for use with detailed MBS and finite-element suspension models. Vehicle System Dynamics, 43(sup1), pp. 76-91.

Hammer, H., Reinalter, W. & Tieber, W., 2003. Simulation von Schnittgrößen durch Befahren eines Handlingkurses. ATZ online, (2003-02).

Haupt, P. & Sedlan, K., 2001. Viscoplasticity of elastomeric materials: Experimental facts and constitutive modelling. Archive of applied mechanics, 71(2), pp. 89-109.

Hausberg, F., Scheiblegger, C., Pfeffer, P., Plöchl, M., Hecker, S. & Rupp, M., 2015. Experimental and analytical study of secondary path variations in active engine mounts. Journal of Sound and Vibration, 340, pp. 22–38.

Hausberg, F., 2015. Adaptive und kennfeldbasierte Steuerung aktiver Motorlager, Doctoral Thesis, Technische Universität Wien. Audi Dissertationsreihe, Band 101. Cuvillier Verlag, Göttingen.

Hillis, A.J., Harrison, A.J.L. & Stoten, D.P., 2005. A comparison of two adaptive algorithms for the control of active engine mounts. Journal of Sound and Vibration, 286(1-2), pp. 37-54.

ISO 2631 (E), 1978. Guide for the Evaluation of Human Exposure to Whole Body Vibration. International Organization for Standardization.

ISO 2631 (E), 1985. Evaluation of Human Response to Whole Body Vibration. International Organization for Standardization

Japs, D., 1979. Ein Beitrag zur analytischen Bestimmung des statischen und dynamischen Verhaltens gummielastischer Wulstkupplungen unter Berücksichtigung von auftretenden Axialkräften. Doctoral Thesis, Universität Dortmund.

Kang, D.-W., Jung, S.-W., Nho, G.-H., Ok, J.-K. & Yoo, W.-S., 2010. Application of bouc-wen model to frequency-dependent non-linear hysteretic friction damper. Journal of Mechanical Science and Technology, 24(6), pp. 1311-1317.

Karlsson, A. & Persson, A., 2003. Modelling non-linear dynamics of rubber bushings - parameter identification & validation. Master Thesis, Lund University.

Klingenberg, R., 2001. Materialdämpfung in Antriebskomponenten. Deformationsabhängige Reibung, Viskosität und Relaxation in spielbehafteten Elastomeren. Düsseldorf: VDI Verlag GmbH, pp. 543-565.

Kramarczuk, W., 2012. Belastungsermittlung an Aggregatelagern mittels numerischer Simulation: Doctoral Thesis. Berlin: Logos -Verl. AutoUni-Schriftenreihe.

Kümmlee, 1985. Ein Verfahren zur Vorhersage des nichtlinearen Steifigkeits- und Dämpfungsverhaltens sowie der Erwärmung drehelastischer Gummikupplungen bei stationärem Betrieb (A Method for the prediction of non-linear stiffness and damping behaviour, as well as heating of torsional rubber couplings). VDI-Fortschrittsberichte, Konstruktionstechnik/Maschinenelemente, 136, p. 191.

Lambertz, S., 1994. Nichtlineares Materialgesetz für technische Gummiwerkstoffe mit deformationsabhängigen Eigenschaften und seine experimentelle Überprüfung an Gummifederelementen: Techn. Hochsch., Diss.--Aachen, 1993. Als Ms. gedr. ed. Aachen: Shaker.

Lee, J.H. & Kim, K.-J., 2005. An Efficient Technique for Design of Hydraulic Engine Mount via Design Variable-Embedded Damping Modeling. Journal of Vibration and Acoustics, 127(1), pp. 93-99.

Lee, J.H. & Singh, R., 2008. Critical analysis of analogous mechanical models used to describe hydraulic engine mounts. Journal of Sound and Vibration, 311(3-5), pp. 1457-1464.

Lee, J.-H., Bae, M.-S. & Kim, K.-J., 2004. Limitations of Mechanical Model With Lumped Mass in Representing Dynamic Characteristics of Hydraulic Mount: SAE 2003-01-1466. SAE Transactions; Journal of Passenger Cars - Mechanical Systems, 112(1), pp. 1679-1683.

Lennert, S., 2009. Zur Objektivierung von Schwingungskomfort in Personenkraftwagen. Als Ms. gedr. ed. Düsseldorf: VDI-Verl.

Lewitzke, C. & Lee, P., 2001. Application of Elastomeric Components for Noise Isolation in the Automotive Industry. (01-1477).

Lion, A., 2006. Dynamische Modellierung von elastomeren Bauteilen. Elastomerdynamik. München: Universität der Bundeswehr München, Institut für Mechanik.

Lion, A. & Kardelky, C., 2004. The Payne effect in finite viscoelasticity. International Journal of Plasticity, 20(7), pp. 1313-1345.

Ludwig, R., 2001. Tensorielle Verallgemeinerung eines Stoffmodells für Elastomere: Techn. Hochsch., Diss.--Aachen, 2000. 1. Aufl. ed. Aachen: Mainz.

Lugner, P., Pacejka, H. & Plöchl, M., 2005. Recent advances in tyre models and testing procedures. Vehicle System Dynamics, 43(6-7), pp. 413-426.

Maier, H., 2006. Analyse und Optimierungsmethoden für Aggregatlagerungssysteme zur Verbesserung des Fahrkomforts (Analysis and Optimization of Engine Mounting Systems toImprove Comfort Behaviour): Doctoral Thesis. Karlsruhe: Hrsg.: Prof A. Albers.

MdynamiX AG, 2016, MDYNAMIX [Online]. Available from: www.mdynamix.de [Accessed 10 Dec 2016]

MdynamiX AG, 2017 User Manual ‘Documentation Pfeffer-Models Generation 4 for Elastomer Bushings or Passive and Decoupled Hydro Mounts VI-MXmount/MXmountdesigner User’s Guide Parameter Identification GUIs’

Mischke, M., 1987. Fahrkomfort und Straßenunebenheiten. VDI-Berichte, 1987(650), pp. 79-93.

Mischke, M. & Klingner, B., 1998. Schwingungskomfort im Kraftfahrzeug. ATZ Automobiltechnische Zeitschrift, 100(1), pp. 18-24.

Mitsch, M., Mack, W. & Falkner, A., 2010. On the scattering of test data and the significance of the standard coefficients ‘dynamic stiffness’ and ‘loss angle’ for hydraulic engine mounts. Vehicle System Dynamics, 48(3), pp. 387-403.

Mitschke, M., 2003. Dynamik von Kraftfahrzeugen. 4 ed. Berlin: Springer.

MSC.MARC.Software, 2000. Non-linear Finite Element Analysis of Elastomers, Technical Paper. In: M.A.R. Corporation, ed.

MSCsoftware, 2010. Product Brief - MD Adams 2010 - What’s New [Online]. Available from: www.mscsoftware.com/Submitted-Content/Resources/pb_mdadams_ltr_w.pdf [Accessed 19 Mar 2015].

MSCsoftware, 2015. Adams/Car [Online]. Available from: www.mscsoftware.com/en-uk/product/adamscar [Accessed 19 Mar 2015].

Ohlendorf, J., Pfeffer, P., Bathelt, H. & Wodke, H., 2000. Komfortsteigerung durch optimierte Kopplung von Aggregat- und Fahrwerkslagerung. ATZ Automobiltechnische Zeitschrift, 102(5), pp. 326-332.

Pacejka, H.B., 2002. Tyre and Vehicle Dynamics. Oxford: Butterworth-Heinemann.

Peeken, H. & Lambertz, S., 1994. Nichtlineares Materialmodell zur Beschreibung des Spannungs-Dehnungsverhaltens gefuellter Kautschuk-Vulkanisate. Konstruktion: Organ Der VDI Gesellschaft Konstruktion und Entwicklung, 46(1), pp. 9-15.

Pfeffer, P.E., 1994. *Prüfung von Gummi-Metall-Lagern unter fahrdynamischen und akustischen Gesichtspunkten.* Dipl.-Ing. Thesis, Rheinisch-Westfälische Technische Hochschule Aachen.

Pfeffer, P.E. & Hofer, K., 2002. Simple Non-Linear Model for Elastomer and Hydro-Mountings: to Optimise Overall Vehicle Simulation: Einfaches nichtlineares Modell für Elastomer- und Hydrolager. ATZ worldwide, (5), p. 3.

Pfeffer, P., Scheiblegger, C., Roy, N. & Ortmann, C., 2014. Models for elastomeric and hydraulically damped vibration isolators within full vehicle simulation. *2014 VI-grade Users Conference.* Pollenzo – Bra (CN), Italy.

Pfeffer, P., 2010. Modelling and Simulation of the Elastomer and Hydromount Models (Generation 2) and their implementation in ADAMS. *3rd VI-grade Users Conference.* Bad Nauheim, Germany.

Plöchl, M. & Edelmann, J., 2007. Driver models in automobile dynamics application. Vehicle System Dynamics, 45(7-8), pp. 699-741.

Rauh, J., 2003. Virtual Development of Ride and Handling Characteristics for Advanced Passenger Cars. Vehicle System Dynamics, 40(1-3), pp. 135-155.

Rendek, M., 2011. Transient effects of filler-reinforced rubber with respect to the Payne effect ; experiments, constitutive modelling and FEM implementation. Thesis, Universität der Bundeswehr.

Rendek, M. & Lion, A., 2009. Modelling and finite element simulation of fillerreinforced elastomers under dynamic deformations. Kaut. Gummi Kunstst., pp. 39-45.

Riepl, A., Reinalter, W. & Schmid, M., 2005. Application of the tyre model FTire in the vehicle development process at MAGNA STEYR Fahrzeugtechnik. Vehicle System Dynamics, 43(sup1), pp. 370-383.

Rigler, J., 2009. Komfort- und Akustiksimulation mit Adams/View. 03.07.2009. Presentation at Technische Universität München.

Roy, N., Scheiblegger, C., Darling, J., and Pfeffer, P., 2017. *Durability Loads Prediction of Body-on-Frame Vehicles using Full Vehicle Simulation***,** Int. Journal of Passenger Cars, SAE Technical Paper 2017-01-9675. RETRACTION

Roy, N. & Villaire, M., 2013. Virtual Road Load Data Acquisition using Full Vehicle Simulations. SAE Technical Paper 2013-01-1189.

Sauer, W. & Guy, Y., 2003. Hydro Bushings - Innovative NVH Solutions in Chassis Technology. SAE Technical Paper, 2003-01-1475.

Scheiblegger, C., Pfeffer, P.E., Karrer, H. & Geiger, N., 2011. Modelling of Elastomer and Hydro Mounts for Ride Comfort and Handling Simulation (Modellierung von Elastomer- und Hydrolagern zur Simulation von Fahrkomfort und Fahrdynamik). *13th International VDI Congress Tires-Chassis-Road.* Hanover, Germany: VDI-Berichte 2137, pp. 247-268.

Scheiblegger, C., 2011. New Bushing Models in Adams for Elastomer and Hydro Mounts: Implementation of Generation 4 at AUDI (Neue Lagermodelle in Adams für Elastomer und Hydrolager: Implementierung der Generation 4-Modelle bei Audi). *VW Konzernanwendertreffen MKS, 24th November 2011.* Weissach, Germany.

Scheiblegger, C. & Pfeffer, P., 2012. New Models for Elastomer and Hydro Mounts for Ride Comfort and Handling Simulation. *6th CTI Conference: Federung & Dämpfung im Kfz, 27th Janaury 2012.* Stuttgart, Germany: Car training Institute.

Scheiblegger, C., Lin, J. & Karrer, H., 2013. New non-linear bushing model for ride comfort and handling simulation: Focussing on linearization and the implementation into MBS environment. In: FISITA 2012 World Automotive Congress, 27-30 November 2012, 2012, Beijing, China. Springer Verlag, pp. 461-473.

Scheiblegger, C., Roy, N., Silva Parez, O., Hillis, A., Pfeffer, P. & Darling, J., 2014. Non-Linear Modeling of Bushings and Cab Mounts for Calculation of Durability Loads. SAE Technical Paper 2014-01-0880

Scheiblegger, C., Roy, N., Hillis, A. J., and Pfeffer, P., 2016. Modeling Hydro Mounts in Vehicles for Durability Load Analyses, Ride Comfort and Vehicle Dynamics Simulation. *AVEC'16 - Proceedings of the 13th International Symposium on Advanced Vehicle Control AVEC'16.* CRC Press, p. 703-712 10 p.

Scheiblegger, C., Roy, N., Hillis, A. J., and Pfeffer, P., 2017. Hydro mounts: An in-depth look at modeling hydro mounts in vehicles for durability load analyses, ride comfort and vehicle dynamics simulation. Vehicle Dynamics International, Annual Showcase 2017.

Sedlaczek, K., Dronka, S. & Rauh, J., 2011. Advanced modular modelling of rubber bushings for vehicle simulations. Vehicle System Dynamics, 49(5), pp. 741-759.

Sedlaczek, K., Dronka, S. & Rauh, J., 2011. Advanced modular modelling of rubber bushings for vehicle simulations. Vehicle System Dynamics, 49(5), pp. 741-759.

Sedlan, K., 2000. Viskoelastisches Materialverhalten von Elastomerwerkstoffen: Experimentelle Untersuchung und Modellbildung. Universität Gesamthochschule Kassel.

Simpack, 2010. SIMPACK - Elastomer [Online]. Available from: www.simpack.com [Accessed 19 Mar 2015].

Singh, R., Tiwari, M., Adiguna, H., Hrovat, D. & Tseng, H., 2002. Transient Response Evaluation of a Hydraulic Engine Mount. Sound and vibration, p. 5.

Sjöberg, M., 2002. On Dynamic Properties of Rubber Isolators. Doctoral Thesis, Royal Institute of Technology (KTH).

Sjöberg, M. & Kari, L., 2002. Non-Linear Behavior of a Rubber Isolator System using Fractional Derivatives. Vehicle System Dynamics, 37(3), pp. 217-236.

Sjöberg, M. & Kari, L., 2003. Testing of non-linear interaction effects of sinusoidal and noise excitation on rubber isolator stiffness. Polymer Testing, 22(3), pp. 343-351.

Stammen, K., 2009. Bewertung des Schwingungskomforts in PKW mit Hilfe von Regressionsmodellen und künstlichen neuronalen Netzen. Als Ms. gedr. ed. Düsseldorf: VDI-Verl.

Steinweger, T. & Weltin, U., 1998. Mehrdimensionale Beschreibung elastischer Lager in MKS Simulationen. VDI Berichte Nr. 1416. Düsseldorf: VDI Verlag GmbH.

Stommel, M., 1999. Beschreibung der viskoelastischen mechanischen Eigenschaften, der Betriebsfestigkeit und des Bruchverhaltens von Elastomerbauteilen mit der Finiten-Elementen-Methode (Description of the Viscoelastic Mechnical Properties, the Service

Life and the Fracture Behaviour of Rubebr Parts by the Finite-Element-Method) Doctoral Thesis. Aachen: Mainz.

Turner, Richard (2005): Modelling of Non-linear Elastomer Mounts. Final Year Report. Bath. University of Bath, Department of Mechanical Engineering.

VDI-3880,2004. VDI 3880: Damping of Materials and Members: Damping of Solids (Verein Deutscher Ingenieure).

VDI 2057, 2017. VDI 2057-1: , V.D.I., Human Exposure to Mechanical Vibrations – Whole-Body Vibration. (Verein Deutscher Ingenieure)

VI-grade, 2015. VI-GRADE [Online]. Available from: www.vi-grade.com/en/products/vi-mxmount/ [Accessed 19 Mar 2016].

Waltz, M., 11.10.2005. Dynamisches Verhalten von gummigefederten Eisenbahnrädern. Dissertation, Rheinisch-Westfälische Technische Hochschule.

Weidemann, C., 2002. Fahrdynamik und Verschleiß starrer und gummigefederter Eisenbahnräder: Doctoral Thesis. Rheinisch-Westfälische Technische Hochschule, Aachen. Aachen: Shaker.

Whear, R. & Williams, H.T., 2005. Advanced Hydraulically Damped Elastomeric Component Models. SAE Transactions; Journal of Passenger Cars - Mechanical Systems, 114, p. 5.

Williams, H.T. & Whear, R., 2005. Elastomer Models for Virtual Mounting Systems. SAE Technical Paper 2005-01-1075, p. 7.

Yang, X., 2011. Effects of bushings characteristics on suspension ball joint travels. Vehicle System Dynamics, 49(1-2), pp. 181-197.

Yang, X., Muthukrishnan, G., Seo, Y.-J. & Medepalli, S., 2004. Powertrain Mount Loads Prediction and Sensitivity Analyses. 2004 SAE World Congress. Detroit, Michigan: SAE International.

Yang, X. & Xu, P., 2012. Chapter 1 - Road Load Analysis Techniques in Automotive Engineering. In: Y.-L. Lee, M.E. Barkey & H.-T. Kang, eds. Metal Fatigue Analysis Handbook. Boston: Butterworth-Heinemann, pp. 1-60.

Yang, Zehao (2009): Modelling of a vehicle hydraulic engine mount. Final year project. University of Bath, Department of Mechanical Engineering

Yarmohamadi, H. & Berbyuk, V., 2010. Computational model of conventional engine mounts for commercial vehicles: validation and application. Vehicle System Dynamics, 49(5), pp. 761-787.

Yu, Y., Naganathan, N.G. & Dukkipati, R.V., 2001a. A literature review of automotive vehicle engine mounting systems. Mechanism and Machine Theory, (36), pp. 123-142.

Yu, Y., Peelamedu, S.M., Naganathan, N.G. & Dukkipati, R.V., 2001b. Automotive Vehicle Engine Mounting Systems: A Survey. Journal of Dynamic Systems, Measurement, and Control, 123(2), p. 186.

Zeman, J., 2009. Dynamic Bushing and Hydromount. Simpack News, 13(1), p. 3.

Ziegenhagen, S., Standardisierte Beschreibung des Übertragungsverhaltens von Elastomer-Kupplungen bei stationärem und instationärem Betrieb. Doctoral Thesis, Technische Universität Berlin.

LIST OF ABBREVIATIONS AND SYMBOLS

ABBREVIATIONS

AEM	active engine mount
BOF	body on frame vehicle
COD	cylinder on demand
COG	centre of gravity
CTVC	ContiTech Vibration Control
DOF	degree of freedom
EM	elastomer model
FEA	finite element analyses
FIR	finite impulse response
FxLMS	filtered-x least mean squares
GSE	general state equation
GUI	graphical user interface
HEM	hydraulic engine mount
HM	hydraulic mount
HBU	hydraulic bushing element
LCA	lower control arm
LIN	linear
LMS	least mean squares
LtFr	left front
LtRr	left rear
MBD	multi-body dynamics
MBS	multi-body simulation
MSF	Magna Steyr Fahrzeugtechnik
NVH	noise, vibration and harshness
NR	natural-rubber
PFE	property file format for first generation of models (*.pfe)
PID	proportional integral derivative (controller)
RDL	model parameter for non-linear force of elastomer model
RtFr	right front
RtRr	right rear
RVIT	rotary variable inductive transducers
SISO	single input single output
Stabar	stabilizer bar

TMD	tuned mass damper
UBU	universal bushing property file (*.ubu) for Matlab/Simulink
UBF	universal bushing format (*.ubf) for Adams property files
UCA	upper control arm

SYMBOLS

a, a_x, a_y, a_z,	acceleration, acceleration in x, y, z direction (m/s²)
A_A	decoupler area (m^2)
A_B, $A_{B\,10}$	equivalent bulking area (m^2)
A_K, $A_{K\,10}$	cross-sectional area of fluid channel (m^2)
$A_{K\,10\,i}$	cross-sectional area of bypass channel in hydro bushes (m²)
A_S	secondary path amplitude (-)
A_T	equivalent piston area of main rubber spring (m^2)
B	magnetic filed strength (T)
c_1, c_2, C_1, C_2	stiffness coefficients of elastomer model (N/m)
C_A	actuator stiffness (N/m)
c_B, $C_{B,dyn}$, $C_{B,dyn}(S)$	dynamic stiffness of main rubber bulking properties (N/m)
$C_{B,1}$, $C_{B,2}$	main rubber spring bulge stiffness 1 and 2 (N/m)
$C_{T,dyn}$, $C_{T,dyn}(S)$	dynamic stiffness of main rubber spring (N/m)
$C_{T,1}$, $C_{T,2}$	main rubber spring stiffness 1 and 2 (N/m)
$C_{A,dyn}(S)$	actuator transfer function (N/m)
$C_{K,dyn}(S)$	fluid channel transfer function (N/m)
d_1, d_2	damping coefficients dashpot elements of elastomer model (N s/m)
d_{10}	damping coefficient for linear fluid damping (N s/m)
d_A	actuator damping (N s/m)
$d_{B,1}$, $d_{B,2}$	main rubber spring bulge damping 1 and 2 (N s/m)
d_K	damping coefficient induced by loss of fluid flow along inertia track (N s/m)
$d_{K,quad}$	quadratic damping coefficient induced by los of fluid flow along inertia track (N s^2/m^2)
dt	damping coefficient dashpot element (N s/m)
$d_{T,1}$, $d_{T,2}$	main rubber spring damping 1 and 2 (N s/m)
$d(n)$	chassis vibration (-)
$D_{decoupling}$	decoupling amplitude (m)
$e(n)$	error signal (-)
$f_{0\,10}$	resonance frequency of hydro mount (Hz)
f_0	reference frequency for elastomer model (e.g. 10 Hz) (Hz)
$f_1(t)$, $F_1(s)$, $f_2(t)$, $F_2(s)$	internal forces of elastomer model (N)
F, F_{stat}, F_{LIN}, F_{NL}	force due to static, linear or non-linear model part (N)
$\hat{F}(\Omega)$	amplitude of force at excitation frequency (N)

$f_A(t)$, $F_A(s)$	actuator force (N)
$f_x(t)$, $F_x(s)$	transmitted force to the engine (N)
$f_y(t)$, $F_y(s)$	transmitted force to the chassis (N)
G	force offset due to preload (N)
H	horizontal scaling in Adams mask for unit conversions (-)
$i(t)$	current (A)
j	complex unit j = √-1
k_b	bulging stiffness of fluid chamber (N/m)
k_M	voice coil constant (kg m/A s^2)
k_{stat}	static stiffness (N/m)
$k_{stat\ 0}$	static stiffness at operating point (certain preload) (N/m)
K_d	complex (dynamic) stiffness (N/m)
$K_{decoupling}$	Stiffness gradient for calculation of decoupling characteristics (-)
k_{dyn}	average dynamic stiffness (N/m)
K_t	spring rate (N/m)
k_1	main spring (N/m)
k_2	second spring in elastomer model (N/m)
k_{Sign}, k_{SignB}, $k_{Sign\ D}$, $k_{Sign\ P}$, k_{SignT},	stiffness gradient of tangens-hyperbolicus function, to replace discontinuous sign function and (de)activate features 0: off | $1e^9$ (-)
k_T	stiffness of main rubber, top mount (N/m)
l	coil length (m)
l_K	length of fluid channel (m)
L	moving coil inductance (H)
m_A	actuator mass (kg)
m_K	fluid mass of inertia track (kg)
M_k	dynamic tuned mass damping effect due to the fluid pulsation in the channel
n	sample number (-)
p_{LIMIT}	pressure limit in hydro mount during upstroke (Pa)
$p(n)$	impulse response of P(z) (-)
$p_i(t)$	pressure inside upper fluid chamber (N/m^2)
$P(z)$	primary path (-)
$P_{xx}(S)$	passive dynamic AEM characteristics $F_X(s)/X_T(s)$ (N/m)
$P_{yy}(S)$	passive dynamic AEM characteristics $F_y(s)/X_T(s)$ (N/m)
Q, Q_0, Q_2	displacement offset in Adams subsystem, for design position (m)
r	engine order (-)
R	moving coil resistance (Ω)
s	Laplace variable (-)
$\hat{s}$, $\hat{s}_1$, $\hat{s}_2$	excitation displacement amplitude (m)
s(t)	deflection, displacement (m)
s_0	deflection at design preload
$s(n)$	impulse response of S(z) (-)

$s_{p,1}$, $s_{p,2}$, $s_{p,3}$	poles $P_{xx}(s)$, $P_{yx}(s)$, $S_x(s)$, $S_y(s)$ (-)
$s_{yx,1}$, $s_{yx,2}$, $s_{x,1}$, $s_{y,1}$	zeros of $P_{xx}(s)$, $P_{yx}(s)$, $S_x(s)$, $S_y(s)$ (-)
$S(z)$	secondary path (-)
$S_x(s)$	active dynamic AEM characteristics $F_x(s)/U(s)$ (N/V)
$S_y(s)$	active dynamic AEM characteristics $F_y(s)/U(s)$ (N/V)
$\hat{S}(z)$	secondary path estimate (-)
t	continuous time (s)
T	sample time (s)
U	displacement input (m)
$\hat{U}(\Omega)$	amplitude of displacement input (m)
u(n)	control output of adaptive filter (-)
u'(n)	control output of adaptive filter filtered by secondary path dynamics (-)
U(t), U(s)	voltage (V)
U_{ind}, U_R,U_L	induced, resistance, inductance voltage (V)
$v(t)$	velocity (m/s)
v(n)	engine vibration (-)
w(n)	complex filter weight (-)
$x_A(t)$, $X_A(s)$	displacement of actuator mass (m)
x(t), X(s)	displacement of elastomer model at engine side (m)
$x_B(t)$, $X_B(s)$	displacement of upper fluid chamber bulking area (m)
$x_K(t)$, $K_K(s)$	displacement of fluid in inertia track (m)
$x_T(t)$, $X_T(s)$	displacement of AEM at engine side (m)
x(n)	complex reference signal (-)
x'(n)	complex reference signal filtered by secondary path estimate (-)
y(t), Y(s)	displacement of AEM at chassis side (m)
z	variable of z transform
z(t), Z(s)	internal displacement of elastomer model (m)
α	*alpha*; ratio of spring coefficients for elastomer model $(\alpha=k_1/k_2)$ (-)
β	*beta*; ratio of damping coefficients ($\beta=c_2/c_1$) (-)
γ	*gamma*; ratio of damping coefficient / spring coeff. ($\gamma=c_1/k_1$) (s)
δ	loss angle (deg)
δ_s	secondary path phase angle (deg)
ε, ε_x, ε_x, ε_z	strain (-)
$\kappa_{B,dyn}$	volumetric compliance of upper fluid chamber (m^5/N)
λ	*lambda*; scaling factor for velocity-dependent linear model part (-)
μ	adaptation step-size
ρ	model internal parameter *rho;* for non-linear stiffness decrease (1/m)
ρ_f	fluid density (kg/m^3)
ω	engine speed (rad/s)
φ	rotation angle (rad)
Ω	frequency (rad/s)

APPENDIX

A1 Parameter List Elastomer Model

G4E: Pfeffer Model Generation 4 for Elastomer mounts

	USER INPUT MATLAB	VARIABLE / ABBREV.	MODEL INTERNAL PARAMETRS IN *.UBU	MODEL INTERNAL PARAMETRS IN *.UBF	STANDARD VALUE
STATIC STIFFNESS					
NL static stiffness curve			NL_CURVE	CURVE	
control NL stat sitffness	**Inclue nonlinear curve?**		Act_nonlinear	USE_CURVE	Act_nonlinear=0 / USE_CURVE = 'no'
control static coupling			**Couple**	-	Couple=0 / depends on SHAPE
linear static stiffness	**static stiffness**	**kstat**		STIFFNESS_STATIC	50 ... 3000E3 N/m
Scaling static stiffness / NL stiffness curve			**set_FSTAT**	SCALE_STIFFNESS_STATIC / SCALE_CURVE	set_FSTAT=1
LINEAR PART - FREQUENCY DEPENDENCE					
	dynamic hadening @ SA1	**DH1**		dynamic_hardening_1	DH1= kdyn1/kstat; 1.05 ... 1.5
	first (smaller) amplitude	**SA1**		amplitude_1	SA1=0.1mm
	Loss angle in degree	**delta_grad**		loss_angle	delta_grad=3
	Layout frequency	**FREQ**		layout_frequency	FREQ=10
model internal to			alfa	ALPHA	
calculate shape of			beta	BETA	
frequency dependence			gamma	GAMMA	
scaling loss angle due to linear part			scaler	LAMBDA	
scaling linear part			**set_LIN**	SCALE_FREQ	set_LIN=1
NONLINEAR PART - AMPLITUDE DEPENDENCE					
	dynamic hardening @SA2	**DH2**		dynamic_hardening_2	DH2= kdyn2/kstat; DH2<DH1
	second (higher) amplitude	**SA2**		amplitude_2	SA2=2mm
model internal calc.			rho	RHO_RUBBER	
Increase of stiffness			RDL	RDL_RUBBER	
NL module force	**Force Limit ON/OFF**		kSign	FRICTION_SIGNUM_GRADIENT	kSign=1e9 (on) kSign=0 (off)
limitation (G4 only)	string to calculate max. NL	**strFmax**		-	strFmax='RDL'
	force		Fmax1	FRICTION_MAX_1	Fmax1=RDL
			Fmax2	FRICTION_MAX_2	Fmax2=Fmax1
	max. nonlinear force		**Fmax**	-	Fmax=kstat*Fmax1
scaling nonlinearpart			**set_NONLIN**	SCALE_AMPL	set_NONLIN=1
NL Module (G2 - Porsche only)	relaxation factor		rnl	-	rnl=0

A2 Parameter List Hydro Mount Model

A2.1 Main Parameter Symbols & Variables in Matlab

Symbols	*Name in the mfile*	Typical values	Unit	Description
c_T	*cT10*	2.20E+05	N/m	stiffness of top mount
A_0	*AB10*	3.50E-03	m	effective piston area
A_K	*AK10*	5.70E-05	m²	cross sectional area of fluid channel
l_K	*lK10*	2.60E-01	m	length of fluid channel
d	*d10*	1.50E-01	N s/m	damping coefficient of the fluid channel
b	*beta10*	5.00E-01	N s^2/m^2	damping coefficient for quadratic term
f_0	*f010*	1.20E+01	Hz	Resonance frequency
r_F	*rhof*	1.10E+03	kg/m³	Fluid density
d	*delta*	2.50E+00	deg	Loss angle at SA1 and FREQ
f	*FREQ*	1.00E+01	Hz	Frequency for parameters DH1, DH2 and delta (usually 10Hz)
DH1	*DH1*	1.25E+00	-	Dynamic Hardening (Kdyn/Kstat) at first amplitude
sA1	*SA1*	1.00E-04	m	first (lower) excitation amplitude
DH2	*DH2*	1.10E+00	-	Dynamic Hardening (Kdyn/Kstat) at second amplitude

sA2	*SA2*	2.00E-03	m	second (higher) excitation amplitude
RM	*RDLB10*	8.00E-04	m	Non-linear factor for puffing stiffness
rho	*rhoDLB10*	400	1/m	
	GB_FRC_damp	1.60E-01	-	Multiplication factor for internal model parameters (α, β, γ)
cB	*cB10*	calculated	N/m	puffing stiffness
mK	*mK10*	calculated	Kg	effective channel fluid mass
α	*alfa10z*	3.72E-01	-	Internal model parameter (constant) of elastomeric mount module
β	*beta10z*	9.71E-02	-	
γ	*gamma10z*	8.45E-03	s	
$D_{decoupling}$	$D_{decoupling}$	0.001	m	play displacement of the decoupler

A2.1 Parameter List Property File Format ubf

Model Parameter Property File *ubf-format	Model Variable	Typical Value	Unit
Model Parameter Elastomer Parts			
MAIN_RUBBER_AMPLITUDE_1	SA1	0.0001	m
MAIN_RUBBER_AMPLITUDE_2	SA2	0.001	m
MAIN_RUBBER_DYNAMIC_HARDENING_1	DH1	1.6104	-
MAIN_RUBBER_DYNAMIC_HARDENING_2	DH2	1.2842	-
MAIN_RUBBER_LAYOUT_FREQUENCY	FREQ	10	Hz
MAIN_RUBBER_LOSS_ANGLE	delta	3	deg
MAIN_RUBBER_STIFFNESS_STATIC	cT10	647857	N/m
MAIN_RUBBER_USE_CURVE	Act_nonlinear	YES / NO	-
CURVE	NL_CURVE	Table [2x31]	N m
ALPHA	alfa	0.3717	-
BETA	beta	0.0971	-
GAMMA	gamma	0.0084	s
LAMBDA	scaler		m/N
MAIN_RUBBER_RDL	RDLT		m
MAIN_RUBBER_RHO	rhoDLT		1/m
MAIN_RUBBER_SCALE_AMPL	set_NONLINcT	1	-
MAIN_RUBBER_SCALE_FREQ	set_LINcT	1	-
MAIN_RUBBER_FRICTION_MAX_1	Fmax1T	10*RDLT	m
MAIN_RUBBER_FRICTION_MAX_2	Fmax2T	10*RDLT	m
MAIN_RUBER_FRICTION_SIGNUM_GRADIENT	kSignT	1e+009	-
CHAMBER_RUBBER_STIFFNESS_STATIC	cB10		N/m
CHAMBER_RUBBER_AMPLITUDE_1	SA1B	0.0001	m
CHAMBER_RUBBER_AMPLITUDE_2	SA2B	0.001	m
CHAMBER_RUBBER_DYNAMIC_HARDENING_1	DH1B	1.4721	-
CHAMBER_RUBBER_DYNAMIC_HARDENING_2	DH2B	1.08	-
CHAMBER_RUBBER_FRICTION_MAX_1	Fmax1B	10*RDLB	m
CHAMBER_RUBBER_FRICTION_MAX_2	Fmax2B	10*RDLB	m
CHAMBER_RUBBER_FRICTION_SIGNUM_GRADIENT	kSignB	1e+009	-
CHAMBER_RUBBER_LAMBDA	GB_FRC_damp		
CHAMBER_RUBBER_LAYOUT_FREQUNCY	FREQB	10	Hz

CHAMBER_RUBBER_LOSS_ANGLE	deltaB	5	deg
CHAMBER_RUBBER_RDL	RDLB		m
CHAMBER_RUBBER_RHO	rhoDLB		1/m
CHAMBER_RUBBER_SCALE_AMPL	set_NONLINcB	0	-
CHAMEBR_RUBBER_SCALE_FREQ	set_LINcB	1	-
Parameter for Hydraulic System	**Variable**	**Value**	**Unit**
CHAMBER_AREA	AB10	0.0044	m^2
CHAMBER_CURVE_IMPACT_PRELOAD	NL_CURVE_cB	Table [31x2]	1/m
CHAMBER_PRELOAD_SENSITIVITY_OFFSET	Q0	0	m
CHAMBER_PRELOAD_SENSITIVITY_SIGNUM_GRADIENT	kp	0	-
DECOUPLING_CLEARANCE	D_decoupling	0.0001	m
DECOUPLING_GRADIENT	K_decoupling	1	-
FLUID_CHANNEL_AREA	AK10	0.00018643	m^2
FLUID_CHANNEL_LENGTH	lK10	0.28	m
FLUID_DAMPING_EXPONENT	set_POW	2	-
FLUID_DAMPING_EXPONENT_GRADIEENT	kSignD	1e+009	-
FLUID_DAMPING_LINEAR	d10	0.3	N s/m
FLUID_DAMPING_NONLINEAR	beta10	0.3	N s^2/m^2
FLUID_DENSITY	rhof	1090	kg/m^3
FLUID_MASS	mK10		kg
FLUID_PRESSURE_LIMIT_BYPASS_AREA	AK10i	0 (OFF)	m²
FLUID_PRESSURE_LIMIT_BYPASS_THRESHOLD	P_threshold	50000	N/m²
FLUID_RESONANCE_FREQUENCY	f010	26	Hz
FLUID_PRESSURE_LIMIT	P_LIMIT	100000	N/m^2
FLUID_PRESSURE_LIMIT_SIGNUM_GRADIENT	kSignP	0 (OFF)	-
SCALE_CHAMBER_STIFFNESS	set_FB	1	-
SCALE_FLUID_DAMPING_LINEAR	set_FLDAMP1	1	-
SCALE_FLUID_DAMPING_NONLINEAR	set_FLDAMP2	1	-
SCALE_FLUID_TUNED_MASS_DAMPER	set_FLTMD	1	-
SCALE_FREQ_SHIFT	set_FREQ	1	-
SCLAE_MAIN_RUBBER_CURVE	set_FT	1	-
Virtual Test Rig Parameters *ubf-format	**Variable**	**Value**	**Unit**
testrig_displacement_scaling	H	1	-
testrig_offset	Q	0	m
testrig_offset_2	Q2	0	m
testrig_preload	G	0	N
trestrig_force_scaling	V	1	-
testrig_Couple	Couple	on /off	-
testrig_Ccdyn	CCdyn	0...5e-2	-
testrig_input_num	input_num	1 (sinus) /2(time)	-
testrig_ModelType	ModelType	G4D (Hydro) G4E (Elasto)	-
main_rubber_friction_string	strFmaxT	RDLT10	1/m
chamber_rubber_friction_string	strFmaxB	RDLB10	1/m